analytical chemistry

pubs.acs.org/ac Review

Optical Spectroscopy of Surfaces, Interfaces, and Thin Films

Thomas J. Blackburn, Sarah M. Tyler, and Jeanne E. Pemberton*

Cite This: *Anal. Chem.* 2022, 94, 515−558

Read Online

ACCESS | Metrics & More | Article Recommendations

CONTENTS

INTRODUCTION AND SCOPE

Efforts to characterize solid/liquid, solid/gas, liquid/gas, liquid/liquid, and liquid/gas interfaces utilizing optical spectroscopies in the ultraviolet−visible (UV−vis), infrared (IR), and terahertz (THz) regions of the electromagnetic spectrum have continued unabated since our previous review of this area in 2019.[1] Such interfaces are ubiquitous in the chemical and biochemical sciences and play central roles in many technologies and industrial processes in areas including biochemical and chemical sensing, biomedicine, nanotechnology, lubrication, corrosion, energy conversion and storage, and catalysis. Developing an understanding of relevant chemical and biochemical events at surfaces and interfaces on a spatial scale approaching molecular and on a temporal scale approaching that of chemical reactivity is essential to advancing these areas. The creative and clever implementation of optical spectroscopies and microscopies in an ever-increasing arsenal of forms has enabled measurement advances in understanding fundamental chemical and physical phenomena that, in turn, have driven significant improvements in related processes and technologies.

Indeed, researchers have at their disposal an increasing array of surface and interface optical spectroscopy analysis tools. Here, we restrict our consideration to those methods utilizing or producing signals in the UV−vis, IR, or THz spectral regions for chemical or biochemical systems at interfaces and in surface molecular layers or thin films. This review covers recent work reported in the primary scientific literature in the approximate 3-year period from the time ending the coverage of our last review through September 2021. Given the breadth represented by such work, a truly comprehensive review of this area is not possible within the space limitations of this review. We have endeavored here to report on scientific efforts that, in our view, represent significant advances in capabilities, especially advances in spatial and/or temporal resolution, or that represent significant advances in understanding important surface or interfacial chemistry or biochemistry made possible through inventive advances in optical spectroscopic methods. Choices of work presented are necessarily selective at the discretion of the authors. Any omissions of particular work, inadvertent and otherwise, are the sole responsibility of the authors, with no negative connotations about the scientific importance of this work implied.

In surveying this body of work, noteworthy are continued advances in sensitivity, spatial and temporal resolution, and the

Published: January 3, 2022

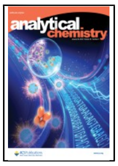

https://doi.org/10.1021/acs.analchem.1c05323

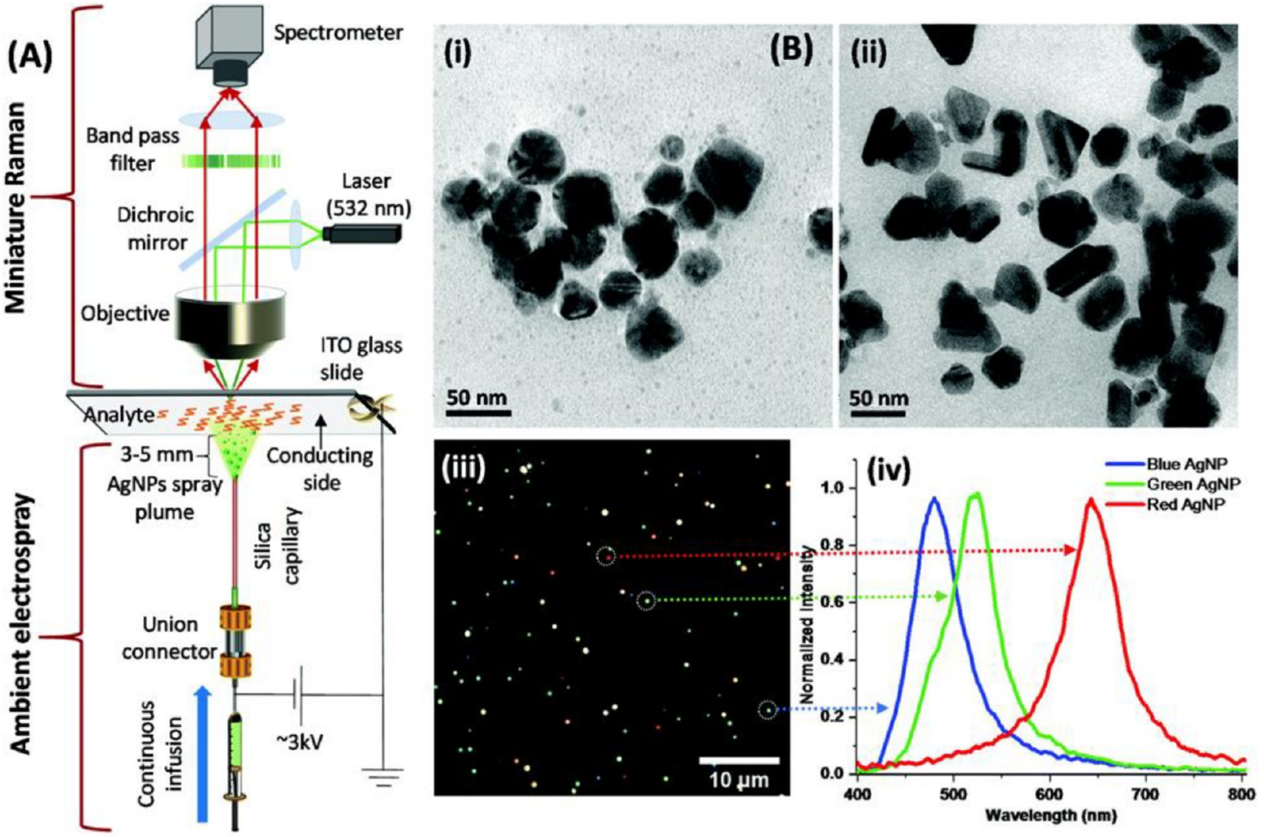

Figure 1. (A) Schematic representation of the AESD-RS setup and (B) characterization of the soft-landed Ag NPs before and after electrospray: (i and ii) transmission electron microscopy (TEM) images of the preformed Ag NPs before and after electrospray, respectively, (iii) dark field microscopy image of the soft-landed Ag NPs, and (iv) plasmonic scattering spectra corresponding to each of the Ag NPs encircled in part iii. Republished with permission of The Royal Society of Chemistry, from Ahuja, T.; Ghosh, A.; Mondal, S.; Basuri, P.; Jenifer, S. K.; Srikrishnarka, P.; Mohanty, J. S.; Bose, S.; Pradeep, T. *Analyst*, **2019**, *144*, 7412−7420 (ref 3); permission conveyed through Copyright Clearance Center, Inc.

continued emergent use of plasmonic phenomena in realizing significant gains in measurement methodology, along with investigation of the fundamental physical processes that define plasmonic phenomena. This latter area has become so important and active that we devote an entire section of this review to description of advances in plasmonics. Continued creative development of more traditional techniques and newer techniques introduced within the past few decades have propelled researchers to answer important questions in chemical and biochemical measurement science using these tools.

Selected works in these areas have been chosen for their perceived importance in advancing surface and interface analysis methods or for their use in answering critical questions about chemical or biochemical events at interfaces or on surfaces. We have organized these advances into six broad categories that are admittedly overlapping in many cases: plasmonics, surface imaging, catalysis, electrochemical systems and corrosion, materials systems, and biological surface and interfacial phenomena. We recognize that these same works could be organized in different ways with equal clarity; our organization was chosen simply for convenience. Some subtopics covered here have overlap with more focused reviews that have been published in *Analytical Chemistry* over the past several years. In these cases, we have sought to update the status of these areas as they pertain more broadly to surface and interface analysis but not to fully replace the in-depth content of these previous reviews.

As noted in the Acknowledgments, we have dedicated this review to ***Professor Richard P. Van Duyne*** whose initial discovery of surface enhanced Raman scattering (SERS) in 1977 and his prolific work in plasmonic phenomena more broadly up until his untimely passing motivated generations of researchers around the world to pursue work in these areas.

■ OPTICAL SPECTROSCOPY METHODS BASED ON PLASMONIC ENHANCEMENT

Advances in the understanding of surface plasmons and localized surface plasmons has led to the continued expansion of plasmonics in the analysis of surfaces and interfaces. Although the well-known technique of SERS has dominated the field, a myriad of other techniques, substrates, and processes are emerging that are playing larger roles in chemical and biochemical analysis. Improved control of plasmonic phenomena has also led to advances in inducing and controlling surface and interfacial chemical processes such as catalysis. The use of surface plasmons has served as the basis of new analytical techniques, while plasmonic effects have also been successfully integrated with older methods to enable fresh approaches to analytical problems.

Advances in Surface Enhanced Raman Scattering Substrates and Methods. The utilization and refinement of plasmonic nanoparticles (NPs) as SERS substrates continues to be of intense focus. Highlighting these advances, a review by Haynes and co-workers covers strategies for stabilizing NPs to extend their lifetimes in various environments.[2] Much work has been done to extend NP stability and lifetime to expand the temporal window for longer-term experiments, while at the other end of the temporal spectrum, efforts to improve NP stability for use in ultrafast plasmonic spectroscopies where heating is more extreme has also been reported.

The development of cost-effective, rapid, scalable, and reproducible fabrication methods for robust substrate preparation that utilize recent advances in nanomanufacturing is critical. Such approaches have traditionally drawn from different fields of science and engineering with some even borrowing from techniques such as mass spectrometry. Adopting such unconventional practices has led to the development by Pradeep and co-workers of a novel technique called ambient electrospray deposition Raman spectroscopy (AESD-RS).[3] In this approach, a modification of one first reported by Cooks and co-workers,[4] a uniform distribution of preformed NPs is soft-landed using electrospray deposition onto an analyte sample deposited on a transparent conductive glass substrate such as indium tin oxide (ITO). The SERS analysis is then performed with epi-illumination of the assembly through the back of the conductive glass substrate as shown in Figure 1. This approach allows analysis of a diverse array of sample types within a short period of 4−6 min including sample preparation time. These authors demonstrated the use of this approach for investigation of *p*-mercaptobenzoic acid (p-MBA), 2,4-dinitrotoluene, and *Escherichia coli* using preformed citrate-capped Ag NPs dropcast onto ITO substrates. Enhancement factors of 10^8 were reported with analyte sensitivities down to the nanomolar level. In a follow-up study, these researchers used this approach to explore time-dependent changes in molecular orientation of a series of simple molecular thiol probes, p-MBA, benzenethiol, and cyclohexanethiol precast onto an ITO surface.[5] Overall, soft landing of preformed Ag NPs using AESD-RS was demonstrated as a robust method for preparing SERS substrates suitable for rapid detection and semiquantitative analysis of target analytes.

In another substrate advance, Cetin et al. developed a novel, cost-effective and reliable fabrication method to produce 50 μm × 50 μm plasmonic substrates consisting of nanomushroom antenna with sub-10 nm plasmonic gaps for SERS.[6] This fabrication approach resulted in control of the gap between adjacent metallic nanomushrooms to 5 nm with 90% homogeneity and resulting in Raman enhancement factors of more than 10^8. The manufacturing of such arrays with high homogeneity is a step toward achieving the goal of robust, homogeneous, large-area SERS substrates for a variety of applications.

The ability to modulate the optical properties of nanostructured metallic surfaces in response to stimuli would enable the fabrication of reactive optical substrates for photonics-based applications. Edel and Kornyshev and co-workers achieved this tunability through the design and assembly of a SERS substrate whose optical properties can be modified through application of a potential.[7] The SERS substrate consisted of 40 nm Au NPs functionalized with p-MBA in two-dimensional arrays with a TiN-coated planar Ag film as the working electrode. As the applied potential is increased relative to the potential of zero charge (pzc) for the substrate from 0.1 to 0.7 V vs pzc, the NPs form an array on the substrate surface as the result of electrostatic forces between the NPs and the electrode. Interestingly, between 0.1 and 0.3 V vs pzc, the p-MBA SERS signal increases linearly as more NPs are attracted to the electrode surface, although the signal-to-background is poor. Between 0.4 and 0.7 V vs pzc, a rapid increase in signal is observed from both the increased NP coverage and the plasmonic coupling that this increased coverage induces with a shift in the localized surface plasmon resonance (LSPR) toward the excitation wavelength. The ability to turn "on" the sensor at potentials >0.7 V vs pzc and "off" at potentials <0.4 V vs pzc makes the sensor function controllable. The ability to form and then remove NP arrays make this a plausible approach for reusable SERS sensors.

Using an innovative SERS substrate, Van Duyne and co-workers integrated a microneedle array SERS substrate with the Raman reporter p-MBA to sense the pH of the interstitial fluid in biological systems.[8] The microneedle array was fabricated from commercial polymeric adhesive and coated in gold, representing the first use of such a technique to fabricate such an array. The robust nature of the film was validated by multiple insertions and retractions from both model and human skin without damage, displaying excellent biostability during these tests. The reversible and reproducible nature of the microneedle array paves the way for such plasmonic systems to be utilized in future work investigating biological process without disrupting the systems being analyzed.

Following a similar approach, Dong and co-workers designed a SERS-active microneedle array with two grooves containing redox-sensitive and pH-sensitive SERS probes to allow multimodal detection.[9] These microneedle arrays were used to assess differences in physiological environments in a rat model for arthritis. Using anthraquinone-2-carboxylic acid as the redox probe and p-MBA as the pH-sensitive probe, statistically significant differences in interstitial pH and oxidative environment were found for probes inserted into the joints of healthy and arthritic rats.

Fabrication of ultramicroelectrodes is a cost-effective approach compared to typical manufacturing methods necessary for SERS substrates. Capitalizing upon this, Tian et al. developed a new technique, microphotoelectochemical SERS (μPEC-SERS), which utilizes an ultramicroelectrode whose dimensions match the laser spot size.[10] This enables the simultaneous collection of a SERS spectrum and the photocurrent resulting from a potential hot-electron transfer event. Using μPEC-SERS to investigate the reaction of *p*-aminothiophenol to dimercaptoazobenzene, it was found that the activated oxygen species created by hot-electron transfer are more oxidative than those produced in conventional electrochemical oxygen reduction reactions. Such findings highlight the current convolution of new SERS substrate development with the recently realized, more complex plasmonic phenomena. Nonetheless, this newest generation of SERS substrates has attained surface morphology control at the nanoscale while retaining adequate enhancement factors.

For next-generation substrates, understanding and controlling the effects of multicomponent plasmonic NPs and nanostructures is essential. This aspect of substrate development is covered in greater detail in a recent review by Nam and co-workers[11] wherein multicomponent nanoparticles are defined as "hybrid structures composed of two or more condensed nanoscale domains with distinctive material compositions, shapes, or sizes."[11] Taking advantage of such nanostructures, Chen et al. developed a floating nanoarray (FNA) SERS sensor that concentrates target analytes either by surface charge or polarity.[12] The array was constructed of Pt−Pd NPs with the final assembly diameter of <100 nm with a quasi-ordered assembly. The porous FNA has a broad surface plasmon resonance (SPR) that covers the majority of the visible range. Using this FNA SERS sensor, aqueous malachite green was detected at the 1 ppm level, although the authors note that this approach requires additional work to understand interactions at the FNA surface.

Taking a cue from nature, Stone and co-workers constructed a NP sphere as a core with "tentacles" extending outward ∼15 nm, each decorated with a 5 nm Au NP sphere.[13] This creates numerous plasmonic interactions between the tentacle and core NPs. This nanoassembly benefits from the resulting intense LSPR across the "biological optical window" of 650−1100 nm and provides better enhancement than its satellite core components. This assembly enabled detection of multiple SERS labels within the concentration range of nM to mM providing a method for analysis in biological systems. The unconventional nature of this "octopus"-like structure yields unique detection capabilities with both the core and tentacles potentially playing discrete sensing roles in future work.

In a different approach, Wang and co-workers constructed a hydrophilic Au porous structure (hydro-GPS) based on Au NPs assembled on the tip of a tetraoctylammonium-modified glass nanopipet and cross-linked using 3,6-dioxa-1,8-octanedithiol as a strongly enhancing SERS substrate to investigate ion transport through nanopores.[14] A combination of electroosmotic and electrophoretic flow allows passage of a neutral Raman reporter molecule, 4-methoxyphenyl isocyanide (MOPI), into and eventually through the hydro-GPS assembly. The potential- and temperature-sensitive $\nu(\mathrm{N{\equiv}C})$ mode of MOPI allows monitoring the overall potential of the hydro-GPS assembly that results from differences in electrophoretic and electroosmotic flow through the assembly and temperature changes due to Joule heating. The ability to probe localized ion flow has the potential to provide new insights into confined mass transport.

To investigate surface−NP interactions at the single particle level, Baumberg and Nijs and co-workers utilized a super-efficient plasmonic nanoarchitecture for Raman kinetics (SPARKS)[15] to monitor 3-mercaptopropionic acid (MPA) on a single NP.[16] SPARKS is a further refinement of the nanoparticle-on-mirror approach (NoPM)[17] in which NPs are partially embedded in an organosilica nanolens that increases the SERS signal by 100 times over either the NoPM or the related nanocube-on-mirror approach.[18] The MPA forms a self-assembled monolayer (SAM) on template-stripped Au with the SPARKS NPs deposited on top. Upon irradiation at pH 7, MPA can exist in one of three unique states: protonated, deprotonated, or monodentate; at pH 4, MPA exists in unbound, monodentate, and bidentate states. The different states are monitored through the response in the $\nu(\mathrm{C{-}OH})$ region at pH 7 or the $\nu(\mathrm{Au{-}S})$ region at pH 4. The temporal resolution of the technique allows tracking interconversion of the states at pH 7 wherein the protonated and deprotonated forms comprise a majority. In contrast, at pH 4, all three states coexist, linked by an interconversion pathway with the monodentate as an intermediate between the unbound and bidentate states. The ability of SPARKS to facilitate kinetics-based monitoring on the sub-100 ms time scale should make this tool extremely useful in the study of reactive chemical systems.

Improving the sensitivity of Raman detection for biological molecules, Cheng and co-workers introduced plasmon-enhanced stimulated Raman scattering (PESRS) to image biomolecules released from cells.[19] To achieve single-molecule detection sensitivity, they utilized low energy, 80 MHz chirped laser pulses to avoid sample damage and allow fast chemical mapping. Their data analysis scheme utilized a penalized least-squares approach to extract Raman bands of interest from the broad non-Raman background followed by a block-matching and 4D filtering algorithm to further denoise their data resulting in high-quality stimulated Raman spectral data. Proof of concept experiments were performed for adenine on Au nanoparticles. Stimulated Raman scattering (SRS) signals were reported in single pixel mapping with single-molecule sensitivity. In dynamic experiments, they were further able to acquire PESRS mapping of adenine secreted from bacteria on a nanoparticle plasmonic substrate. This responsive technique represents a new approach for vibrational imaging of low-concentration molecules in a fast and highly sensitive manner. The results here suggest that PESRS should be applicable to a broad array of surface types including membranes or catalysts.

Ren and co-workers developed a clever approach to measure the temperature of plasmonic Au nanoparticles by utilizing a temperature-dependent shift of the SERS signal of the $\nu(\mathrm{N{\equiv}C})$ band of phenyl isocyanide with a sensitivity of 0.236 $\mathrm{cm^{-1}}$/°C in a cell culture medium.[20] They attributed a slight broadening and a shift to lower frequencies of the $\nu(\mathrm{C{\equiv}N})$ band at ∼2200 $\mathrm{cm^{-1}}$ to an orientation change of the phenyl isocyanide on the Au NP surfaces with increasing surface temperature up to the limit of their plasmonic heating to 80 °C and applied this to the investigation of local temperature changes in living cells. Functionalized Au NPs were used to monitor both changes in the $\mathrm{Ca^{2+}}$ transport in a living cell under different local temperature variations as well as a metabolic rate under different culture temperatures.

Adopting a different approach to utilizing NPs on a substrate, Li created a nanoantenna-based remote enhanced Raman spectroscopy technique consisting of matched nanoantenna pairs.[21] Following an excitation-collection-separated plasmonic approach, a Ag nanowire acts as the receiving antenna that launches surface plasmon polaritons (SPPs) in a Au mirror substrate. A Ag nanocube acts as the transmitting antenna which collects the near-field signals and converts them into detectable far-field signals. The two antennae are bridged by the propagating SPPs and are both physically and functionally separated from one another. This design philosophy enables a high signal-to-noise ratio by limiting the photothermal noise from direct excitation and can be utilized in applications where signal-to-noise ratio (S/N) is currently an issue.

Advances in the development and understanding of substrates for the SERS approach of tip-enhanced Raman spectroscopy (TERS) have also been reported. Standardization of enhancements attained for different TERS geometries is necessary for interlaboratory comparison and comparing results from one experimental geometry to another. To this end, Rossi and co-workers determined enhancement factors for reporter molecules in monolayer-coated tips used in three configurations: isolated as single tips, a tip−tip dimer geometry, and a more conventional TERS gap mode geometry in which the tip is brought close to a Ag or Au metallic substrate.[22] The use of a Raman reporter-modified tip eliminates most of the uncertainties associated with scanning probe microscopy control of tip−surface separation and, hence, TERS intensities. Enhancement factors were compared among these geometries utilizing a single excitation source and collection system to allow for appropriate comparison using monolayers of thiophenol, 7-mercapto-4-methylcoumarin, and thiram as Raman reporters. Although absolute enhancement factors varied between Raman reporter molecules, enhancement factors were uniformly determined to be in the order tip−tip dimer > TERS gap mode > isolated tip mode. The isolated tip approach consistently resulted in the enhancement factors that were about 2.2 times lower than for the standard TERS gap mode. Further, the tip−tip dimer geometry consistently had the highest enhancements, with enhancement factors that were about 3 times larger than the standard TERS gap mode geometry. This work is critical in establishing a uniform comparison approach that allows the laboratory-to-laboratory enhancement factor to be reliably compared and benchmarked.

With the increased adoption of nanostructures in SERS applications, the visualization of optical fields and LSPRs is critical in optimizing development and implementation. Utilizing work first report by Bhattarai and El-Khoury[23] and advancements in tip manufacturing, Verma and co-workers functionalized a single side of an atomic force microscopy (AFM) tip with a Raman reporter to image the optical field and LSPRs of nanostructures using TERS.[24] By depositing Ag NPs onto a single side of a silicon AFM tip, these researchers developed a route for selective functionalization with the Raman reporter *p*-nitrobenzenethiol (4-NBT) for side-selective TERS. Imaging plasmonic Au nanotriangles by TERS at the Raman spectral modes for p-NBT, the $\nu(\mathrm{C{-}S})$ at 1080 $\mathrm{cm^{-1}}$ and the $\nu(\mathrm{C{=}C})$ at 1580 $\mathrm{cm^{-1}}$ were used to visualize the local near-field by monitoring changes in the Raman intensity. Orientation of the nanotriangle on the surface results in different intensities indicating that the probe is sensitive to the local optical field and its orientation and not just proximity to the nanotriangles. The LSPR at 710 nm was identified from the difference in intensities between the 1080 and 1580 $\mathrm{cm^{-1}}$ bands resulting from differences in the LSPR extinction coefficient at the corresponding wavelengths. Further development of methods such as TERS, whose signal levels are sensitive to the local optical field, will aide in better design of nanostructures for use in various applications.

In improvements to the routine application of TERS, Park and Raschke and co-workers developed a method for dynamic wavefront shaping of the excitation field for adaptive TERS (*a*-TERS) and adaptive tip-enhanced photoluminescence (*a*-TEPL) to overcome limitations from inconsistent signal levels due to differences in tip size, shape, and roughness and difficulty in polarization resolved measurements.[25] Dynamic wavefront shaping at the tip apex occurs with the adaptive optics of a spatial light modulator that dynamically controls the LSPR with feedback from a deep learning algorithm. In analysis of a $\mathrm{WSe_2}$ monolayer (ML) supported on a Au substrate, the optimization algorithm increased the *a*-TEPL signal by a factor of 2 over normal TEPL and by a factor of 4.4×10^4 over far-field photoluminescence of the $\mathrm{WSe_2}$ ML. Near-field polarization control at the tip was demonstrated in studies of spin-coated layers of isotropic brilliant cresyl blue (BCB) molecules. Although the far-field signals of a several layer-thick film of BCB are too weak to be detected, strong *a*-TERS signals are observed depending on the wavefront shaping condition. In addition to optimized *a*-TERS signals that are 2 times that observed with conventional TERS, a new vibrational band emerges at 613 $\mathrm{cm^{-1}}$ for a combination of $\delta_{\mathrm{op}}(\mathrm{C{-}C})$, $\rho_{\mathrm{t}}(\mathrm{O{-}C_2})$, and $\rho_{\mathrm{t}}(\mathrm{N{-}C_2})$ modes from the symmetry-selective plasmon-phonon coupling at the tip under these polarization control conditions. This approach to adaptive nanoimaging represents a generalized solution for reliable field enhancement in tip-enhanced spectroscopies which should be extendable to plasmonic cavities as well.

In addition to SERS using conventional metallic substrates, work has continued on the use of semiconductor substrates for SERS. Alamri developed a 2D $\mathrm{MoS_2}$/graphene van der Waals heterostructure substrate decorated with Au NPs.[26] This SERS substrate yielded an enhancement factor 1 order of magnitude greater than can be achieved with Au NP-decorated graphene substrates due to enhanced dipole−dipole interactions at the heterostructure interfaces which increase the contribution from chemical enhancement. Although optimizing chemical enhancement is not a typical route for improving SERS substrate performance due to the limited range of additional enhancement possible through this mechanism, this work does represent a novel advance in SERS substrate fabrication.

Alshareef and co-workers further expanded the utility of monoclinic $\mathrm{MoO_2}$ for plasmonic applications by creating nanostructures that support specific and tunable longitudinal and transverse surface plasmon modes.[27] These researchers demonstrated tuning of geometry-dependent surface by control of either the shape or thickness of $\mathrm{MoO_2}$ nanostructures. Theoretical calculations supported the strong plasmonic behavior of the monoclinic $\mathrm{MoO_2}$ through extensive delocalization of electrons in Mo d-orbitals. This work provided a significant advance in tailoring surface plasmons of nonconventional metallic nanostructures and highlighted the potential of $\mathrm{MoO_2}$ nanostructures for possible micro−nano optical and optoelectronic applications.

Cao and co-workers attained higher enhancements and greater sensitivity by constructing $\mathrm{MoO_{2-\mathit{x}}}$ nanospheres containing oxygen vacancies through the Li metal grinding reduction method.[28] These nanospheres produced higher Raman enhancements through a chemical enhancement mechanism due to the promotion of charge transfer between the defective metal oxide and the surface analyte. These nanospheres supported detection limits of 10^{-8} M for rhodamine 6G (Rh6G), a 10-fold improvement over non-vacancy $\mathrm{MoO_2}$ NPs.

Wu and co-workers used black $\mathrm{TiO_2}$ NPs with a crystal core-amorphous shell structure as substrates for SERS.[29] Strong SERS in these systems was proposed to arise from efficient interfacial photoinduced charge transfer due to the strong synergistic effect of the novel crystal- amorphous core−shell structure of the black $\mathrm{TiO_2}$ NPs. The high-efficiency exciton transition of the crystal core provides photoinduced charges with effective exciton separation and charge injection at the crystal core-amorphous shell interface. The enrichment of these photoinduced charges in the amorphous shell facilitates interfacial photoinduced charge transfer between the substrate and target analyte molecules at the surface of the shell, leading to strong SERS activity in the visible and near-IR regions with enhancement factors of $\sim 4 \times 10^5$. These researchers demonstrated the utility of these NP substrates for SERS detection of drug-resistant breast cancer cells.

Non-SERS Plasmon Enhanced Spectroscopies. Plasmonic enhancement has been used in spectroscopic methods other than Raman scattering. Busson and Dalstein used NP spheres deposited onto adsorbate-modified substrates for plasmon enhancement of vibrational sum-frequency generation (vSFG) spectroscopy.[30] Although paradoxical at first glance, this approach overcomes the low intensity experienced with vSFG from interfacial systems of low adsorbate coverage and, hence, modest molecular orientation. Due to the need for inversion symmetry, vSFG has traditionally been limited to high surface coverage systems with a requisite need for greater molecular ordering and orientation. A signal amplification factor of 7.1 was experimentally measured for a monolayer of aminopropyltriethoxysilane deposited on a Si substrate that was overcoated with a layer of 13.5 nm-diameter Ag NPs. Unsurprisingly, it was found that Ag NP spheres produced the highest plasmonic enhancement.

The use of shell-isolated nanoparticle enhanced (SHINE) approaches for plasmonic enhancement of spectroscopic signatures has continued to gain popularity after the introduction of shell-isolated nanoparticle enhanced Raman scattering (SHINERS) by the Tian group almost a decade ago.[31] The utility of SHINE approaches derives from the presence of a chemically inert shell and the presence of a strongly plasmonic core. This “smart dust” has now been used to provide plasmonic enhancement in other types of analytical spectroscopies.

He and co-workers used Au core-silica shell SHINE for plasmonic signal amplification in vibrational SFG and difference frequency generation (DFG) in methods termed SHINE-SFG and SHINE-DFG.[32] As a test analyte, *p*-mercaptobenzonitrile (p-MBN) on a Au surface was used to quantify enhancement factors relative to normal SFG for a series of SHINE with varying silica shell thicknesses under different polarization conditions. The enhancement factor was found to be $>10^5$ for SSP-polarized SHINE-SFG when using SHINE NPs with a 2 nm-thick SiO_2 shell. Thinner shells resulted in stronger plasmonic enhancements with consequently larger EFs. Additionally, nonlinear coupling of the SFG signal and the difference frequency generation (DFG) signal was found to provide a new enhancement regime. The development of SHINE-SFG and the coupled effects of SHINE-DFG are new nonlinear coherent spectroscopic tools. In addition, the observation of SFG and DFG signal coupling suggests a rational strategy for development of enhancing substrates to take optimal advantage of these coupled spectroscopic phenomena.

Building on previous efforts by Aroca and Geddes,[33,34] Li and co-workers used SHINE enhancement of phosphorescence (SHINEP) to investigate the shell thickness dependence of emission quenching by energy transfer to the metal surface in a plasmonic cavity.[35] As a demonstration of this approach, $[Ru(bpy)_3]^{2+}$ was used as the phosphorescent emitter to provide a suitably long radiative lifetime. Two configurations were investigated: coupling and noncoupling. In the couple configuration, the $[Ru(bpy)_3]^{2+}$ emitters are sandwiched between a 2 nm-thick SiO_2-coated Ag substrate and core−shell Ag@SiO_2 NPs deposited onto the $[Ru(bpy)_3]^{2+}$ layer, whereas in the noncoupled configuration, the $[Ru(bpy)_3]^{2+}$ emitters are sandwiched between a quartz substrate and the overcoated Ag@SiO_2 NPs. Compared with the previously reported phosphorescence enhancement factors of 2−9, enhancements of >330 were realized in the coupling configuration at an optimal silica shell thickness of 6 nm. Additionally, the radiative emission rate was accelerated by a factor of almost 125 in the coupled mode by decreasing emission losses due to energy transfer. Not surprisingly, emission from $[Ru(bpy)_3]^{2+}$ in the coupled mode exhibited larger enhancements than in the noncoupling mode, although the maximum emission intensity realized in the noncoupled mode occurred a slightly larger silica shell thickness of 10 nm relative to the coupled mode due to a different balance of radiative and nonradiative decay processes. Collectively, these results suggest approaches to improving photostability of emitters by reducing the lifetime in the excited state. This makes SHINEP a promising tool for control of distance-dependent plasmon-enhanced emission spectroscopies.

In an alternative application of SHINE, Li and co-workers developed a plasmonic substrate for simultaneous plasmon-enhanced single-molecule Raman and fluorescence spectroscopy using a plasmonic nanocavity.[36] The nanocavity consists of a Ag substrate coated with a 2 nm-thick silica layer with Ag shell-isolated NPs deposited on top. The dielectric shell of the NPs prevents surface quenching of fluorescence by the NP while still generating a plasmonic hotspot for Raman scattering. Investigating the single-molecule photoinduced reaction of rhodamine B isothiocyanate with time with 50 ms time resolution, four distinct time regimes were observed that resulted in the ultimate cleavage of the C−C bond between the xanthene and phenyl moieties. The fluorescence and Raman signals remained unchanged until 12.65 s, but between 12.65 and 15.05 s the disappearance of the fluorescence signal at 576 nm and the Raman bands at 1519 and 1654 cm^{-1} indicate a structural transformation on the NP. Between 15.05 and 15.70 s, the maximum fluorescence wavelength shifted slightly red to 580 nm, but no significant changes were observed in the Raman intensities. This period was followed by another fluorescence shift at 15.70 s to 591 nm accompanied by a shift of the Raman bands at 1519 and 1654 cm^{-1} to 1500 and 1652 cm^{-1}, respectively. Through correlation of the fluorescence and Raman signals, the four stages in the single-molecule reaction of a C−C bond could be uniquely identified as first, a structural transformation from the free acid to the lactonic species with subsequent decarboxylation and, finally, phenyl group removal to leave the intact xanthene moiety. These combined optical spectroscopy techniques represent a powerful tool for monitoring single-molecule chemistry at the single NP level.

Strong coupling of single quantum dot (QD) emitters with plasmonic nanocavities gives rise to a hybrid state of a plasmon and an exciton called a plexcitonic state. Raschke and co-workers developed tip-enhanced strong coupling (TESC) spectroscopy and imaging based on scanning probe microscopy to obtain unambiguously photoluminescence (PL) spectra with Rabi splitting from plexcitonic states of nanocavity-trapped isolated QDs that allows measurement and control of quantum effects at the nanoscale.[37] In their system, a scanning plasmonic antenna tip and metal mirror substrate form a nanocavity to control and enhance the plexcitons. A HeNe laser is used for excitation and focused on the tip, with the PL signal collected in a backscattering configuration. These researchers demonstrated TESC on QDs and observed that changing tip position rapidly and reversibly changes coupling strength, indicating a degree of quantum dynamic control. These researchers emphasized that this technique can be extended beyond plexciton measurement and control to other types of quantum states including infrared vibrational resonances by changing variables such as transition dipole moment of the QDs or tip parameters. Expanding this technique to other quantum states might offer active and dynamic control of different photochemical pathways of single molecules.

A novel system developed by Litvin and co-workers utilizes semiconductor plasmonic nanocrystals (PNCs) to increase the optical response of near-infrared PbS QD emitters.[38] The PNCs were constructed from $Cu_{2-x}Se$ in poly(vinyl alcohol) yielding a LSPR centered at ∼1150 nm. This LSPR was coupled to the PbS QDs and yielded a 3-fold enhancement of the photoluminescent intensity. Interestingly, the PL spectra were blue-shifted and had a longer-lived photoluminescent decay due to high amplification of the trap-related PL from the higher-lying states of the QDs. This effect could be further enhanced by better control of the $Cu_{2-x}Se$ PNC and PbS QD concentration and spatial distribution. This work defines a potential strategy for fabricating nano- and micrometer-sized light sources with the possibility of miniaturization of the technology for hand-held devices or nanospectroscopy systems.

In another microscopy technique development, Wickramasinghe and co-workers developed stimulated Raman (SR) photon-induced force microscopy (PiFM) in a noncollinear configuration using a monolayer of 4-nitrobenzenethiol on a 30 nm Au NP as a proof-of-concept Raman reporter.[39] In this approach, stimulated Raman nanoscopy is achieved without resonance Raman enhancement using near-field photon-induced forces instead of the more conventional optical detection in the far-field. By utilizing the second flexural eigenmode of the atomic force microscopy (AFM) cantilever instead of the first, the vibrating tip can be positioned closer to the sample film, improving S/N. These researchers estimated that at the point of maximum field enhancement for a Au-coated tip, this approach allows detection of fewer than 42 molecules.

In a different approach, Dietler and Sekatskii and co-workers developed a gap-plasmon enhanced photothermal-induced resonance (PTIR) technique which uses visible light instead of the typical IR radiation to improve spatial resolution to 5 nm.[40] In this approach, Au tip−Au substrate gap plasmon resonances are efficiently induced by visible wavelength radiation which, when resonant with an electronic absorption process of a thin film sample, induces thermal expansion that results in mechanical deflection of the AFM cantilever. Small changes in the thickness of a sample can lead to large changes in the electromagnetic field amplification in the Au tip−substrate gap region, thereby improving resolution and contrast of the images. To test this system, analysis of a methylene blue-stained amyloid fibril was performed. The PTIR-amplitude map provides a significant improvement in imaging relative to the AFM height mode, and the additional contrast indicates that the fibrils are not as smooth as the AFM height trace makes them appear. The use of visible wavelength light and gap-plasmon enhancement offers a new approach to increase resolution and sensitivity that typical PTIR systems have not yet utilized.

Harnessing plasmonic enhancement to drive the coherent exchange of optical near-fields, Lienau and co-workers developed a new spectroscopic technique called plasmonic nanofocusing scattering spectroscopy that allows measurement of the coherent exchange of optical near fields between neighboring dipoles.[41] In their approach, evanescent field coupling between the plasmon resonance of a single Au nanorod and a conical Au nanotaper when it is positioned close by is sensed through measurement of coherent light scattering from the tip with 5 nm lateral resolution. This is achieved by launching SPPs along the nanotaper that are then nanofocused at the apex of the tip. The strong SPP field in the near-field around the apex is due to the evanescent mode, and the field is converted into far-field radiation only at the apex of the taper, resulting in highly localized scattering. This scattering emission has a field distribution which matches that of an isolated dipole moment orientated along the taper axis and creates emission with virtually no background. At plasmon energies of a nearby nanorod, the coherent scattering intensity is diminished. This approach can be used to investigate single NPs with high S/N and high spatial resolution and should be applicable for investigation of vectorial near-field coupling that occurs in plasmonics, photocatalysis, and energy transport.

Utilizing plasmonic enhancement tip−substrate gap mode nanocavity-based techniques for applications different from those discussed above, Van Duyne and co-workers utilized the newly developed technique of tip-enhanced Raman excitation spectroscopy (TERES).[42] In this approach, different excitation wavelengths result in different near-field intensities in the nanocavity between a Au tip and a Au substrate due to the possible existence of numerous gap-mode plasmon resonances. This allows excitation of gap modes over a wide spectral window depending on the characteristics of the tip (material, radius of curvature) and substrate (material, distance from tip). Investigation of gap-mode nanocavities for a Au tip−Au substrate combination for the Raman reporter biphenyl-4-thiol in the ambient and in aqueous media resulted in significant signal enhancement with increasing wavelengths beyond 600 nm with a wide plateau at longer wavelengths. In the aqueous environment, this profile was red-shifted by 80 nm due to refractive index effects. The added flexibility for the excitation of electronic resonances makes this approach applicable to multicomponent systems in different dielectric environments. This technique also shows promise in coupling the nanocavity plasmon modes with molecular or dark exciton transition for facilitating chemical reactions and quantum optoelectronic applications.

Adopting an alternative TERS approach, Park and Rho and co-workers developed a room temperature, triple-sharp-tips plasmonic cavity for TEPL of low quantum efficiency localized excitons in 2D semiconductors.[43] This new configuration overcomes the signal limitations of both static cavity and optical spectroscopy arising from the much more intense neutral exciton emission, X_0, through a bowtie nanostructure utilizing two sharp tips of nanotriangles while a position-controllable third tip, a Au AFM tip, moves across the bowtie nanogap with <15 nm spatial resolution. This configuration results in 4.0×10^4-fold enhancement in the localized exciton photoluminescence, X_L, through the Purcell effect in the nanoconfined cavity. As a model system, a WSe_2 ML was deposited over the bowtie to induce a slight strain in the film over the gap. Imaging across the bowtie gap showed fluctuations in the TEPL signal for X_L regardless of position in the gap. In contrast, X_0 photoluminescence does not change with tip position across the gap, allowing selective identification of the weaker X_L emission. The ability to control and image localized exciton photoluminescence under ambient

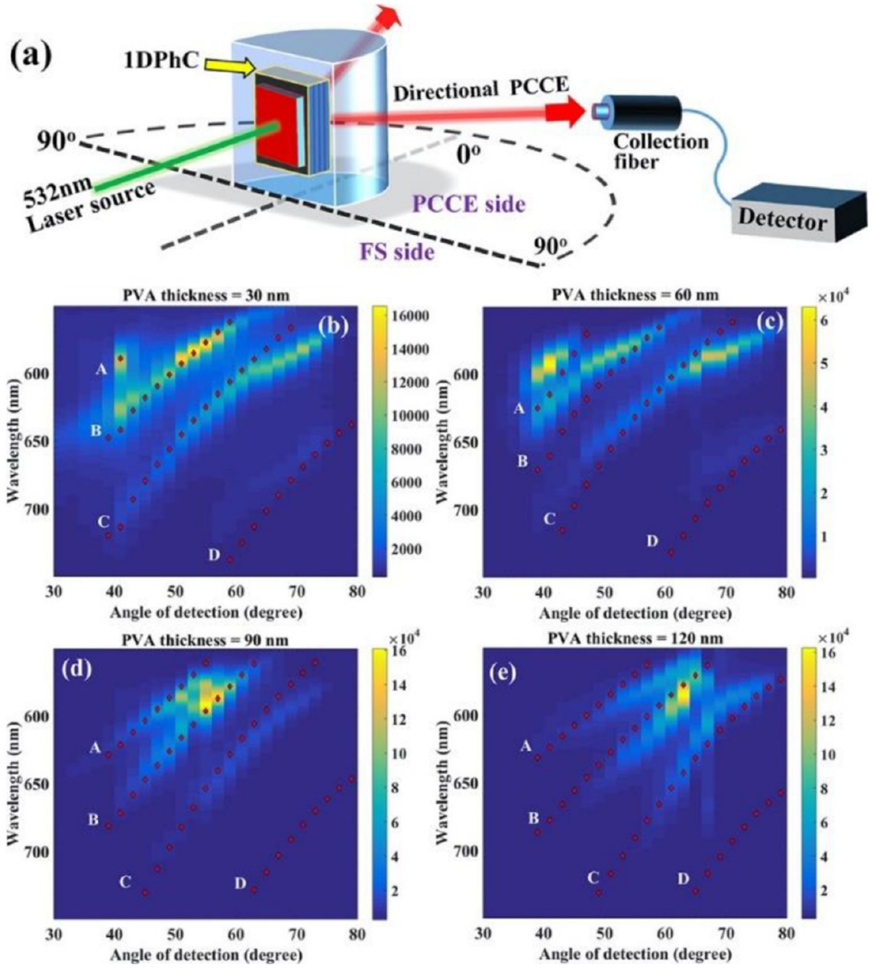

Figure 2. (a) Schematic of PCCE optical setup with 1DPhC position indicated on the prism with excitation in the reverse Kretschmann configuration. Photonic crystal coupled emission from Rh6G for the 1DPhC/PVA structure for PVA layers of varying thickness from 30 to 120 nm (b−e). The color bar scale represents fluorescence intensity in arbitrary units. The red dots represent BSW and IOMs from the numerically calculated dispersion diagram. Reprinted with permission from Bhaskar, S.; Das, P.; Srinivasan, V.; Bhaktha B. N, S.; Ramamurthy, S. S. *J. Phys. Chem. C* **2020**, *124*, 7341−7352 (ref 44). Copyright 2020 American Chemical Society.

conditions in an ML film at room temperature with high spatial resolution should usher in a new era for the study of photoemission in other low dimensional materials.

In another novel method advance, Bhaktha and Ramamurthy and co-workers fabricated a plasmon-free photonic crystal-coupled emission platform (PCCE) to capitalize on internal optical modes (IOMs) and large electromagnetic (EM) fields created largely at the surface due to Bloch surface waves (BSWs) of a one-dimensional photonic crystal (1DPhC).[44] The PCCE platform was constructed from 1DPhC of eight pairs of quarter-wave thick alternating layers of TiO_2 and silica on a fused silica substrate overcoated with a layer of poly(vinyl alcohol) (PVA) of varying thickness. This assembly was affixed to a hemicylindrical prism in a reverse Kretschmann configuration as shown by the instrument schematic in Figure 2. The thickness of the dielectric spacer layer and the PVA film along with excitation wavelength affect the IOMs, the BSWS, and the photonic stop bandgap of the one-dimensional photonic crystal such that they are tunable to allow optimization of fluorescence emission enhancement in the absence of plasmonic modes for the fluorophore Rh6G (see Figure 2). This PCCE platform provided an enhancement in fluorescence emission of ~44-fold, which is considerably better than the 5−10-fold enhancement reported for surface plasmon coupled emission platforms. As a demonstration of utility, these researchers used this platform to detect Al^{3+} in solution with a limit of detection (LOD) of 0.21 parts per quadrillion (~1 fM). This technique needs additional work to realize its full potential, but the impressive results shown here provide a foundation optimization of PCCE platforms. The LOD demonstrated by this system makes it a potentially important tool for detection of trace analytes and point-of-care diagnostic systems.

Building on earlier work of Altug and co-workers using vibrational mode-matched IR-resonant nanoantennas to perform surface enhanced infrared absorption (SEIRA),[45−48] Lea and co-workers coupled this approach to SEIRA with IR scattering-type scanning near-field optical microscopy (IR s-SNOM) for simultaneous imaging and spectroscopy at nanometer spatial resolution.[49] To couple these techniques, IR-resonant Au nanorod antennas are fabricated on a CaF_2 substrate and a Au-coated AFM tip is brought near the surface of the sample to create a tip-gap nanocavity within which combined SEIRA and s-SNOM processes occur. When illuminated with a quantum cascade laser polarized along the axis of an antenna with a plasmon resonance in the vibrational frequency region of interest, the sample on the antenna is bathed in the resulting evanescent field with the IR absorption further enhanced by the scattering of the evanescent field into the far-field by proximity of the Au-coated tip. These researchers were able to image a single monolayer of ferritin protein units through their amide I vibrational mode at ~1650 cm^{-1} with an estimated improvement in sensitivity of 3 orders of magnitude for SEIRA and an order of magnitude over conventional s-SNOM for proteins coupled to the antenna. Moreover, they demonstrated sensitivity to inhomogeneities in protein layer density to almost the single protein unit level. This zeptomolar sensitivity exceeds that previously published for these techniques and opens the possibility for true single protein characterization and imaging through this combined approach.

Conventional SEIRA has been used to investigate many chemical systems by researchers availing themselves of additional signal increases either through nanostructuring a metallic surface or employing arrays of metallic antennas. Taking this approach one step farther, Armelles and co-workers utilized a giant magnetoresistance metallic multilayer to modulate the resonance of the SEIRA platform.[50] Application of a magnetic field changes the resonance of a metasurface due to the magneto-refractive effect in which the surface optical constants change as a function of an electrical resistance change from an applied magnetic field. As a result of the direct role of conduction electrons in this phenomenon, the resonance modulation can cover a wide frequency range from the mid-infrared to the THz regime. To validate their method, these researchers fabricated an array of spintronic Au/$Ni_{81}Fe_{19}$ metallic multilayers covered with a poly(methyl methacrylate) (PMMA) layer as the IR probe species. The presence of the PMMA layer resulted in optical signal changes due to the PMMA bands at 1149, 1449, and 1724 cm^{-1} of 5, 3, and 9%, respectively, compared to the array without PMMA. In contrast, the magneto-refractive transmission spectra acquired in the presence of a magnetic field demonstrate much greater sensitivity to the presence of the PMMA with changes in the magneto-refractive response from the same three PMMA vibrational modes of 18, 30, and 27%, respectively. This work demonstrated that the magneto-refractive approach is more sensitive to the presence of analyte vibrations than the pure optical signals and provides an alternate SEIRA platform with additional signal enhancement from the spintronic substrate.

To better investigate biological samples, Zanni and co-workers combined a two-dimensional IR (2DIR) spectroscopy variant of attenuated total reflection in a reflection pump—probe geometry at an interface coated with a thin layer of plasmon-producing nanostructured Au to yield a hybrid technique called surface enhanced attenuated reflection 2DIR (SEAR-2DIR) spectroscopy.[51] Analysis of the amide I mode of a cysteine terminated α-helical peptide tethered to a Au surface in D_2O and H_2O was performed as a proof-of-concept and demonstrated the ability to use this approach with monolayer sensitivity even in the presence of strongly absorbing solvents. The secondary structure of the peptide was monitored during dehydration, and it was found that the α-helical form dominates the structure when both hydrated or dehydrated. These researchers demonstrated an enhancement of up to 20 000 when compared to the signal level for the same monolayer on a dielectric surface, with the enhancement originating from the change in optical density by increasing the third-order signal through plasmon enhancement while decreasing the local oscillator intensity. This development could have significant use in studies of interfacial structure with the possibility of extension to interfacial dynamics as well.

Using an atypical substrate, Altug and co-workers developed a novel resonant metasurface-based method for surface enhanced IR spectroscopy for detecting molecular fingerprint IR absorption over a broad spectral range by eliminating the spectrometer and instead adopting a compact angle-scanning refractometric plasmon resonance configuration.[52] The Ge-based-high-Q metasurface sensor is constructed of nano-photonic resonators capable of chemical-specific broadband IR detection. The spectral position being collected is controlled by the incident angle of the mid-IR light while the angle-multiplexed approach delivers multiple on-demand resonances limited only by the range of possible incident angles. Measurement of the analyte-induced light intensity change upon attaining the resonant condition across all angles enables visualization of the absorption spectrum without the need for a spectrometer. Impressively, this sensing scheme has a demonstrated surface mass sensitivity of 0.27 pg/mm for biomolecules such as polylysine, DNA aptamers, and human odontogenic ameloblast-associated protein molecules. The simplified detection scheme and low LOD highlight the recent advances made in plasmonic substrates.

Langhammer and co-workers developed a plasmonic heterodimer-based nanospectroscopy approach to monitor the kinetics of chemical transformations of metallic nanoparticles of importance in areas such as microelectronics and heterogeneous catalysis. For the specific analysis of metal nanoparticle oxidation, monitoring the plasmonic properties using visible wavelength spectroscopy works for the initial stages of oxidation but lacks optical contrast in the late oxidation stages of the metal NP when most of the NP has been converted to the oxide.[53] The heterodimer approach, in which the oxidation of one type of metal nanoparticle in a dimer is monitored through the coupled plasmon resonance of a different type of metal nanoparticle in the dimer, enables continuous self-referencing using polarized light to increase optical contrast to the polarization-sensitive plasmon resonance throughout the oxidation. This approach eliminates parasitic signals from polarization-independent isotropic changes in the reference NP part of the dimer or in the underlying substrate to boost S/N. By analyzing the oxidation kinetics of a 30 nm Cu NP in a heterodimer with a reference Au NP, it was found that the Arrhenius activation energy and preexponential factor correspond with the degree of NP oxidation with activation energy increasing and preexponential factor decreasing as oxidation progresses. These changes were attributed to a change in oxidation mechanism as the reaction progresses, due mostly to the evolution of the oxide grain structure. These findings clearly support the complexities of NP oxidation processes. More importantly from a chemical analysis perspective, the heterodimer approach described in this work opens the door to noninvasive investigation of NP chemistry including catalysis, even in corrosive environments.

Advances in Understanding Plasmonic Fundamentals. As plasmonic systems are increasingly incorporated into new and improving methods of analysis, it is critical to extend fundamental understanding of plasmonic phenomena to account for the plethora of new results that theory must explain.

Brolo and co-workers introduced a super-resolution imaging approach to investigate temporal and spatial fluctuations in signal intensity in single-molecule-surface-enhanced Raman spectroscopy (SM-SERS) experiments during this period. Such fluctuations are known to result from a complex array of contributions including molecular adsorption or desorption, surface diffusion, molecular reorientation, and metal surface reconstruction, and studying individual contributions has been challenging. Taking advantage of the different time scales for these processes, these researchers were able to investigate their contributions with some surprising results.[54] Using a new SM-SERS approach that probes single nanoparticle hotspot dynamics at a rate of 800 000 frames per second with ∼7 nm resolution, they showed that most of the nanoshell surface was inactive, containing transient hotspots that show short but intense phases of intensity fluctuations on the 10−100 μs time scale with longer darker periods of up to 10 ms. These results suggested that transient formation of hotspots from random atomic scale surface reconstruction was responsible for the sporadic SERS intensities involved. In a later related study, these researchers used this super-resolution approach to image dried SiO_2@Ag nanoshells coated with a monolayer of 5,5′-dithiobis(2-nitrobenzoic acid) on glass coverslips on an inverted microscope setup with a Zeiss Airysan detector.[55] Their results further demonstrated that the hotspot fluctuations from individual nanoparticles were spatially and temporally separated and exhibited discrete dependencies on excitation wavelength and polarization. Each nanoparticle was found to possess multiple hotspots exhibiting different enhancement factors and resonance conditions accessed with different illumination conditions. Plasmon resonances localized by atomic-scale roughness from reconstruction events at the nanoparticle surface play a significant role in the observed fluctuations, and hotspots supporting single molecules do not exhibit static intensities. These results provide significant insight into previously hidden dynamic effects in SM-SERS.

In an effort to resolve contradictory reports in the literature, Khlebtsov and co-workers studied the dependence of plasmon enhancement as a function of shape and aspect ratio of Au NPs.[56] These researchers used chemical etching to controllably reduce the aspect ratio of Au nanorods by decreasing nanorod length while keeping the shape and width identical. Only a weak correlation between the SERS response and the peak plasmon resonance wavelength was observed in apparent contradiction to the classical electromagnetic theory of SERS. Interestingly, reshaping the NP was found to have a larger effect on the SERS response than on tuning the plasmon resonance. Changing the typical Au nanorod shape to a dumbbell morphology yielded a 5-fold increase in SERS response. These results suggest that the rational design of NP shape has the potential to play a more important role in performance than tuning of the plasmon resonance to the excitation wavelength. These findings improve understanding of fundamental aspects of SERS enhancement and highlight the need for further work into the factors that govern plasmonic enhancement.

Further expanding the understanding of plasmonics, Kang and co-workers imaged the Chladni figure of the plasmonic charge density wave (p-CDW), or SPP, of a triangular Au optical resonator using power loss microscopy.[57] This p-CDW represents the photonic local density of states and a Chladni figure provides a quantum description of the two-dimensional standing wave that exists in the optical resonator. In contrast to near-field approaches to image the p-CDW, which are sensitive only to z-components of the wave, the use of diffraction-limited, all-optical, far-field power loss microscopy allows visualization of the full photonic local density of states. The scattering signal originates from interaction of the incident electromagnetic field and the nonuniform charge density of the metal surface. Imaging the Chladni figure of a gold triangle in real space provides a pathway for future work on the fundamental principles in plasmonic physics that were previously inaccessible.

To better understand electrical effects on the nanoscale, Shin et al. performed potential-dependent gap mode Raman spectroscopy utilizing either Ag or Pt NPs with a flat plate of either Ag or Pt as an electrode linked by 1,4-phenylene diisocyanide.[58] The metal-molecule-metal gap approach allows single-molecule analysis of the Raman shift of the symmetric isocyanide stretching vibrations, whose frequencies vary depending on which metal they are attached to, and how these frequencies vary with potential. These researchers found that the isocyanide group at the NP surface experiences a more enhanced effective potential than the one at the plate surface due to nanoparticle-induced effects rather than molecular resistance. The ability to precisely probe potential differences within a buried nanogap using spectroscopy enables the relative importance of plasmonic nanoparticle effects and molecular resistance effects to be assessed. This approach has the potential to enable optical hotspot distribution within a buried nanogap to be measured.

In working to understand factors that control how the distributions of hot electron and holes evolve after photoexcitation in plasmonic nanoparticles, Link and co-workers investigated the size dependence of PL thought to result from the plasmon-enhanced radiative recombination of hot carriers through inter- and intraband transitions.[59] These researchers utilized Au nanorods (AuNR) of different sizes but similar aspect ratios. From the PL spectroscopy, the importance of the AuNR geometry on the emission and quantum yield was obvious. The interband transitions dominated emission on large AuNRs, which was weakly dependent on size, while intraband contributions decreased with size causing the long wavelength of emission. These findings should facilitate more rational design and optimization of plasmonic systems that rely on hot carrier generation.

The field of plasmonics has many fundamental questions that remain unanswered; despite these unknown aspects, the plethora of measurement techniques based on plasmonic effects that are in development or have already been developed are providing crucial new information that should aid in further elucidating answers to the remaining questions. The use of plasmonic phenomena has enabled the analysis of systems and processes that were previously inaccessible, which not only adds to the understanding of plasmonics but also to the understanding of the system analyzed. As the field of plasmonics evolves, it will continue to be an extensively relied upon tool for analysis of surfaces and interfaces.

■ SURFACE IMAGING METHODS BASED ON OPTICAL SPECTROSCOPIES

Recent advances in imaging have allowed scientists to push the boundaries of what is possible in terms of imaging subject and spatial resolution. Particularly, biological imaging and tip-enhanced techniques in general have each been advanced significantly within the past few years. Herein, we highlight

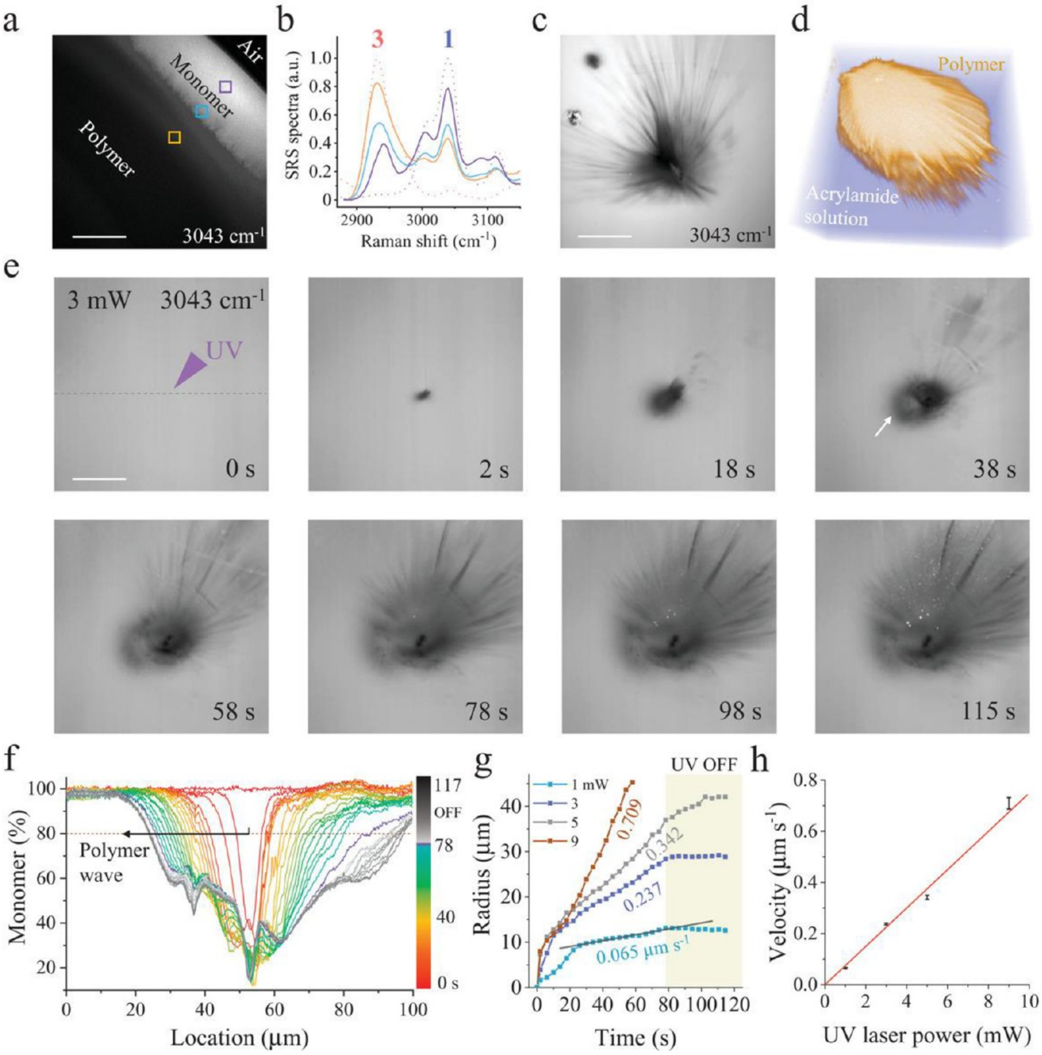

Figure 3. (a) SRS imaging of acrylamide/air interface after 3 min of uniform UV exposure. Scale bar, 50 μm. (b) SRS spectra on the indicated locations in panel a. The blue and orange dotted lines represent the SRS spectra of pure monomer (**1**) and polymer (**3**) for reference. (c) Spectral SRS imaging of polymer formed by a focused UV laser. Scale bar, 30 μm. (d) Two-species 3D SRS imaging of both monomer and the formed polymer structure. (e) SRS recording of fast polymerization dynamics every 4 s. Arrow indicates the polymer wave. Scale bar, 25 μm. (f) Intensity profiles of monomer distribution across the initiation center (indicated by the dashed line in panel e). Purple curve indicates the boundary of the UV laser on and off. (g) Radius of propagating polymer waves with times at different UV laser powers. (h) Linear dependence of propagation speeds of polymer waves with the UV laser power. Used with permission from Li, H.; Cheng, Y.; Tang, H.; Bi, Y.; Chen, Y.; Yang, G.; Guo, S.; Tian, S.; Liao, J.; Lv, X.; Zeng, S.; Zhu, M.; Xu, C.; Cheng, J.-X.; Wang, P. *Advanced Science* **2020**, 7, 1903644, DOI: 10.1002/advs201903644 (ref 60). Copyright 2020 the Authors. Published by WILEY-VCH Verlag GmbH & Co. KGaA, Weinheim.

research done in these aforementioned fields while also including other emerging imaging techniques to showcase the many recent innovations. From instrumental setups to updates of more conventional techniques, optical and vibrational imaging methods are delivering higher spatial resolution and more chemical information than ever before.

Imaging in Solution Including Biological Systems. Monitoring solution-phase reactions with high temporal and spatial resolution has been challenging. This is especially true for polymerization reactions. Li et al. utilized SRS microscopy based on collinear multiple beams to image the ultrafast kinetics of radical polymerization reactions in a label-free approach at a video rate sampling frequency of 2 kHz with submicron spatial resolution and understand the evolution of polymeric chain development.[60] Imaging the test case reaction of acrylamide cross-linked with *N*,*N*′-methylenebis-(acrylamide) was demonstrated as shown in Figure 3. This reaction showed three distinct phases: chemical initiation, radical propagation, and termination to yield a hydrogel. These researchers observed for the first time what they termed a polymer "wave" stemming from UV initiation that was driven by radicals generated at the initiation center. Monitoring the loss of the monomer stimulated Raman signal showed that this wave did not form immediately but was delayed by ∼100 ms from the onset of illumination; moreover, this wave did not expand at a constant rate but instead reached a maximum propagation rate of 35 M s^{-1} 236 ms after illumination started. This maximum propagation rate mediated the reaction progress, with the wave propagating outward toward regions of higher monomer concentration. The polymer propagation velocity was determined to be as high as ∼13 μm s^{-1} with a dependence on laser power. The ability to image with high temporal and spatial resolution offers immense possibilities for imaging chemical processes and understanding the distribution of reaction products with time.

Imaging surfaces and interfaces in aqueous media such as biochemical systems is inherently difficult due to the complexity of biological milieu. Several advances since the last review have been published that begin to address these intrinsic limitations. Although often motivated by the desire to understand biological systems such as cells and tissues, the significance of these advances should be viewed in the broader context of other surface and interfacial systems in aqueous environments important in areas such as electrochemistry and catalysis.

Understanding and determining the chirality of biological molecules is critical for the advancement of biomedical science. Recently, Bhargava and colleagues[61] improved on the traditional FTIR based approach for vibrational circular dichroism (VCD) analysis by implementing a custom quantum cascade laser (QCL) equipped with a discrete frequency infrared microscope for VCD imaging. Taking advantage of the intrinsic linearly polarized nature and high output power of the QCL source permits rapid VCD imaging of complex biological samples. Moreover, the custom QCL-VCD microscope developed in this work allowed simultaneous acquisition of IR and VCD images using a digitally tunable photoelastic modulator to control beam polarization. VCD imaging of a colon tissue sample was successfully undertaken, the first such instance of VCD data recorded using an IR imaging configuration. These images allowed elucidation of protein conformational features of the tissue without the use of stains or dyes. Tracking the VCD image at the 1632 cm^{-1} amide band resulted in a positive VCD signal for an α-helix secondary structure but a negative signal for a β-sheet structure. Although applied to the investigation of tissue in this initial report, this QCL-VCD microscopy approach should be amenable for VCD analysis of interfacial and surface layers and thin films. We will look forward to such advances in future reports on this new methodology.

Lea and co-workers recently used correlated AFM and IR s-SNOM to image a two-dimensional membrane-mimetic peptoid sheet and a three-dimensional catalase nanocrystal with a lateral spatial resolution of ~20 nm.[62] Their imaging data demonstrating heterogeneous vibrational line widths and amplitude distributions allowed them to distinguish areas of peptoid monolayers or multilayers in the 2D peptoid layer and assess secondary structure of the three-dimensional catalase nanocrystal.

These researchers later expanded this approach to be better compatible with *in situ* and *in vivo* environments by coupling a conventional s-SNOM setup with a total internal reflection (TIR) geometry that spatially confines the excitation to minimize spectral interference from absorbance by water.[63] They demonstrated the capabilities of this approach by successfully imaging the same monolayer peptoid nanosheet on a gold nanostructure and catalase nanocrystal as used for the above-noted study. Beyond the possible biochemical applications of this method, this work represents a significant advance for *in situ* IR nanospectroscopy in aqueous media more broadly with potential relevance for biological, catalytic, and electrochemical systems.

An advance in point-by-point discrete frequency IR (DFIR) microscopy using quantum cascade lasers for imaging systems such as biological samples in aqueous media was reported by Bhargava and co-workers. This advance was developed to address the limitation of the long acquisition times of point-by-point scanning relative to conventional widefield IR imaging approaches.[64] Their system consists of an array of QCL modules with a combined tuning range that covers the mid-IR fingerprint region. Half of the beam is focused on the sample while the other half is sent to a beam block. The transflected signal is demodulated with a lock-in amplifier tuned to the pulse repetition frequency of the QCL and is detected by a cryogenic photovoltaic mercury cadmium telluride detector. The microscope portion under the microscopy stage is just a standard white-light epi-illuminated inverted microscope. For situations where a full spectrum is needed, a QCL-based rapid scanning point spectrometer was incorporated. Their DFIR system had noise levels about an order of magnitude lower than that of a conventional FTIR microscopy system, and they determined that for large samples where only a discrete spectrum is needed, their system outperformed a state-of-the-art FTIR imaging system. By using refractive lenses, they improved the contrast and spatial resolution when compared to the FTIR setup. Finally, they were able to speed up data acquisition even more by simultaneously imaging two tunable frequencies using demodulation. These advancements are promising for practical imaging of large samples for diagnostic applications.

In another methodological advance, Wang and co-workers developed ultraviolet-localized mid-infrared (MIR) photoacoustic microscopy (ULM-PAM) also for high resolution, low background MIR imaging of surfaces in aqueous environments including biological samples.[65] This method overcomes limitations from the strong MIR absorption of water while providing lateral resolution on the order of 250 nm. In this approach, the sample is thermally excited by a pulsed mid-IR laser while a second pulsed confocal UV laser detects photoacoustically the brief rise in sample temperature. This approach reports the MIR absorption magnitude of the sample and takes advantage of the enhancement of photoacoustic signals upon an increase in temperature, also known as the Grüneisen relaxation effect. The images resulting from this method thus show MIR absorption contrast but have lateral resolution determined by the UV wavelength. Additionally, since the UV light is transmitted in water, the strong water MIR absorption background is suppressed. The capabilities of ULM-PAM were demonstrated by chemically mapping intracellular distributions of lipids and proteins in 3T3 mouse fibroblast cells. Although beyond the scope of this review, the large penetration depth of this technique also lends itself to imaging thick samples as well as thin samples. This versatile technique has tremendous potential for imaging surfaces and thin films, including fresh biological thin film samples, in aqueous environments. These researchers suggested that this approach could be extended to far-field nanoscale chemical imaging by replacing the UV probe beam with an X-ray beam to do X-ray acoustic imaging with nanometer-scale lateral resolution.

Higher order-coherent antistokes Raman scattering (HO-CARS) microscopy was developed by Huang and colleagues as another approach for imaging thin film biological samples.[66] In HO-CARS, higher-order nonlinear optical processes dominate and can be detected at new wavelengths for high-contrast vibrational imaging with concomitant breaking of the diffraction limit. HO-CARS signals arise from two contributions: higher-order nonlinear direct processes ($\chi^{(5)}$, $\chi^{(7)}$) and the lower-order cascaded $\chi^{(3)}$ process. Using a high numerical

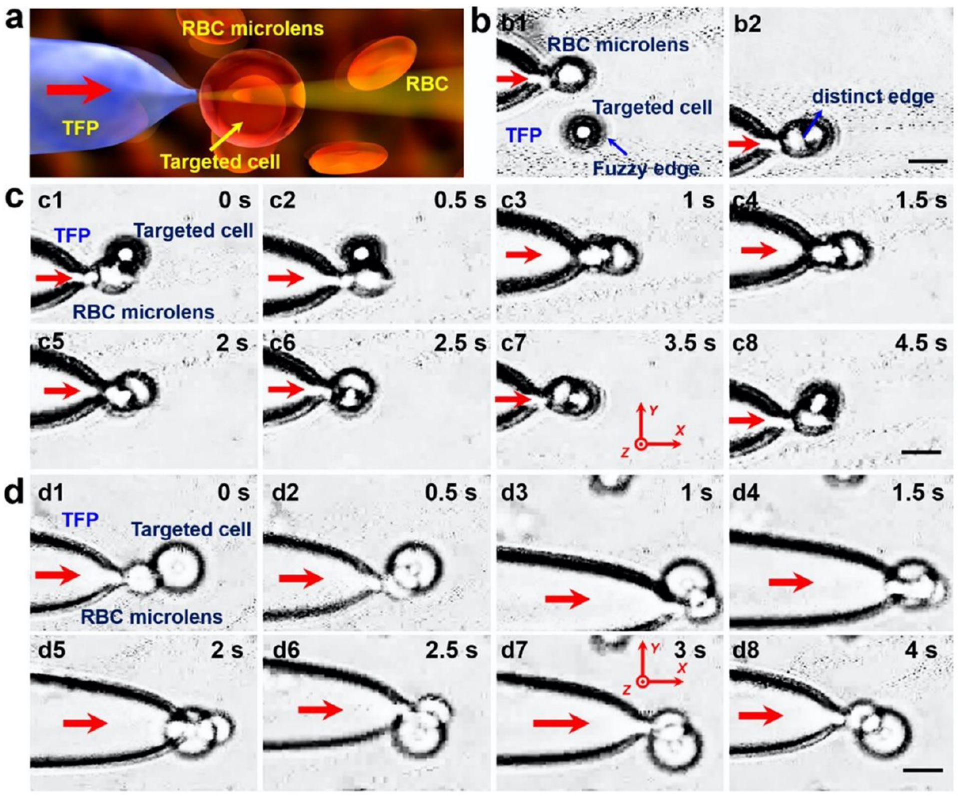

Figure 4. (a) Schematic for the RBC microlens for membrane imaging. (b) Optical microscopic images comparing membrane images without (b1) and with an RBC microlens (b2). (c,d) Scanning imaging using one RBC microlens with the spherical shape (c1−c8) and the normal shape (d1−d8). Scale bar: 10 μm. Reprinted with permission from Liu, X.; Li, Y.; Xu, X.; Zhang, Y.; Li, B. *ACS Appl. Bio Mater.* **2019**, *2*, 2889−2895 (ref 68). Copyright 2019 American Chemical Society.

aperture objective to achieve a tighter focus than in conventional CARS microscopy, the higher order contributions ($\chi^{(5)}$, $\chi^{(7)}$) become dominant and provide richer spectral information than the cascaded $\chi^{(3)}$ process. Moreover, the higher order six- and eight-wave mixing processes lead to much smaller excitation volumes, resulting in significantly improved spatial resolution by a factor of almost 2. These researchers demonstrated this approach by imaging the 2216 cm^{-1} ν(C≡C) mode of 1,4-diphenylbuta-1,3-diyne crystals, the 2930 cm^{-1} $\nu(CH_3)$ mode of pure dimethyl sulfoxide (DMSO), and the 2845 cm^{-1} $\nu(CH_2)$ alkyl mode of species in HeLa cells. The advantages of HO-CARS over basic CARS are clear. Easy integration of HO-CARS systems into current CARS microscopes should allow widespread and broader adoption of this imaging tool for surfaces, interfaces and thin films.

The use of combined AFM-IR methods to image the cell surfaces and to map cellular composition has continued to expand. Ruggeri and co-workers utilized AFM-IR to identify oxidative stress in red blood cells (RBCs).[67] By monitoring $\nu_s(CH_2)$ and $\nu_a(CH_2)$ bands, they identified oxidative stress earlier than the observation of morphological changes in the cells and correlated oxidative stress levels with structural changes in the cells. Through this approach, they were able to identify the cell regions most susceptible to oxidation, and in cells with serrated edges, the presence of membrane peroxidation through the appearance of a ν(C═O) band. Although previous work had demonstrated that morphological changes were the main observable consequence of cell aging and oxidative stress, the AFM-IR results showed that detectable chemical changes occur before these morphological changes become apparent, thus opening the possibility of diagnostic tools based on this approach.

Although desirable, it is difficult to construct small and biocompatible systems capable of imaging biological surfaces. Zhang and Li and co-workers reported an approach that cleverly addresses this challenge using RBCs as biomicrolenses.[68] As shown in Figure 4, with the help of a tapered fiber probe (TFB) and a 980 nm laser beam launched into the TFB, a RBC can be optically trapped and aligned at the fiber tip to form a microlens and then moved laterally to perform scanning imaging with magnifications on the order of 1.1−2. This RBC microlens was then used to image a single cell target single-cell membrane. The ability to stretch the RBC membrane to alter focusing was demonstrated as well. This technique was extended by trapping multiple RBCs in a linear array and creating a wide-field system that produces images more quickly.

In a similar approach utilizing the optical trapping of cells, Qiu and Li and colleagues developed a "bionanospear" nanoprobe with subwavelength spatial resolution.[69] This probe consisted of a tapered fiber handle and a head consisting of a yeast cell coupled to a linear array of *L. acidophilus* cells. Launching an 808 nm laser beam into the taber fiber, an optical trap is created that captures a yeast cell. Using this cell as the lens, the beam is then focused to trap a *L. acidophilus* cell along its long axis. The process is repeated for trapping additional *L. acidophilus* cells to complete the bionanospear; light that propagates along the spear linear array can be focused to a spot of ~190 nm diameter for imaging individual cells. To demonstrate its use in practical applications, this bionanospear was used to probe leukemia cells stained with green fluorescent protein. The fluorescence images of the cell show that this bionanospear system can selectively scan and excite subwavelength, high-resolution spots on the cell. As a further demonstration of the versatility and utility of this device, the bionanospear was forced against the cell membrane without membrane puncture. Such biomicrolens systems have the potential to significantly advance biological imaging with subwavelength lateral resolution; their use in other types of surface and interface imaging in aqueous media should be explored.

Advances in Tip-Based Vibrational Spectroscopy Imaging. Vibrational spectroscopic imaging using tip-based approaches continues to receive strong interest in the community. A number of fundamental advances have been reported in this period that represent significant improvements in tip-based imaging capabilities.

Tip quality and reproducibility have long been known to be major drawbacks to TERS. In particular, the tip-broadening effect wherein imaged object dimensions are larger than their true size is a problem from which all AFM-based techniques suffer. Wang and Kurouski studied the tip broadening effect in TERS imaging using triangular Au nanoplates 40−100 nm in height and tens of microns in length possessing top surfaces of Au (111) and sides of Au (100) or (110) crystal facets.[70] Using these nanoplates as tips, these researchers found, surprisingly, that the tip broadening was similar in TERS and AFM images when there were active TERS hotspots along the shaft of the nanoplate from the presence of metallic nanoparticles; however, when the only TERS hotspot was highly localized at the tip of the probe, the broadening in TERS imaging was less than observed in AFM imaging.[70] While these results serve as a cautionary tale for researchers attempting TERS imaging, they also offer the interesting possibility that hot spots along the shaft might be harnessed for three-dimensional chemical mapping.

In another exciting TERS development, Kusch and co-workers reported excitation-tunable TERS (e-TERS).[71] In e-TERS, a continuously tunable laser is used that enables resonant Raman scattering hyperspectral imaging with nano-scale spatial resolution. To demonstrate this capability, they imaged an ensemble of carbon nanotubes on a gold surface with four excitation wavelengths from which they were able to identify nine different carbon nanotube species and determine their distributions and orientations. These results indicate that e-TERS is a new nanoimaging tool that can be used to obtain excitation-dependent hyperspectral images.

Although the use of TERS has become more widespread in recent years, there still remains relatively little work reported using TERS in liquid phase environments. El-Khoury and co-workers demonstrated fast nanoscale chemical TERS mapping of Au nanoplates in aqueous solution to build upon the understanding of TERS measurements at the liquid−solid interface.[72] Using TERS in a bottom excitation illumination configuration, Raman spectra of the 2225 $\mathrm{cm^{-1}}$ $\nu(\mathrm{C{\equiv}N})$ band of p-MBN-functionalized triangular Au platelets were successfully imaged along the nanoplate edges with 50, 10, and 2 nm lateral step sizes at 0.25 s per pixel in water with sub-15 nm spatial resolution. These results are significant because these researchers demonstrated a robust approach for TERS mapping of local optical fields in aqueous environments. This work enables TERS chemical and biological imaging and monitoring of chemical transformations at solid−liquid interfaces.

In a follow-on application of this work, these researchers used their TERS imaging setup to monitor the model plasmon-driven dimerization of *p*-nitrothiophenol (p-NTP) to dimercaptoazobenze (DMAB) on triangular Au platelets in aqueous solution.[73] By simultaneously monitoring vibrational frequencies independently corresponding to p-NTP and DMAB, they observed DMAB formation only at select sites along the edges of the Au nanoplatelets. Significantly, they demonstrated that this plasmon-driven chemistry did not occur at all places along the nanoplatelet edges that exhibit optimally enhanced electric fields. These effects had not been noted in previous experiments that suffered from poorer spatial resolution. In light of the uniformity of the Au nanoplates used for TERS in this work, these workers concluded that a reversible p-NTP-to-DMAB process that generated both trans and cis isomers at the interface as well as molecular crowding and steric effects must influence this plasmon-assisted chemical transformation.

Detailed imaging of charge movement during individual bond vibrations remains difficult because it requires Angtrom-level spatial resolution. Probe-based techniques such as TERS provide resolution below the diffraction limit, but the size of the probe and the tip−sample distance must be on the atomic scale to attain atomic resolution. Apkarian and co-workers met these requirements by measuring the electronic Raman scattering of flat Co(II)-tetraphenyl porphyrin (CoTPP) molecules immobilized on a Cu(100) surface using the precisely controlled junction between the tip and the sample of a scanning tunneling microscope in ultrahigh vacuum at 6 K.[74] With their setup, they achieve Angstrom-scale resolution at subatomic tip−sample distances in the plasmonic quantum tunneling regime. Chemical visualization of the electronic Raman scattering continuum with <2 Å lateral resolution matches the molecular frames of individual molecules. This continuum maps the field confined by the *z*-component of the molecular polarizability and can only be properly imaged with the tip at vertical distances less than ∼2−3 Å from the molecule. The vibrational TERS signal in this approach is confined vertically and laterally on the Angstrom scale, providing stunning images of individual molecule vibrations. This approach of exciting vibrations with atomic scale resolution, a process these researchers refer to as “plucking”, allowed these researchers to explore in detail the intramolecular charges and currents driven by individual vibrational modes and explore their coupling throughout the molecule as further supported with simulations. This boundary-pushing work illustrates the capabilities of tip-enhanced optical microscopy to shed light on the surface and interfacial phenomena at the single vibration level.

The effect of tip bias in TERS on observed Raman spectra was investigated by Meixner and co-workers who studied benzotriazole (BTA) and 2-mercaptobenzothiazole (MBT) SAMs on a Au substrate under a positive bias voltage on the tip.[75] For MBT, the intensity of the 1590 $\mathrm{cm^{-1}}$ aromatic ring band increases with voltages up to 500 mV; with voltages >700 mV, an additional band due to in-plane ring stretching is observed at 1545 $\mathrm{cm^{-1}}$ which becomes dominant at ∼1000 mV. In contrast, the $\nu(\mathrm{NCS})$ of the thiazole ring decreases in intensity with increasing bias and is most intense at low bias potentials. These changes in intensity were attributed to changes in polarizability of MBT and not structural changes, because no frequency shifts were observed as the bias was changed. In similar experiments with BTA, the intensity of the ring mode at 1585 cm^{-1} reversibly decreases with increasing positive bias. Clearly, an electric field at the tip changes the molecular electron density to an extent that depends on the inductive effects of the functional groups on the molecule. These results have important implications for organic molecule-based electronic devices, as it will be necessary to account for changes in the electron density in predicting device operation. This work provides a crucial starting point for better understanding these effects.

Applying TERS to a catalyst system, Zhong and Ren and co-workers studied the local generation and diffusion of active oxygen species (AOS) from H_2O_2 on bimetallic Pd/Au surfaces as they oxidize molecules in of a monolayer of 4′-(pyridine-4-yl-biphenyl-4-yl)methanethiol.[76] AOS from H_2O_2 include species such as $^{\bullet}OH$, $^{\bullet}OOH$, O_2^-, O^-, O (oxene), and OH^-, all of which can induce oxidation of organic molecules with high efficiency. Molecules that are oxidized by these oxidants are much less strongly bound to the surface, leading to a significant decrease in TERS intensity, which thereby reports on localized regions that have undergone reaction. This allows imaging of the active sites for AOS generation on these bimetallic surfaces as well as providing an understanding of how far these AOS can diffuse across the surface while still remaining active. This work clearly documented that the active site for AOS generation on Pd/Au surfaces are primarily located on step edges. Moreover, it was found that AOS have a characteristic diffusion length of ∼5.4 nm while remaining oxidatively active. This study exemplifies the power of TERS for monitoring reactive species on surfaces. Expanded use of the approaches demonstrated in this work is likely in the coming years.

Pushing the limits on what is possible with TERS, He and co-workers used the technique to image and sequence single-strand DNA (ssDNA) with single base resolution.[77] Using a step size of 0.5 nm, they identified characteristic Raman frequencies for each nucleobase and were able to sequence ssDNA strands of the known phage ssDNA (M13mp18) that were 1 nm apart with accuracies greater than 90%. While these are very preliminary results, they open the door for high-resolution imaging of nanostructures or even the development of next-generation sequencing methods.

Drawbacks to the use of SNOM approaches for broadband illumination and collection of nanoscale Raman scattering are the need for unwieldy and complex optical setups and mediocre performance of tapered optical fiber probes. Recently, Liu and Yan and co-workers developed a new, two-step probe for nanofocusing in the near-field and used it for TERS with <1 nm spatial resolution.[78] Their two-stage optical probe utilizes a sharp-tip Ag nanowire in contact along the sidewall of a partially Au-coated (for scanning tunneling microscopy (STM) electrical contact) tapered optical fiber allowing in a scanning tunneling microscope. Linearly polarized incident light is launched into the optical fiber, and when the phase matching (resonance) condition of the linearly polarized LP_{01} mode in the tapered optical fiber with the TM_0 radially polarized surface plasmon polariton mode of the Ag nanowire is met, the radiant energy is efficiently coupled into the Ag nanowire. Further compression of this TM_0 mode, carrying the majority of the incident energy, to a localized surface plasmon "hotspot" at the tip of the nanowire is then performed with an efficiency of up to 70%. This two-step nanofocusing arrangement provides ∼50% efficiency in the overall assembly. Using this probe assembly, these researchers developed a fiber-in-fiber-out lens-free SNOM STM-TERS system with 1 nm imaging resolution. They demonstrated the resolution of this system by imaging single-walled carbon nanotubes (SWCNTs) on a Au surface. This probe allowed acquisition of STM topography maps of the SWCNTs as well as characteristic TERS line scans, representing a significant advance for TERS chemical mapping experiments.

While the combination of nano-FTIR and s-SNOM has allowed unparalleled capabilities in the molecular characterization of unknown samples, it is limited by both the spectral range of available QCL sources and, more practically, the slow acquisition speed of current imaging approaches. To solve the issue of long acquisition times, Schnell and co-workers[79] integrated synthetic optical holography with s-SNOM and nano-FTIR to develop the technique of nano-FTIR holography. The spectral bandwidth of nano-FTIR sources is on the order of a few 100s of cm^{-1}, which enables the practice of interferogram bandpass sampling, or subsampling, and faster data acquisition with no loss in information within the range of frequencies determined by the nano-FTIR source. This approach allows a reduction in interferogram points from 230 to 17 without the loss of any chemical, phase, or amplitude information, leading to an imaging time reduction by a factor of 13. To leverage this improvement in acquisition time, these workers applied interferogram bandpass sampling to synthetic holograms. Unlike conventional nano-FTIR, the synthetic hologram approach works by holding the reference mirror in a constant position while the AFM tip is scanned across the surface; the reference mirror is only moved when the acquisition of a line scan is complete. This allows encoding of the near-field nano-FTIR interferograms throughout the sampling area. The synthetic-near field holograms are obtained by recording the demodulated signal at each pixel, and the near-field amplitude and phase images are easily reconstructed through spatial filtering in the Fourier transform hologram. To test their method, a 100 nm-thick polyvinylidene fluoride and hexafluoropropylene copolymer (FP) film on a Si substrate that contained 100−400 nm FP particle aggregates. These aggregates possessed a slightly higher frequency absorption than the FP film due to different microstructures (1120 cm^{-1} for the film vs 1160 cm^{-1} for the aggregates). Across a 3 μm × 3 μm sample size, the film and aggregates were easily identifiable in ∼20 min from their distinct absorption bands. This work represents the fastest spectroscopic nanoimaging performance utilizing a broadband source ever reported and, thus, is a powerful new technique for routine imaging of different types of samples. These researchers additionally note that the practice of bandpass sampling could be implemented in other scanning methods as well to reduce acquisition time and increase sample throughput.

Although tip-based spectroscopic techniques such as PTIR and resonant enhanced IR nanospectroscopy require at least some contact between the tip and the surface of interest, PiFM does not require contact to measure the photoinduced force. However, despite the fact that PiFM has been successfully implemented as an imaging technique in numerous studies, the origin of the photoinduced force is still not fully understood. Xu et al. investigated the origin of this force with a new approach based on synchronized IR pulse excitation and mechanical detection with a stationary AFM cantilever in the peak force tapping mode.[80] Although similar to PiFM, their system does not use a force heterodyne detection mechanism or oscillate the cantilever. Instead, with a stationary AFM tip, the sample, which is supported on a sinusoidally oscillating piezoelectric stage, periodically approaches and retracts from the tip. Thus, these researchers created a new peak force tapping method and named the technique peak force-photoinduced force microscopy (PF-PiFM). Synchronized pulsed excitation from a mid-IR quantum cascade laser creates a photoinduced force that causes cantilever deflection as measured using a quadrant photodiode, allowing measurement of the photoinduced force. The cantilever response was found to depend on three factors: the IR frequency, the laser pulse timing, and the IR laser power. Further, they note that the photoinduced force is attractive and nonmonotonic and on the order of magnitude of nano-Newtons. This level of force is greater than predicted by the gradient force model but was found to be adequately accounted for through the additional contribution of photothermal expansion (hence, absorption cross-section of the sample) as an additional contributing factor to the force profile that results from the distance-dependent van der Waal interactions between the tip and the sample. This new measurement principle based on detection of photothermal expansion in the noncontact mode should enable IR nanospectroscopy with high lateral resolution.

To diminish measurement artifacts and improve the sensitivity of AFM-IR, Bhargava and co-workers reported a closed-loop (CL) piezo controller that allows responsivity-corrected AFM-IR imaging (CL-AFM-IR).[81] Instead of recording cantilever deflection in response to IR absorbance, the basis of this CL approach is to use a piezoelectric sample platform that is positioned to maintain a null cantilever deflection in real-time in response to the photothermal effect of the sample. The authors demonstrate that the demodulated cantilever deflection signal of a traditional open loop system has higher noise than their new CL-AFM-IR approach. This instrument was used to map thin PMMA films down to 10 nm thick with a ~5× improvement in noise. The ability to readily integrate this approach into existing AFM-IR instrumentation should expand the utility of AFM-IR in the chemical mapping of surfaces and interfaces.

Other Methods. Rubano and Papro and co-workers reported a terahertz (THz) optical four-wave mixing experiment that provides a stimulated hyper-Raman-like response for determining very low frequency modes (Brillouin zone Γ-point phonons, polaritons, and phonons out of the Γ-point) of materials.[82] These researchers call this technique THz stimulated hyper-Raman (THYR) spectroscopy Briefly, in this technique an intense THz pulse is sent to a sample along with 800 nm IR pulses with a time delay. This allows the THz pulse to excite the low energy modes of the material and mix with the 800 nm beam (ω_L) to obtain a stimulated hyper-Raman signal. When the frequency of the THz wave at ω_T is resonant with a low energy mode of the sample, the THYR signal is enhanced and generates Stokes and anti-Stokes frequencies relative to $2\omega_L$, the second harmonic of the fundamental laser frequency. The intensity of modes generated was shown to be dependent on the delay time between the IR and THz pulses and polarization of the 800 nm radiation. The researchers were able to apply their technique on α-quartz and detect modes far from the Brillouin zone Γ point, demonstrating its potential for studying a range of low-energy excitations. Future advances expected include coupling THYR with scanning probe techniques to improve the spatial resolution of THz techniques to the subnanometer scale.

In another THz-based advance, Aghamiri et al. have combined s-SNOM with THz time domain spectroscopy (TDS) in a technique termed THz time domain nanospectroscopy (THz-TDNS) to achieve hyperspectral THz nanoimaging in the 0.5−1.8 THz frequency range with a spatial resolution of ~170 nm.[83] This approach overcomes the intrinsic limitation of conventional THz spectroscopy that, because of the long wavelength of THz radiation, is diffraction limited to ~150 μm. Moreover, by greatly improving signal levels through forward detection of the tip-scattered field and placing the apparatus in a controlled nitrogen environment, this work demonstrates true hyperspectral imaging, thereby advancing earlier THz-TDNS efforts that were limited to either single point spectroscopy or monochromatic imaging. To demonstrate the capabilities of their system, these researchers measured noninvasively the local mobile charge carrier density of Si without the need for Ohmic contacts. This capability is anticipated to enhance the utility of THz-TDNS in characterizing semiconductors and low dimensional (1D and 2D) materials.

THz tip-based spectroscopy has emerged as a powerful tool for ensemble surface and interface analysis, but it lacks the necessary spatial resolution for imaging nanoscale surface and subsurface features and phenomena. Building on earlier work by Hunsche et al.,[84] Klarskov and co-workers developed a sequential approach for nanoscale reflection-type THz time-domain spectroscopy (THz nanoscopy) and laser THz emission nanoscopy (LTEN).[85] To showcase this combination of techniques, imaging of a structured, lightly p-doped InAs sample was used as a model system. Comparison of the two approaches revealed that LTEN had the greater contrast due to the creation of a strong THz dipole through the photo-Dember after ultrafast photogeneration of charge carriers. This dipole forms as the result of differences in mobilities of holes and electrons in the semiconductor. The surface sensitivity of THz nanoscopy and the subsurface surface sensitivity of LTEN provide complementary information about a sample. Additionally, LTEN has better confinement of the THz field below the tip and strong coupling with the sample. The combination of surface and subsurface sensitive charge carrier detection offers a novel technique for semiconductor analysis.

In an advance that offers a stand-alone optical method to 2D and 3D orientational mapping that rivals electron and X-ray based techniques, Ilchencko and co-workers utilized polarized Raman microscopy as a less expensive approach for mapping crystalline samples.[86] Their approach is based on simultaneous registration of multiple Raman scattering spectral intensities obtained at different polarizations. After first undertaking simulations to understand orientation ambiguity with different numbers of on-axis and off-axis channels for excitation and scattering collection using different polarized excitation, the demonstration of ambiguity-free orientational mapping of several types of polycrystalline samples was reported. In 2D single-acquisition Raman orientation mapping (SAROM), a single excitation laser is split into three beams having different polarizations (0°, 45°, and 90°) and focused onto the surface at different spatial locations. Then, the Raman scattering signal is divided into nine backscattering channels, six that are on-axis and three that are off-axis before being spectral dispersed onto a charge-coupled device (CCD) detector. For 3D mapping, three excitation lasers with slightly different wavelengths and different polarizations are focused to a single spot on the sample surface and the Raman scattered signal is again collected in multiple on-axis and off-axis channels, with the resultant Raman scattering being dispersed at slightly different positions across the CCD detector due to the different excitation wavelengths used. After correction of the signal intensities for wavelength dependent intensity attenuation, Raman intensity scaling and normalization, linear phase, and linear amplitude anisotropy of each optical element, and depth-dependent birefringence of the sample in each channel, the orientation of each crystallite can be determined with confidence. These researchers demonstrated 2D SAROM by generating an orientation map of a polycrystalline Si sample and a pharmaceutical preparation and compared the results to maps generated from the more conventional approach of electron backscattering diffraction. The agreement was excellent agreement in both cases with an average orientation differences on the order of ∼2°. 3D SAROM was demonstrated on a semitransparent polycrystalline sapphire sample, again with excellent results. Although these workers acknowledge some limitations of the SAROM approach, the method represents an accessible purely optical method for orientational mapping that should be applicable to a wide range of Raman-active sample types requiring no preparation. With further development, this novel, nondestructive, and relatively inexpensive technique could become widely adopted for 2D/3D crystallographic mapping.

Building on their earlier proof-of-concept development of s-SNOM for mapping surface complex dielectric constant, Stanciu and co-workers recently demonstrated the utility of this approach for mapping complex optical properties of a range of nanostructured materials: polyelectrolyte multilayered capsules for drug delivery, ultrathin optical coatings with controllable color properties, and plasmonic ceramic NPs.[87] These efforts clearly established the use of s-SNOM for revealing optical cues in the complex permittivity mapping with chemical changes and assessing the optical property homogeneity and quality of thin films on the nanoscale, comparable to the spatial resolution of AFM. Collectively, these results establish s-SNOM as a useful tool for surface mapping of the complex permittivity of materials important in nanoscience, nanomedicine, and photonics.

Oft-noted limitations of s-SNOM are that it does not provide direct topographic information with explicit sample−tip distances, signal demodulation can result in different signal shapes resulting in ambiguous spatial information, and contact-based AFM modalities cannot be simultaneously employed to acquire corelated sample surface information. Wang and colleagues developed peak force s-SNOM (PF-SNOM) to overcome these limitations.[88] Using an s-SNOM setup operating in peak force tapping mode with time-gated detection of near-field signals and a far-field background subtraction algorithm, these workers demonstrated how to accurately fit the far field background even when the tip is far from the sample and measure the near-field response as a function of distance. This approach allows three-dimensional tomographic sectioning of the near-field signal as a function of distance from the surface and correlation with other surface measurements. To demonstrate the utility of this new method, surface phonon polaritons (PhPs) of boron nitride nanotubes (BNNTs) were imaged in both lateral and vertical directions. As distance between the tip and surface decreases, the near-field profiles showed a larger near-field signal and stronger tip−sample interactions at the terminal of the tube, suggesting that PhPs have different near-field interactions at different spatial locations. Also noted across the BNNTs were line width changes due to PhP lifetime differences and PhP resonance frequency shifts that depend on tip−sample distance. Lateral resolution for PF-SNOM is ∼5 nm, far better than the lateral resolution of ∼13 nm estimated for tapping mode s-SNOM, while the vertical resolution for PF-SNOM was estimated to be 0.12 nm. Similar results were observed for PhPs in SiC. This work definitively demonstrates that the near-field behavior of samples is impacted by the tip−sample distance, in contrast to the conventional understanding of s-SNOM behavior. With its ability for simultaneous characterization of mechanical, electrical, and optical properties of samples, PF-SNOM is a powerful imaging tool that can be applied to observe nanoscale behavior in both the lateral and vertical directions.

The use of ultrafast lasers and chirped pulse amplifiers have led to a steady rise in nonlinear optical techniques even though they suffer from much broader bandwidths than the vibrational modes that they are used to study. This necessitates the use of narrowband filtering to reduce the bandwidth but is achieved at the cost of laser power, leading to low efficiencies. To address this issue, Liu and co-workers introduced a simple but elegant schematic to achieve high-resolution wave-mixing spectroscopy without sacrificing the power of the laser.[89] Utilizing a basic SFG setup, they overlap NIR and IR laser beams spatially and temporally on the sample, which results in a focused spot size of ∼60 μm and a bandwidth of 60 nm for the NIR beam. The beam can be spatially chirped by insertion of a prism into the beam path, leading to a dispersion of the central frequency along a ∼ 500 μm focal line and a reduction of bandwidth (and spectral resolution) to just 2.2 nm. Further improvement of the resolution is as simple as expanding the image on the CCD through higher magnification optics and/or utilizing a CCD with more vertical pixels. These workers demonstrated the utility of this approach by spectrally resolving the two major ν(C−H) bands at ∼2875 and 2935 cm^{-1} from SAMs of octadecyltricholorosilane (OTS) on silica substrates. Comparison of the results using the spatially chirped scheme with unchirped signals subjected to bandpass filtering showed comparable spectral profiles, albeit without the advantage of full pulse energy characteristic of the chirped scheme. Additionally, these researchers also demonstrated the ability of their chirped SFG setup to perform spatially resolved spectroscopic analyses without the need for scanning. To do this, they partially covered the OTS SAM with a monolayer of graphene and successfully imaged an abrupt increase in spectral resolution of the ν(C−H) bands imaging across the boundary between graphene-covered regions of the SAM to bare regions of the OTS SAM. The simple change implemented in this work of spatially chirping the NIR beam to successfully improve spectral resolution without losing laser power could be easily adapted to other wave-mixing techniques.

■ CATALYSIS

Catalysis has continued to attract widespread attention with particular emphasis of late directed to resolving debate over the mechanism of plasmonic catalysis. In addition, application of subdiffraction-limited nanoimaging spectroscopies to the study of catalytic reaction mechanisms and catalyst surface chemistry has continued unabated during this time period.

Plasmonic Photocatalysis. An unresolved question of widespread interest in plasmonic catalysis is the mechanistic role of hot electron or hole transfer versus thermal effects in the chemistry observed. The hot charge carrier transfer mechanism of plasmonic photocatalysis involves the nonradiative decay of excited surface plasmons that creates energetic hot charge carriers, electrons, and holes that are transferred to nearby reactive molecules, thereby inducing chemical reactions. Despite enormous effort, many critical aspects of this question remain poorly understood, with ongoing research actively addressing these issues. Although all of the details of this discussion are beyond the scope of this review, a recent review by Jauffred provides additional insight into the issues under active consideration.[90] We focus here on surface optical spectroscopic approaches to better understand plasmonic catalysis.

Yoon and co-workers expanded the scope of chemical reactions that were catalyzed by plasmonic photocatalysis to C−C bond cleavage reactions.[91] Using SERS to monitor reaction progress, these researcher followed the catalyzed decarboxylation of p-MBA to benzenethiol and the β-cleavage of *p*-mercaptobenzyl alcohol to benzenethiol in the nanogap regions between Au NPs and a mirrored Au surface. These reactions were proven to be plasmon-driven through the hot carrier transfer mechanism by comparing spectrally identified product formation using bare Au NPs with that occurring using Au@SiO_2 core−shell nanoparticles for which the hot charge carrier transfer mechanism is not possible. This work fundamentally advances our understanding of plasmonic photocatalysis and may facilitate harnessing the power of this phenomenon to improve plasmon-based photonic or photocatalytic devices.

Adding additional evidence and insight into hot electron transfer claims, Van Duyne and co-workers performed a SERS and electrochemical SERS study of plasmon-driven hot-electron transfer using continuous-wave pump−probe SERS.[92] They investigated plasmon-driven hot-electron transfer between Au NPs and [6,6]-phenyl-C_{61}-butyric acid methyl ester (PCBM). The pentagonal pitch vibrational mode of PCBM at 1458 cm^{-1}, known to be sensitive to the PCBM charge state, was used as a reporter for the electron transfer process with a shift of 6−8 cm^{-1} to lower frequency indicative of hot-electron transfer to the PCBM. Significant thermal changes of the PCBM system were probed through the Stokes and anti-Stokes intensities and indicated that photothermal effects were insignificant in this process.

Tian and co-workers investigated the role of hot electrons and, perhaps more importantly, the role of hot holes in the oxidation of *p*-aminothiophenol (p-ATP) to DMAB on Au@TiO_2 nanostructures.[93] Oxidation of p-ATP to DMAB does not occur on bare Au without O_2 and without surface plasmon induced hot electron transfer or on Au@SiO_2 nanoparticles under any conditions. On bare Au NPs, this process in the presence of O_2 occurs via an indirect mechanism involving excitation of surface plasmon-induced hot electron transfer to reduce water to O_2 which then oxidizes p-ATP; however, this reaction cannot be driven even under illumination on Au@SiO_2 or on Au@SiO_2@TiO_2 due to the suppression of charge transfer by the SiO_2 shell. Interestingly, however, on the Au@TiO_2 nanostructures, the oxidation of p-ATP in the absence and presence of O_2 was found to result in different oxidation products. O_2 is similarly proposed to be produced from the reduction of water by hot electrons with the p-ATP being oxidized by the hot holes. In the absence of O_2, however, surface plasmon-induced hot hole transfer, facilitated by the TiO_2 shell, is proposed to lead to direct hot hole oxidation of p-ATP to (oxadiaziridine, 2,3-bis (4-mercaptophenyl)). Whether or not the exact chemistry of the proposed product formed is correct, their work clearly supports the role of TiO_2 in facilitating hot hole transfer and minimizing recombination of surface plasmon-induced electron−hole pairs, an important advance for plasmonic catalysis.

Confirming the role of O_2 in the mechanism, Xu and co-workers utilized both TERS and SERS to investigate the azo-dimerization mechanism for conversion of p-ATP into DMAB during photoillumination, albeit by a slightly different proposed mechanism.[94] Based on TERS and SERS experiments in high vacuum and pure N_2 and O_2 environments along with density functional theory (DFT) calculations, these researchers proposed that the catalyst first dissociates O_2, with the activated O capturing the hot electron and then extracting a hydrogen atom leading to dimerization of p-ATP. They further demonstrated that metal electronegativity affects the availability of electrons for transfer through additional studies using Au, Cu, Al, and their corresponding oxide substrates.

To investigate the effect of molecular orientation on photocatalyzed reactions, Ren et al. used TERS to analyze the effect of molecular orientation on the coupling efficiency of p-ATP and p-NTP to produce DMAB.[95] The coupling reaction of p-ATP and p-NTP is dependent on both adsorption orientation and laser energy on different substrates. Tilting of both p-ATP and p-NTP on Au(111) allows the coupling reaction to DMAB to readily occur. However, on Ag (111), p-ATP is oriented along the surface normal whereas p-NTP is oriented parallel to the surface, both orientations of which impede the reaction. Despite this, the coupling of p-ATP and p-NTP does occur on NPs of both Au and Ag due to complex adsorption orientations, albeit with different rates. These insights into coupling chemistry highlight the ability of TERS to determine the orientational fine structure needed for optimized chemical coupling to occur. These results have important implications for the future design of photocatalysts for optimizing the reactant orientation and adsorption energetics.

To better understand plasmon-driven reaction mechanisms, using SERS, Habteyes and co-workers investigated the hot-electron transfer versus plasmon-pumped adsorbate excitation.[96] The premise motivating this work is that photochemistry can be induced by either by plasmon-induced hot electron transfer to the unoccupied orbital of the adsorbate and/or by a plasmon-pumped HOMO−LUMO electron transition of the adsorbate by energy transfer. Which route dominates depends on a myriad of different factors such as absorption geometry, surface-molecule energy-level alignment, spectral overlap between the resonance of the NP, and the levels of the adsorbate, and presence of other surface ligands, coadsorbed solvent molecules, or ionic species. These researchers explored systems that document contributions from each of these mechanisms, highlighting that the community has only a nascent understanding of these pathways.

Wang et al. demonstrated the role of plasmon-induced hot electron reductive desorption of 4-nitrobenzenethiol in a TERS configuration on Au(111).[97] They used DFT, finite-difference time domain (FDTD), and finite element method (FEM) calculations to confirm that this process must be hot electron transfer driven and not thermally driven, as thermal desorption was calculated to require temperatures of at least 2100 K at the tip−sample junction.

Despite the increase in convincing studies documenting the role of plasmon-induced hot charge carrier transfer in plasmonic catalysis, the debate about the importance of thermal effects continues. Sivan and co-workers argue that plasmon-induced heating can explain many results on plasmonically catalyzed bond dissociation reactions reported in the literature that, they assert, are incorrectly attributed to hot charge carrier transfer.[98] They provide a careful analysis of four previous works describing bond dissociation reactions using an Arrhenius model to prove that these photocatalyzed bond dissociation reactions are the result of thermal effects from collective plasmonically heated nanoparticle sources and not hot electron transfer reactions. That said, these researchers do assert that plasmon-induced hot charge carrier transfer does indeed account for, at least in part, certain other photocatalyzed reactions reported in the literature such as redox reactions.

In developing a technique to quantify thermal contributions in chemical processes, Nordlander, Halas, and co-workers investigated NH_3 decomposition to N_2 and H_2 in a nanoreactor.[99] Utilizing a mixed Cu−Ru surface alloy with Cu NP antennas and Ru surface reactor sites, they constructed a plasmonic antenna-reactor photocatalyst. They note a 1−2 orders of magnitude increase in turnover frequency for this reaction under plasmonic illumination compared with the process driven by heating the catalyst system to equivalent surface temperatures. An excitation wavelength-dependent activation energy barrier was also observed with plasmonic excitation, clearly suggesting an important role for hot electron transfer in this process. Postulating a mechanism involving stepwise N−H bond cleavage of the adsorbed NH_3 to leave $Ru{-}N_{ads}$ species that then combine to form N_2 gas, they postulate that hot electrons activate the $Ru{-}N_{ads}$ surface bond, leading to enhanced formation of N_2 and its subsequent desorption from the surface as the source of the greatly enhanced turnover frequency for this reaction due to the decrease in activation energy brought about by the decrease in surface coverage of intermediates.

Keller and Frontiera used ultrafast nanoscale surface enhanced Raman thermometry on the picosecond timescale to investigate the role of heating in plasmon-driven photocatalysis.[100] Using a pump−probe scheme, these researchers quantified the degree of energy deposition from photoexcited plasmons into specific vibrational modes of adsorbates through measurement of the Stokes and anti-Stokes intensities to determine effective temperatures for specific vibrational modes. They found that the heating dissipated within 5 ps, resulting in a temperature increase of generally less than ∼100 K even under conditions of high photoexcitation. They interpret these results to provide strong evidence that plasmonic catalysis is largely driven by a plasmon-induced process such as hot charge carrier transfer and is not driven by a thermal process.

Applying SERS to investigate nanoreactors, Koopman and co-workers investigated the role of heat distribution in plasmon catalysis as it pertains to the possibility of scaling plasmonic catalysis.[101] By investigating the conversion of p-NTP into DMAB as a model reaction, it was found that driving the reaction at a fixed light intensity turns the 3D heat transport into 1D heat transport in larger nanoreactors leading to eventual destruction of the catalyst by melting. They report that silicon is a better substrate for plasmonic nanocatalysis than glass, because its better thermal conductivity allows it to withstand higher driving light intensities by better mitigating heat build-up. This work clearly elucidates the critical role of heat transport in plasmonic catalysis, which may facilitate development of more efficient nanoreactors as benchtop experiments transition to larger scales.

In an effort to further disentangle hot electron transfer from thermal effects in plasmonic catalysis at the single nanoparticle level, Szczerbiński et al. created nanoreactors between a TERS tip and a Au substrate and explored the single hot spot behavior of a series of SAMs formed from thiols possessing different electron capture cross sections and thermal desorption temperatures: 1-hexadecanethiol, biphenyl-4-thiol, and 1H,1H,2H,2H-perfluorodecane-1-thiol.[102] The premise underlying these experiments was that the reaction products observed through plasmonic catalysis should be similar to those observed upon macroscopic illumination of these SAMs by energetic particles (e.g., X-ray photons or low energy electrons <50 eV) if hot electron transfer played a dominant role in the catalysis. They compared the resultant TERS spectra to literature SERS spectra from macroscopic SAMs after illumination with X-rays and low energy electrons; the TERS spectra were strongly similar to those from SAMs exposed to high energy particles energy reported in the literature. None of these reactions were deemed to be accessible by thermal effects leading these researchers to conclude that these reactions are the result of hot electron transfer. Understanding the analogy of plasmonic catalysis to the processes that occur with high energy particle exposure should enable more rational design of systems for successful exploitation of plasmonic catalysis.

Vibrational Spectroscopy Advances in Probing Other Catalytic Systems. Ryu et al. synthesized photocatalytic nanoconjugates based on a cubic or spherical AgCl nanocore wrapped by a trimetallic nanomesh of Au, Ag, and Pd or Au, Ag, and Pt by selective reduction of the metal mesh from its ionic components.[103] The combination of the ionic core and the metallic mesh allows the mesh to absorb visible light for plasmonic catalysis and support SERS reaction monitoring while the porosity of the mesh allows the photocatalytic AgCl surface to catalyze reactions. The trimetallic structure exhibits both plasmon-enhanced and metal-based catalysis while also serving as an internal probe for SERS monitoring of reactions. After thorough characterization of these novel catalyst materials, the catalytic reduction of environmentally harmful Cr^{6+} to Cr^{3+} and p-NTP to p-ATP were investigated.

To investigate the activation of oxygen at the interface of a composite nanocatalyst with a ternary blend, the adsorption and activation of CO was investigated. To probe the oxygen activation on a Pt-CeO_2 interface, Li, Zhang, and co-workers utilized a SERS "borrowing strategy" in which the SERS associated proximate Au nanostructures are used to understand the chemistry at nearby surface sites on a nonenhancing substrate.[104] In this work, the researchers constructed a CeO_2 island on a Au@Pt substrate forming Au@Pt-CeO_2 core−shell−satellite nanostructures from which SERS signals could be observed for species on not only the Au part of the composite but also the CeO_2 and Pt parts of the composite. By monitoring the ν(Pt−C) band at 550 cm^{-1} for CO adsorbed on composite Pt, the ν(Ce−O) band at 450 cm^{-1} for CO absorbed at Ce^{3+}, and the ν(Pt−C) band at 490 cm^{-1} for CO adsorbed on the surrounding Pt substrate, the behavior of distinct catalytic sites could be individually monitored. The

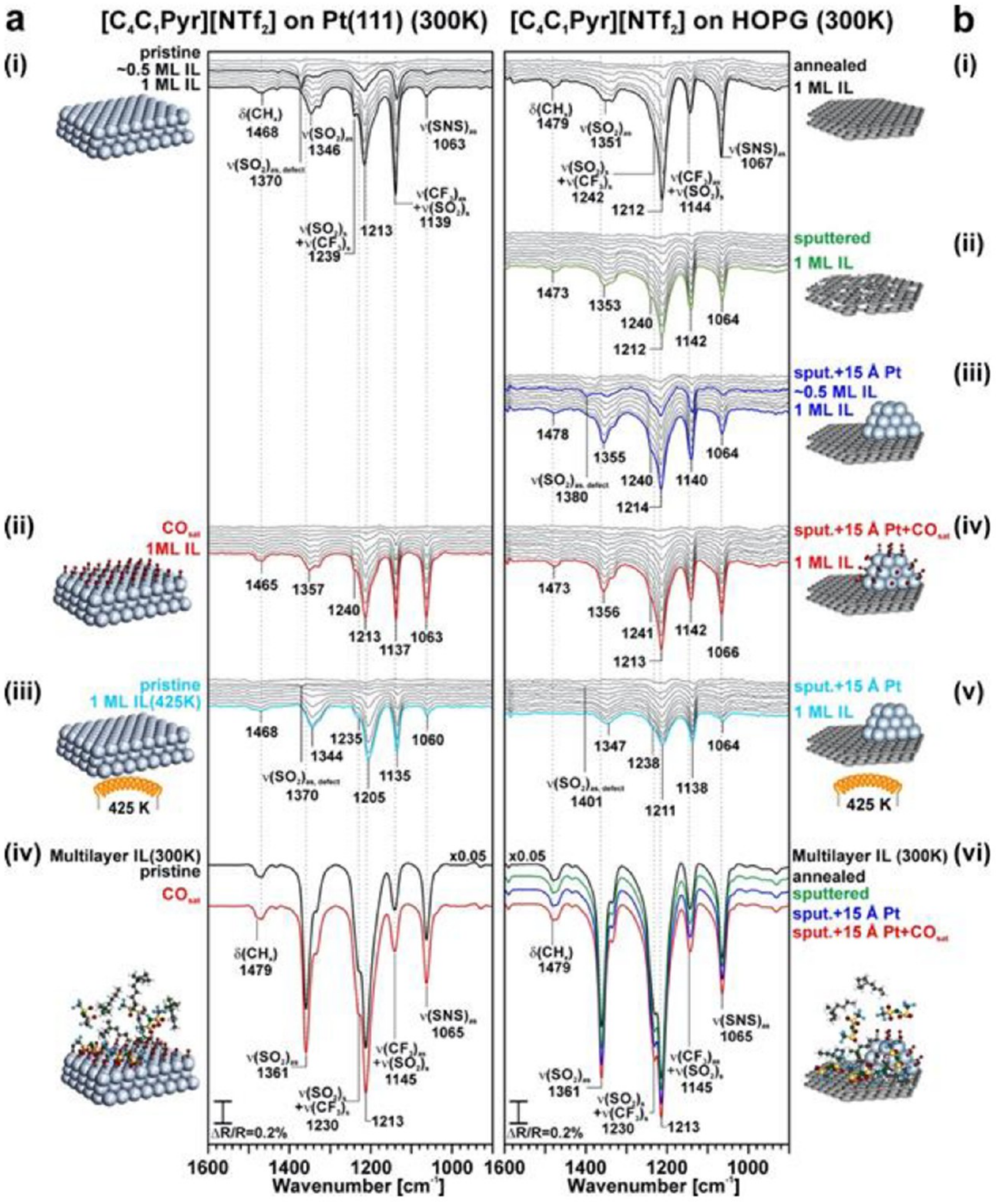

Figure 5. Comparison of IL film growth on different substrates: (a) time-resolved IRRAS recorded during deposition of [C4C1Pyr][NTf2]: (i) onto pristine Pt(111) at 300 K, (ii) onto Pt(111) presaturated with CO at 300 K, (iii) onto Pt(111) at 425 K, and (iv) comparison of IR spectra of IL multilayers on Pt(111) at 300 K. (b) Time-resolved IRRAS recorded during deposition of [C4C1Pyr][NTf2]: (i) onto preannealed HOPG at 300 K, (ii) onto Ar^+-bombarded HOPG at 300 K, (iii) onto Pt NPs on Ar^+-bombarded HOPG at 300 K, (iv) onto CO-saturated Pt NPs on Ar^+-bombarded HOPG at 300 K, (v) onto Pt NPs on Ar^+-bombarded HOPG at 425 K, and (vi) comparison of IR spectra of IL multilayers on HOPG at 300 K. Reprinted with permission from Schuschke, C.; Hohner, C.; Stumm, C.; Kettner, M.; Fromm, L.; Görling, A.; Libuda, J., *J. Phys. Chem. C* **2019**, *123*, 31057−31072 (ref 110). Copyright 2019 American Chemical Society.

CO oxidation pathway was determined from the time and temperature-dependent SERS responses. These studies proved definitively that the O_2 activation to chemisorbed O step of the CO oxidation reaction on both lattice Ce−O and Pt sites of the composite occurred to a greater degree compared with Pt alone. This work enhanced the understanding of O_2 activation of oxide-supported metal structures and demonstrated SERS to be a powerful tool for monitoring such catalytic processes through ready access to the low-frequency region.

Li and co-workers used SHINERS for the *in situ* investigation of the catalytic hydrogenation of p-NTP to p-ATP on Pt-containing mixed-metal catalysts of different size and composition.[105] Pinhole-free shell-isolated SERS-supporting nanoparticles were decorated with Pt, PtCu, and PtNi nanocomposite catalysts, allowing *in situ* SERS monitoring of reactions at the metallic catalyst surfaces. In terms of composition, bimetallic catalysts were found to outperform Pt catalysts, an effect that was attributed to weakening of the N−O bond in $-NO_2$, as supported by a decrease in frequency of the ν(O−N−O) band, on the bimetallic catalysts relative to Pt. Pure Pt catalysts of 5.0, 6.8, and 8.3 nm size were studied, with the catalytic efficiency optimized with the 6.8 nm NPs. This work is an excellent example of the power of SHINERS for the *in situ* study of catalytic systems. This group further provided a nice review of the use of SHINERS for investigation of electrochemical- and heterogeneous-catalysis systems with a consideration of prospects for future improvements.[106]

In more conventional vibrational spectroscopy studies of catalysts, Nuguid et al. investigated the selective catalytic reduction of NO_x and NH_3 on V_2O_5/TiO_2 catalysts by Raman spectroscopy with modulated reactant exposure and simultaneous time-dependent detection of the Raman signals from the catalyst.[107] In this innovative approach, the time domain spectra of the active parts of the catalyst whose structures change by interaction with reactants are extracted from the signals from large concentrations of steady-state catalyst species by transformation to the phase domain. The results indicated that both the V_2O_5 and TiO_2 are necessary for the reaction, but only V_2O_5 catalyzes the reaction. TiO_2 was found to be a reservoir for NH_3 that can then be shuttled to the active V_2O_5. However, not all V_2O_5 is active, with only the portion of the V_2O_5 sites that are unsaturated being active.

Comparing binary and ternary catalysts, Carrero and co-workers correlated the structure−reactivity relationship of supported metal oxide $V/Nb/SiO_2$ catalysts by time-dependent *operando* Raman spectroscopy.[108] Correlation of the reaction rate with the oxidation state of the active site was achieved through monitoring the Raman signature of the vanadyl $\nu(V{=}O)$ band at ~1032 cm^{-1} from isolated VO_4 surface species in catalysts of differing vanadia and niobia contents. Using sequential pulsed dosing of O_2, these researchers summatively approached exposure to a predetermined amount of reactant per amount of catalyst to time resolve the fast oxidation of the catalysts surface species. In comparing the binary with the ternary system, it was found that the Nb hindered V reduction while V promotes Nb reduction, but the exact nature of this process needs to be further investigated. The synergistic effect observed in the ternary system highlights the utility of this approach for analyzing such complex systems under *operando* conditions.

Howe and co-workers studied the elementary steps in the formation of hydrocarbons from methanol catalyzed by HZSM-5 using synchrotron IR nanospectroscopy (SINS) with a temporal resolution of 250 ms.[109] SINS allows investigation of large single crystals of the HZSM-5 catalyst with very high temporal resolution because of the high intensity of the synchrotron source. In contrast, the majority of previous surface vibrational spectroscopy studies on this system, that were less conducive to effective *operando* investigation, integrated signals over many crystals with much poorer temporal resolution. In this reaction, dimethyl ether was found to form first and then bind to a Brønsted acid site by hydrogen bonding followed by the formation of surface methoxy groups which produce hydrocarbons that desorb from the catalyst surface. The temporal response of the species involved produced some unexpected observations of abrupt changes in intensity after reactant introduction. The high temporal resolution and use of both methanol and deuterated methanol to unravel the mechanism in this system provided an enhanced understanding of these important reactions and highlighted the elegance of SINS for the study of surface catalysis.

In an investigation of catalysis in supported thin layers of ionic liquids at metal surfaces with IR reflection−absorption spectroscopy (IRRAS) in both time-resolved and temperature-programmed implementations, Libuda and co-workers studied catalysis by Pt (111) and Pt NPs supported on highly oriented pyrolytic graphite (HOPG) coated with layers of 1-butyl-1-methylpyrrolidinium bis(trifluoromethylsulfonyl)-imide $[C_4C_1Pyr^+]$-$[NTf_2^-]$ under ultrahigh vacuum conditions.[110] On Pt, this ionic liquid has a strongly held monolayer and a more weakly bound bulk layer as shown in Figure 5. The strong adsorption of the ionic liquid is largely due to the $[NTf_2^-]$ component. Preadsorption of CO prevents $[NTf_2^-]$ adsorption at defect sites, whereas coadsorption results in CO displacement from atop sites by $[NTf_2^-]$ while retaining CO in bridging sites. Finally, CO was found to not penetrate bulk thin films of the ionic liquid, although CO does penetrate monolayers of this ionic liquid to form a mixed adsorbate phase on the surface. These results have important implications for the rational design of solid catalysts with supported ionic liquid layers.

Guo and co-workers used an *operando* double beam FTIR spectroscopy design to eliminate spectral interference from gas-phase species in understanding the effect of Zn on HZSM-5 in the aromatization of isobutane to benzene, toluene, and xylene.[111] Their double beam approach is achieved by collecting reference and sample spectra simultaneously, thereby providing an unimpeded view of dynamic surface processes. These researchers compared HZSM-5 and Zn-modified HZSM-5 and found that the modified catalysts exhibit better activity for isobutane aromatization due to its strong adsorption interactions with intermediate olefins such as ethylene, propene, and butene but weaker interactions with product aromatics. The use of this *operando* double beam approach enabled these researchers to elucidate the details of these complex chemical processes without interference from gas phase reactants, intermediates, or products for the first time.

Time-resolved IR spectroscopy on the picosecond to millisecond time scale was used similarly by Orr-Ewing and co-workers to follow the photochemical decarboxylation of cyclohexanecarboxylic acid in deuterated acetonitrile, which is a convenient source of free radicals for chemical synthesis.[112] This IR transient absorption (TA) configuration[113] used two tunable mid-IR probe beams that interrogate the reaction volume excited by a UV pump pulse after a variable time delay, allowing simultaneous monitoring of two spectral frequency regions. Utilizing a co-oxidant pair of phenathracene (PHEN) and 1,4-dicyanobenzene, the selective excitation of PHEN in the reaction mixture provides selective peaks to analyze the decarboxylation time scale. The elementary steps of photooxidation to bimolecular electron transfer and decarboxylation were observed through tracking bands for the photooxidant $PHEN^+$ and subsequent growth of CO_2 to estimate the lifetime of the transient carboxyl radical at 520 ns. The ability to monitor kinetics over 8 orders of magnitude in time with a single technique highlights the value of TA with high repetition-rate spectroscopic probes to resolve multistep photocatalytic reaction mechanisms in catalysis.

Understanding structure−activity relationships in catalysis is critical in optimizing catalytic performance and has gained increased importance as the scale of catalytic control has decreased to nanoscale dimensions. Bañares and Daturi and co-workers coupled fiber optic-based Raman and transmission FTIR spectroscopies along with gas phase analysis for *operando* characterization of catalysts.[114] This approach facilitates complementary characterization of adsorbed species, reaction intermediates, and structural properties of the catalyst as nicely showcased in an investigation of a vanadium-based catalyst during propane oxy-dehydrogenation. Specifically, this study allowed better elucidation of the role of different oxygen species bound to vanadium sites during catalysis. Insights made possible by this combined approach should contribute to better rational design of catalysts.

Researchers at the Fritz Haber Institute utilized their new vibrational spectroscopy tool, surface action spectroscopy (SAS), to elucidate the structure of the topmost atomic layers in magnetite with and without surface water.[115] In this approach, surfaces are first decorated with so-called "messenger" species such as rare gas atoms or H_2. Then, the decorated surface is irradiated with tunable IR radiation from a free electron laser and the desorbed messengers are monitored in real time with a mass spectrometer. The mass spectrometer signal levels of the messengers vary with the amount of IR radiation absorbed by the catalyst surface, thereby mapping the vibrational signatures of the uppermost catalyst layers. In this study, thin Fe_3O_4 (111) and biphasic Fe_2O_3 (0001) films supported on a Pt(111) surface were investigated in the frequency region from 300 to 700 cm^{-1} in the absence and presence of dosed H_2O to understand the structures of H_2O-derived adsorbate layers. This work clearly documents the power of SAS for surface chemical structure elucidation. The fact that SAS can be readily applied to disordered and even rough surfaces portends its continued use as a vibrational spectroscopy tool to investigate catalyst surface chemistry.

■ ELECTROCHEMICAL SYSTEMS AND CORROSION

Fundamental Studies on Electrochemical Systems. In addressing unresolved questions about pyridine adsorption and reaction at electrode surfaces in aqueous electrochemical systems, Tian and co-workers used electrochemical surface-enhanced Raman spectroscopy (EC-SERS) along with isotopic labeling to detect the presence of both pyridine and the α-pyridyl radical at Pt electrodes.[116] Investigation of the potential dependence of the resulting SERS spectra enabled an understanding of how coverage, binding strength, and molecular orientation are tuned by electrode potential. This insight is critical in developing a mechanistic understanding of pyridine-mediated redox processes of interest such as CO_2 reduction.

Gurkan and co-workers used EC-SERS to investigate the interfacial structure of bis(trifluorosulfonyl)imide ($TFSI^-$)-based ionic liquids at the electrode−electrolyte interface with a specific focus on the impact of cation alkyl chain length on interfacial structuring at glassy carbon and Ag electrodes.[117] The $TFSI^-$ forms a dense, strongly adsorbed anion layer at more positive potentials on glassy carbon wherein the longer alkyl chains of the quaternary ammonium cations screen anion−anion repulsion, allowing formation of a layer that is denser than for shorter alkyl chain cation systems. As the potential is made more negative, the longer alkyl chains buckle, forming a ringlike coordination structure supporting penetration of the anion layer by the alkyl chains. This work highlights the powerful combination of spectroelectrochemical and electrochemical methods for elucidation of electrode−electrolyte structure in complex media.

Kang et al. used electrochemical AFM TERS (EC-AFM-TERS) to map heterogeneity in redox behavior across electrode surfaces at the nanoscale during the reduction of Nile Blue (NB).[118] Specifically, these researchers prepared Au(111) triangular nanoplates that were supported on portions of the polycrystalline ITO electrode so that contrast in the redox behavior between electrochemistry at Au(111) and nearby ITO could be monitored using TERS signals. The sharp edges of the Au nanoplates in this experiment supported TERS for NB on the nearby ITO at different applied potentials. $E^{0\prime}$ maps were generated which showed a slight (4 mV) but distinct difference in NB $E^{0\prime}$ at Au(111) compared with ITO, with a unimodal distribution of $E^{0\prime}$ values on Au but a bimodal distribution on ITO. This variance in $E^{0\prime}$ values was attributed to different localized surface charges on the ITO grains. The lateral spatial resolution of this approach on ITO was ∼40 nm, whereas that across the Au nanoplate/ITO edge was about 80 nm. This work clearly demonstrates the power of nanoscale measurement tools in elucidating effects that are not available from macro- or microscale ensemble measurements.

Van Duyne and co-workers also used EC-TERS to investigate the manipulation of individual molecules for tip functionalization in electrochemical environments by potential-dependent transfer of species from a substrate to the tip, similar to what has been done in UHV TERS.[119] This bias-induced approach was used to reversibly functionalize a Ag TERS tip with cobalt phthalocyanine (CoPc) as a test system. It was found that the CoPC transfer is governed by the affinity for interaction with the tip as modulated by electrochemical potential. Although the full scope of generality of this approach remains to be demonstrated, the possibility of tip functionalization in electrochemical environments opens possibilities in areas such as molecular electronics and chemical and biochemical sensing that were inaccessible prior to this work.

Ren and co-workers improved the sensitivity of side-illuminated EC-TERS through the use of a water immersion objective.[120] The limitations of conventional setups originate from optical distortion from mismatched refractive indices of the multilayer media (air, glass, electrolyte) used in conventional setups. Use of a water immersion objective eliminates this optical distortion and increases the numerical aperture, leading to a 5-fold improvement in instrument sensitivity. As a proof-of-concept, the redox chemistry of anthraquinone was studied; interestingly, the TERS signals demonstrated that only 64% of the hydroquinone molecules could be reversibly oxidized despite the quasi-reversible behavior indicated by cyclic voltammetry. These researchers attributed this discrepancy to photoelectrochemistry while under simultaneous illumination and potential control and not simply a tip-induced localized surface plasmon effect. Although the mechanism for this irreversible reduction process remains unknown, this work clearly demonstrates for the first time the requirement for simultaneous illumination and potential to induce this irreversible reduction process.

In two further advances of this earlier work, the Ren group utilized a water-immersion objective with a high numerical aperture in a top illumination geometry EC-AFM-TERS experiment with a thin (∼1 nm) SiO_2-coated Au tip for enhanced mechanical and chemical stability.[121] This approach yielded an enhancement 7 times larger than a bare tip used in conventional setups. Additionally, it was found that the enhancement and best tip−sample separation depends on the cantilever deflection, which should be investigated for each tip type. The collective impact of these improvements was tested by monitoring the redox behavior of thin films of polyaniline as a proof-of-concept. This work demonstrates that tip-based spectroscopy techniques can be configured in capable and robust geometries that should enable probing of local processes in real electrochemical systems of interest.

The use of surface enhanced surface IR spectroscopy for understanding electrochemical interfaces has also continued during this period. Zhang et al. investigated water structure at a monolayer Pd film deposited onto a Au electrode using attenuated total reflection (ATR) SEIRA spectroscopy.[122] Hydrogen adsorption occurs on this electrode in 0.1 M $NaClO_4$ between −0.2 and −0.6 V (vs Ag/AgCl). Using Fourier self-deconvolution of potential difference (relative to +0.3 V) SEIRA spectra reveal three water environments with different ν(O−H) band frequencies: icelike water at 3320 cm^{-1}, liquidlike at 3390 cm^{-1}, and the monomer or multimer state at 3610 cm^{-1}. These researchers observed that icelike water was most prevalent at +0.3 V (vs Ag/AgCl) but diminished at more negative potentials where liquidlike water dominates due to the interfacial disruption caused by hydrogen adsorption. In total, in neutral aqueous solutions, this work documents that the interface is composed of predominantly liquidlike water but with a hydrogen bonding environment that is less well developed compared with bulk solution.

Using synchrotron-based nano-FTIR spectroscopy, Bechtel, Kostecki, and Salmeron and co-workers investigated the interfacial structure of solvents at a monolayer graphene−liquid interface as a function of potential.[123] A clever design in which the single layer graphene was suspended across liquid openings in a holed array of Au allowed probing of the graphene-liquid interface using SINS while maintaining the graphene electrode under potential control. In water, slight blue shifts in the δ(H−O−H) of interfacial relative to bulk water were observed. Spectral signatures from a propylene carbonate−graphene interface similarly showed negligible frequency shifts in vibrational bands suggesting weak interaction with the graphene surface. However, at the graphene electrode−aqueous electrolyte solution interface, pronounced shifts in frequency and the presence of new bands suggested substantial interaction of the electrolyte ions with the graphene surface that varied with potential. This exciting work demonstrates the power of nano-FTIR spectroscopic probes for understanding the details of electrochemical interfacial environments with the possibility for very high spatial resolution.

To better understand the effect of oxidation on the structure of an absorbed species, Shen and co-workers used a plasmonically enhanced vSFG scheme based on Au nanogratings to investigate the electrochemical electrode−solution interface.[124] Building on their earlier work demonstrating the concept of plasmon enhancement of vSFG using thiol self-assembled monolayers on Au electrodes,[125] this work uses the planar surface plasmon excited along the grating to probe the Au−aqueous interface in electrochemical systems without interference from the strong IR absorption of water which attenuates the signal by absorption to unusable levels in the absence of plasmon enhancement. Specifically, they chose two systems with significant spectral overlap of the strong IR absorption in the ν(O−H) region to demonstrate the power of this approach. They monitored the structure of interfacial water species during oxidation of the Au electrode using their interfacial ν(O−H) modes and demonstrated significant changes in vicinal hydrogen bonding. These researchers further studied adsorbed pyridine at the Au electrode surface as a function of potential, a classical model of the electrochemical interface, and verified potential-dependent reorientation of pyridine at the Au electrode surface by monitoring the intensities of the pyridine ν(C−H) modes. This work impressively demonstrates the utility of coupling plasmonic enhancement with nonlinear optical spectroscopies of interfacial systems, providing a nice complement to enhanced linear spectroscopic methods.

A combination of ATR UV−vis spectroscopy and potential-modulated ATR (PM-ATR) spectroelectrochemistry were used by Oquendo andco-workers to elucidate the relationship between molecular orientation and the charge transfer tunneling rate for tethered phosphonic acid-functionalized Zn phthalocyanines (ZnPcs) on ITO electrodes.[126] In PM-ATR, a sinusoidally modulated electric field is imposed about a central dc potential of the tethered redox system. Differences in molar absorptivity values of the neutral and oxidized species leads to an output signal that also modulates at the imposed modulation frequency modified by the electron transfer kinetics. Fitting of these data as a function of imposed modulation frequency allows the electron transfer rate constant to be extracted. For the series of ZnPcs studied in this work, it was found that the most efficient charge transfer occurred for tethered ZnPcs that presented the shortest tunneling distance, a complex function of tether length, molecular orientation, and aggregation state of the ZnPcs on the ITO surface. This work demonstrated the power of ac-based optical methods for understanding fast heterogeneous electron transfer processes, with rates as fast as $(2−4) \times 10^4\ s^{-1}$ successfully measured.

An extension of this approach was reported that utilized PM-total internal reflection fluorescence (PM-TIRF) for tethered luminescent redox molecules such as perylene diimide. Although a useful tool for high surface coverage systems, PM-ATR is generally not sensitive enough to measure electron transfer rates across low surface coverage (i.e., submonolayer) films. However, when the immobilized submonolayer is luminescent, fluorescence detection can enhance the sensitivity. Saavedra and co-workers further extended the PM-ATR concept to demonstrate the first example of potential-modulated total internal reflection fluorescence (PM-TIRF) to determine electron transfer rate constant for a submonolayer film of a redox-active chromophore perylene diimide functionalized with a phosphonic acid tethered to an ITO surface.[127] With only ∼3% of a surface monomer tagged with the redox-active probe, these researchers were able to obtain an electron transfer rate constant to the isolated monomeric redox species on the surface. This value was almost 4 orders of magnitude lower than that measured for a film comprised of aggregated but otherwise identical redox species using PM-ATR. This slower rate constant is likely due to lack of electron self-exchange between monomer units. While this technique will only be useful for molecules with reasonable fluorescence quantum yields, for such systems, these experiments allow a direct comparison of electron transfer rates for submonolayer versus monolayer redox species coverages which may contribute to a better understanding of charge transfer kinetics involving redox-active species in optoelectronic devices.

Simonian and co-workers combined surface plasmon resonance and fluorescence spectroscopy in a new spectroelectrochemical method to study the recently reported electrochemical proximity assay (ECPA), an aptamer-based protein recognition approach for point-of-care testing.[128] ECPA is a quantitative method for determining protein biomarkers using tethered aptamers that, when binding to the target protein, can bring a redox-active reporter close enough to the electrode surface for redox processes to occur, with the magnitude of current flow proportional to the concentration of target protein

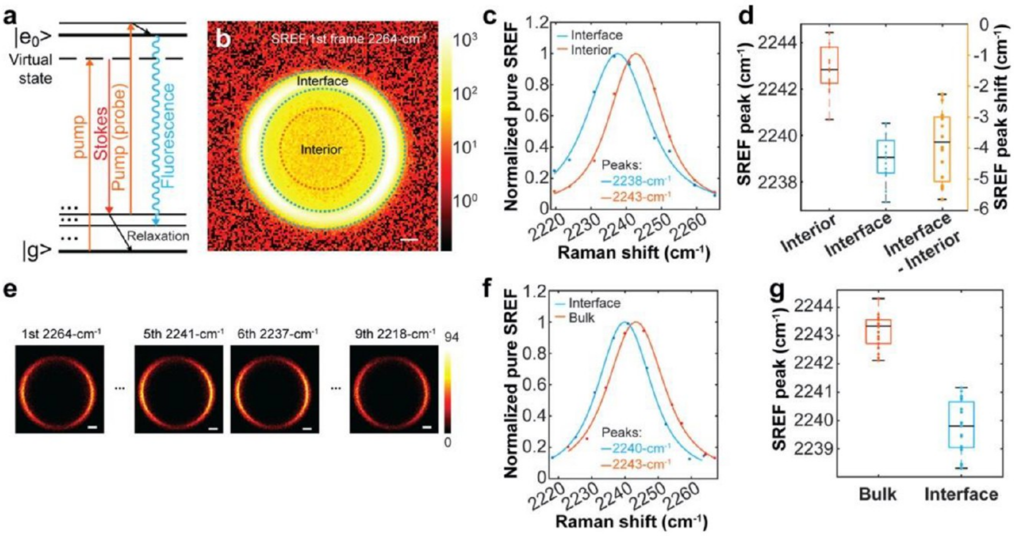

Figure 6. SREF imaging of water microdroplets in oil. (a) Energy diagram of SREF. (b) First frame (excitation at 2264 cm^{-1}) of typical hyperspectral SREF imaging of the Rh800 nitrile mode of a water microdroplet (prepared with an initial concentration of Rh800 molecules of 20 μM) in hexadecane. (c) Background-subtracted SREF spectra of the Rh800 nitrile mode in the interior (red curve) and at the interface (blue curve) of the microdroplet in panel b. Red dots and blue dots represent the signal averages from the interior region and from the interface region, with their corresponding fitting results. (d) Box plot of independent measurements of the Rh800 nitrile peak position in the interior and at the interface and the corresponding Stark shift. (e) Typical hyperspectral SREF image series of microdroplets (prepared with an initial concentration of Rh800 molecules of 50 nM) in hexadecane and (f) corresponding typical background-subtracted SREF spectra of the microdroplet interface (blue curve) and a 20 μM Rh800 bulk water solution (red curve). (g) Box plot of the distribution of Rh800 nitrile peak positions. Scale bar, 2 μm. Reprinted with permission from Xiong, H.; Lee, J. K.; Zare, R. N.; Min, W., *J. Phys. Chem. Lett.* **2020**, *11*, 7423−7428 (ref 133). Copyright 2020 American Chemical Society.

bound to the surface. In the combined SPR/fluorescence spectroelectrochemical approach, the change in current can be correlated to optical changes in the surface bound sensing layer allowing validation of the purported sensing dynamic processes to be achieved in real time. The ability to monitor dynamic structural changes with simultaneous electrochemistry and two optical techniques demonstrated by this study opens the door to investigation of other dynamic processes in critical electrochemical applications.

In another novel approach, Su and co-workers developed an electrochemiluminescence (ECL) self-interference spectroscopy technique (ECLIS) with exquisite nanoscale spatial resolution along the axis normal to the electrode surface.[129] Superposition of the ECL emitted by lumiphores at various vertical spatial positions with that reflected from the electrode surface results in a spectral response that consists of orderly distributed peaks atop the broad luminescence band. Applying the matrix propagation model to these interference fringes enables the distance of the lumiphore from the surface to be estimated. The method was first demonstrated using lumiphores covalently coupled to the electrode surface through a series of double-stranded DNA linkers and was then extended to estimate the depth and thickness of the interfacial region responsible for ECL in the freely diffusing classical system of $Ru(bpy)_3^{2+}$ with tri-*n*-propylamine. This approach should facilitate better understanding of reaction mechanisms of ECL systems and may be extendable to development of ECL-based bioassays.

Several significant studies of unconventional electrified interfaces have also been published during this period. In investigating an unconventional electrical double layer, Allen and co-workers used vSFG to investigate the speciation of Fe(III) species at aqueous−air and air−glycerol interfaces from solutions containing $FeCl_3$.[130] Concentration-dependent vSFG spectra indicate interfacial water reorganization in the presence of $FeCl_3$. At relatively low concentrations, increased water ordering suggests an electrical double layer created from Cl^- at the interface with the corresponding Fe(III) in solution. However, as the concentration of $FeCl_3$ is increased, the loss of this ordered water is observed, suggesting strong interfacial ion pairing or Fe(III) complex formation occurs with centrosymmetric water solvation that diminishes the vSFG signal. Similar results were observed for glycerol−air interfaces in comparable glycerol solutions containing $FeCl_3$.

Studying another electrified interface, Borguet and co-workers probed the heterogeneous charge distribution at the α-Al_2O_3 (0001)/H_2O interface through the Stark-active ν(C≡N) mode frequency of SCN^- by vSFG as a function of solution pH.[131] Spectral fitting allowed identification of four discrete SCN^- species at the interface depending on solution pH. The major interfacial species at all values of solution pH was identified as Al−O−H---S−C≡N^- at neutral aluminol sites, which are the dominant surface aluminol sites at every pH. At positively charged sites in acidic solutions, the minor surface species is SCN^- electrostatically attracted to the protonated aluminol site in an orientation with its N atom pointing toward the surface and the S atom pointing toward the bulk. At negatively charged surface sites, strong electrostatic attraction of K^+ counterions occurs which then electrostatically attract SCN^- species resulting in ion pair adsorption. The interfacial sensitivity of vSFG allowed for the first time the elegant elucidation of surface charge heterogeneity at charged metal oxide surfaces in aqueous media.

Using a different Raman spectroscopic approach, Min and Zare and co-workers used the recently developed approach of stimulated Raman excited fluorescence (SREF) microscopy[132] to measure the electric field at the water−oil interface of aqueous droplets in an oil medium.[133] Although previously implicated in various effects in aqueous microdroplets, the existence of such electric fields have not been definitively proved. In SREF, the fluorescence excitation spectrum maps out the Raman line shape of the vibrational mode. Using the Stark effect of electric field on the vibrational frequency of pendant cyano groups in the dye Rhodamine 800 (Rh800), these researchers imaged water microdroplets in emulsions of hexadecane seen below in Figure 6. A clear frequency shift of the ν(C≡N) band (2243 cm^{-1} in bulk solution) as a function of position within the microdroplet was observed, with a shift to lower frequency of ∼4 cm^{-1} for the Rh800 at the microdroplet interface. Using the known Stark shift for this vibrational mode, the interfacial electric field magnitude is ∼8 MV/cm. This work documented for the first time the presence of a strong electric field at the water−oil interface of aqueous microdroplets.

Finally, Geiger and co-workers developed an approach that allows selective extraction of the potential-dependent third order contribution ($\chi^{(3)}\Phi(0)$) to second harmonic signals at charged interfaces from the second order contribution ($\chi^{(2)}$) that results in molecular orientation.[134] By using heterodyne-detected second harmonic generation (SHG), which can measure intensity and phase of the SHG signal, instead of the more standard homodyne SHG measurement, which can measure only intensity, these researchers were able to definitively extract the potential-dependent phase component of the SHG signal from an aqueous-fused silica interface that is responsive to changes in electrical double layer thickness. Across a series of aqueous NaCl solutions of ionic strength ranging from 10^{-6} to 10^{-3} M, the $\chi^{(2)}$ contribution to the signal remained relatively constant while the $\chi^{(3)}\Phi(0)$ component, which is directly proportional to the interfacial potential, decreased due to increased screening within the electrical double layer. These results are significant in that their observation does not require *a priori* assumption of a model such as the Gouy−Chapman model or that the $\chi^{(2)}$ contribution is invariant with potential. The ability to probe interfacial potential without relying on an underlying model allows one to test primitive ion models or mean-field theories for aqueous solutions without external bias. This approach enables better understanding of fundamental electrochemical double layer theory and its application to a range of electrochemical systems.

Energy Storage and Conversion Systems. Understanding and controlling interfacial reactions at inorganic and organic electrode surfaces in modern batteries and fuel cells are critical in improving cycle life and safety of these devices. Common electrode materials of commercial interest are layered lithium-transition-metal oxides ($LiNi_xMn_yCo_{1-x-y}O_2$ or NCM). While recent studies have shown that increasing the Ni content allows greater charge capacity, decomposition, and O_2, and CO_2 gas evolution occur during cycling at lower voltages in these materials along with major capacity loss. Li and co-workers used electrochemical SHINERS for *operando* characterization of two NCM electrodes to monitor interfacial reactions as a function of applied voltage.[135] Using $LiPF_6$ as the electrolyte, the SHINERS spectra of the electrode with higher Ni content reflected the formation of LiF, spinel (CO_3O_4), and rock-salt (NiO) at voltages lower than the electrode with lower Ni content. Based on these spectral results, these researchers were able to propose a viable pathway for decomposition of Ni-rich NCM electrodes involving metal ion reduction with concomitant oxygen release, leading to spinel and rock-salt formation and dehydrogenation of the solvent leading to LiF and other oxyfluoride deposition at the interface. These findings provide additional insight into interfacial reactions at NCM electrodes, facilitating the design of better Li-ion battery systems.

Flores and Berg and co-workers similarly analyzed the local structure and redox activity of Ni-rich $Li_xNi_{1-2y}Co_yMn_yO_2$ with $y = 0.1$ (NCM811), 0.2 (NCM622), and 0.33 (NCM111) as Li-ion cathodes using *operando* Raman spectroscopy during charge−discharge cycling.[136] These systems all share the same local oxygen environment modulated by the substituting metal M. The low frequency Raman spectral data in conjunction with DFT calculations allowed these researchers to map the evolution of structure during cycling; more precisely, they were able to define the local structure of delithiated NCMs and correlate this structure with redox activity. Despite the similarity in composition, this work demonstrates definitively how very small changes in composition can lead to large differences in the local structural environment that affects delithiation. The understanding garnered from this work opens new possibilities for intelligent design of cathodes with more desirable properties.

Aluminum ion batteries (AIBs) are another class of batteries receiving increased attention due to the natural abundance of Al and its potential for high gravimetric and volumetric capacity. Recently, Wang and co-workers used *operando* Raman spectroscopy coupled with X-ray diffraction to investigate Al/flexuous graphite as a new type of cathode material for AIBs. Using the spectral signatures of the flexuous graphite, these researchers followed the intercalation/deintercalation of $AlCl_4^-$ to and from the space between the graphite layers of the host material.[137] After aging the flexuous graphite for 8000 cycles, the graphite G band broadens considerably along with the appearance of a D band in the Raman spectrum of the aged cathode material; these observations suggest formation of increasingly amorphous graphite during potential cycling. Intercalation of $AlCl_4^-$ was confirmed for potentials above 1.50 V, whereas $AlCl_4^-$ adsorption is suggested at potentials less than 1.50 V. Definitive evidence for structural change of graphite cathodes during intercalation/deintercalation had not been reported previously, highlighting the power of the *operando* Raman spectroscopy approach.

In seeking to overcome slow electron transfer kinetics in vanadium redox flow batteries, Roberts and co-workers studied nitrogen doping of carbon paper electrodes as an alternative to the typical heat pretreatment of the carbon paper in air. Raman spectroscopy was used to rationalize the increased catalytic activity of the nitrogen-doped carbon by correlating the Raman 2D band and the intensity ratio of the 2D band to the G band with electrocatalytic activity.[138] These researchers demonstrated that, although the typical heat pretreatment of carbon paper in air leads to an increased surface area, it does not lead to an increase in catalytic activity. In contrast, nitrogen doping of carbon paper leads to greater catalytic activity for the VO^{2+}/VO_2^+ redox chemistry. Careful Raman imaging demonstrated somewhat surprisingly that nitrogen doping occurs primarily at the carbon fibers rather than in the carbon paper matrix despite its greater disorder. Enhanced catalytic activity was rationalized from changes in the Fermi energy inferred from the Raman spectra.

Operando Raman spectroscopy was also used to monitor simultaneously chemistry at the anode, cathode, and in the electrolyte of a rechargeable organic battery by Lin and Fichtner and co-workers for a battery a composed of a porphyrin−metal complex [5,15-bis- (ethynyl)-10,20-diphenylporphinato]copper(II) (CuDEPP) anode, a graphite cathode, and a 1-butyl-1-methylpiperidinium TFSI$^-$ ionic liquid electrolyte.[139] These researchers studied the chemistry of the anode, cathode, and electrolyte to gain an understanding of the electrochemical energy storage process. During charging of the CuDEPP anode, Raman bands from the porphyrin ring and ethynyl substituents changed significantly, but these changes were found to be fully reversible after discharge. In addition, bands from the cation of the ionic liquid electrolyte increased in intensity, electrostatically attracted by reduction of the CuDEPP. In contrast, bands from the Cu−N and benzene functionalities of CuDEPP were relatively unchanged during charging/discharging. Finally, intercalation of the ionic liquid anion into the graphite cathode resulted in the observation of a new graphite *G*′ band during charging that disappeared after discharging. This study demonstrates the power of simultaneous Raman spectral monitoring of all battery components during charging/discharging cycling in fully understanding the energy storage process.

Understanding the factors that govern ion solvation and transport at interfaces in Li ion batteries is critical for the design of robust and stable high-performance battery electrolytes. Using a nanogap SERS structure, Nanda, Hallinan, and co-workers probed Li$^+$ salt solvation in the aprotic solvents ethylene carbonate and diethylene carbonate in the vicinity of a solid−liquid interface.[140] Incorporating a Au NP monolayer as the plasmonic substrate, the solvation numbers of the Li$^+$ systems were determined. The solvation numbers from these SERS experiments were then compared with those for the same systems determined with standard FTIR and Raman spectroscopy to ascertain any differences. In general, the solvation numbers determined from standard FTIR and Raman were larger than those reported by nanogap SERS suggesting that these less locally specific tools are sensitive to solvation layers beyond the primary layer.

Liu and co-workers used *operando* SERS coupled with impedance spectroscopy to understand the mechanism of the water-mediated sulfur tolerance of a proton conducting oxide of a ceramic-metal anode of solid oxide fuel cells (SOFCs).[141] It is well-established that small amounts of sulfur impurities degrades the performance of SOFCs over time, limiting their longevity. The effects are believed to be associated with degradation of the anode, although significant advances in developing more sulfur-tolerant materials based on barium cerate-zirconate ($Ba(Zr_{1-x}Ce_x)O_{3-\delta}$) have been realized. This work addresses the sulfur-induced chemistry of this proton conducting oxide material. SERS is useful in these studies because it allows observation of *operando* surface species formed upon exposure to only parts-per-million levels of sulfur-containing species. Although the traditional view is that mobile oxygen anions are responsible for removal of surface adsorbed sulfur-containing species, by monitoring the intensity of the surface $-SO_4$ Raman band at 980 cm^{-1}, these researchers discovered that sulfur mitigation was more efficient in moist fuels than dry fuels, leading to the hypothesis that adsorbed water may be equally effective in removing surface sulfur species by the overall reductive process of $SO_4^{2-} + 2\ H_2O\ (g) + 2\ e^- \rightarrow 4\ OH^- + SO_2\ (g)$. Time-resolved analysis was performed to further highlight the strength of the *operando* Raman technique to probe SOFCs under operating conditions. Overall, this study provides important insight into mitigation of sulfur poisoning in these systems.

Optical spectroscopies have also played a central role in elucidating surface and interfacial aspects of energy conversion processes that rely on redox reactions of simple fuels such as CO_2, O_2, and water. Katayama, Shao-Horn, and co-workers used *in situ* ATR-SEIRA spectroscopy coupled with ambient-pressure X-ray photoelectron spectroscopy and DFT calculations to understand the differences in mechanistic detail for CO_2 reduction (CO2RR) on Pt, Au, and Cu metal catalysts.[142] The detailed and specific information on surface species as a function of potential provided by the ATR-SEIRAS approach show convincingly that C-bound intermediates such as CO_{ad} or $COOH_{ad}$ dominate on Pt and Au surfaces but that both C-bound and O-bound intermediates, such as $CO_{3,ad}$ are prevalent on Cu surfaces. Specifically, the O-bound species $CO_{3,ad}$ and C-bound species $(H)CO_{ad}$ were deemed responsible for the formation of C1- and C2-containing hydrocarbon products. Collectively, these findings indicate that the metal catalyst preference for C-bound and O-bound intermediates affects the results, as strong O-binding accelerates the formation of the desired intermediates but too strong an interaction suppresses hydrogenation and desorption. Understanding the mechanistic details of these processes will facilitate design of CO2RR electrode catalysts with enhanced efficiency.

Gewirth and co-workers used EC-SERS to investigate the high surface area, electrochemically deposited Cu and Cu−Ag and Cu−Sn alloy electrodes deposited in the presence of the electrodeposition additive 3,5-diamino-1,2,4-triazole (DAT) as catalysts for selective CO_2 reduction.[143] By monitoring the intensities of the low frequency SERS bands associated with Cu_2O (415, 534, and 620 cm^{-1}) and chemisorbed CO (279 and 360 cm^{-1}) as a function of electrode potential, their results show a clear inverse correlation between the presence of Cu_2O on the surface and the production of CO and C_2 species (C_2H_4 and C_2H_5OH). Ready access to the low-frequency region attendant to such EC-SERS studies provided a window into the mechanistic details of such catalytic electroreduction processes of simple molecules.

Kemna et al. analyzed CO_2 reduction at Pt electrode in a [BMIM][BF_4] ionic liquid using a combination of *operando* IR spectroelectrochemistry and vibrational sum-frequency generation (vSFG).[144] The IR analysis revealed the formation of a [BMIM]-COOH intermediate species in the presence of CO_2 through the electrochemical reduction of the BMIM cation to a carbene which then forms carboxylic imidazolium adduct that can then strongly hydrogen bond with itself as indicated by the growth of bands at 1670 and 1633 cm^{-1} for the monomer and dimer, respectively. With a subsequent anodic sweep in the presence of water, this species can be oxidized back to the original BMIM imidazolium cation and formic acid. The vSFG, which specifically probes only the Pt surface species, further indicates that, in the presence of relatively high water content, small amounts CO can be formed on the Pt surface during the cathodic sweep. The ability to probe mechanisms using both IR spectroelectrochemistry and vSFG provide the first experimental glimpse of the complexity of the reaction chemistry occurring during CO_2 reduction in an ionic liquid medium.

Metal organic frameworks (MOFs) can exhibit structural changes in response to external stimuli that can alter MOF function. In certain MOF catalytic systems, catalytic active sites can be distorted such that activity is either diminished or enhanced. To investigate the effect of structural alterations on MOF electrocatalysis, Korienko and co-workers utilized a combination of *in situ* Raman and ATR-IR spectroelectrochemistry.[145] As a catalytic electrode, a Mn-porphyrin containing MOF (Mn-MOF) was grown on a thin layer of TiO_2 deposited on a fluorine-doped, tin oxide-coated glass substrate. UV−vis spectroelectrochemistry was used to characterize the porphyrin electronic spectroscopic features. These features change somewhat for the porphyrin upon incorporation into the MOF indicating a change in coordination environment. Upon electrochemical reduction from Mn(III) to Mn(II), the Soret band exhibits a blue shift of ~35 nm. Using laser excitation in resonance with the Mn-porphyrin Soret band, resonance Raman spectra indicated significant potential dependent changes consistent with changes in Mn coordination. Upon reduction of Mn(III) to Mn(II), the spectra indicate loss of an axial ligand in the MOF as substantiated by the disappearance of metal−ligand Raman bands at 223 and 241 cm^{-1}. Corroborated by ATR-IR difference spectroscopy, reducing the Mn center results in growth of IR bands corresponding to deprotonated carboxyl groups due to structural changes of the MOF. These changes were shown to be reversible, albeit with different kinetics. Upon introduction of CO_2 into this system, new vibrational bands tentatively attributed to carboxylate modes of an intermediate in the catalytic cycle were observed, along with evidence of a CO product. This work represents the first *in situ* observation of structural changes in a MOF upon electroreduction of the metal center and the first observation of CO_2 reduction intermediates during active electrocatalysis in a MOF.

Interfacial and surface vibrational spectroscopies have also been used to probe the oxygen reduction reaction (ORR) in various media. Kukunuri and Noguchi used *operando* SEIRA spectroscopy to probe the ORR at a $Pt/HClO_4$ interface.[146] To be able to detect low concentration intermediate species, a Pt electrode was sputter coated on top of a roughened Au thin film to provide surface enhancement. This configuration allowed detection and confirmation of the presence of low concentration superoxide species (O_2^-) from the presence of new a band at 1095 cm^{-1} that were not detectable on a Pt electrode in the absence of the underlying Au surface. Further corroboration of superoxide generation was provided by isotopic labeling experiments using $^{18}O_2$ and D_2O. The confirmation of O_2^- species in an acidic medium in the vicinity of the electrode surface suggests that the interfacial pH is much higher than that of the bulk solution during oxygen reduction. This work provides additional insight into the ORR mechanism on Pt-based electrocatalysts.

In another study of the ORR, Van Duyne and co-workers investigated the structure and activity of iron(II) phthalocyanine (FePC), a model catalyst for the ORR, using *operando* EC-TERS.[147] The ability to locate the TERS tip immediately above a single FePc molecule produces definitive evidence that the ORR is catalyzed by the FePc and not by the underlying Au surface. During the investigation, it was found that the FePc is capable of undergoing both reversible change and irreversible degradation during catalysis of the ORR. The reversible change in FePc involves reconfiguration of the FePc from a planar to a nonplanar configuration during ORR due to the formation of oxygen-containing adducts at the Fe center which pulls the Fe ion up and out of the plane of the Pc ring leading to slight ring pucker. In contrast, the irreversible degradation upon extended polarization in the ORR region involves demetalation of the FePc to the free base Pc molecule, driven by the overall thermodynamic stability of hydrated free Fe^{2+}. Thus, the reversible change can be seen as a precursor step to the irreversible degradation leading to free Fe^{2+} and the free base but otherwise intact Pc ring. This work showed definitively for the first time that this demetalation occurred by distortion of the FePc during catalysis and not through electrochemical degradation of the Pc ring to amorphous carbon.

Cowan and co-workers used potential-dependent SHINERS to study water oxidation at electrocatalytic IrO_x thin films electrochemically deposited onto glassy carbon electrodes.[148] The Ir centers of the electrocatalyst undergo activation to the $Ir^{4.x+}$ state followed by the subsequent reaction with water. Significantly, these researchers observe a weak band at 813 cm^{-1} whose intensity is directly correlated with the water oxidation current. This peak was assigned to an Ir oxo intermediate (Ir═O) that leads to formation of a postulated surface Ir−O−OH intermediate with subsequent O_2 evolution. The high sensitivity of the SHINERS approach, particularly in the low-frequency region where these difficult to observe metal−oxygen surface intermediates are observed, has provided definitive information for the first time about surface intermediates that had been speculated to be involved but not previously directly observed.

vSFG has been used by Tian and co-workers to better understand the physical basis of the electrical power generated by moving a droplet of an aqueous ionic solution across a graphene layer supported on a polymer surface under the influence of an electrical potential.[149] This work confirmed that the ordered surface dipole moment from ordered carbonyl groups on the poly(ethylene terephthalate) (PET) polymer surface under the graphene sheet provides the driving force for selective Na^+ adsorption at the graphene/solution interface. Under the driving force of gravity, as the adsorbed Na^+ flow across the graphene surface, electrons generated in the graphene move in the opposite direction to complete the circuit. The vSFG clearly documents the presence of this ordered surface dipole of the PET carbonyl groups at the PET/graphene interface through a strong ν(C═O) band at 1725 cm^{-1} that is absent in control studies with PMMA, which does not show similar carbonyl group ordering at the PMMA/graphene interface and no current generation in the graphene film.

Advances in optical spectroscopies for the analysis of electrochemical systems have enabled researchers to probe electrochemical interfaces with unprecedented success, leading to a more complete understanding of relevant molecular structure, orientation, reactivity, and mechanistic details. Given the significant and timely interest in electrochemical systems, especially those for power generation and storage, one can reasonably predict continued focus on the use of these tools as complementary to electrochemical methods for probing electrochemical interfaces in model and device-relevant systems.

■ CHARACTERIZATION OF MATERIALS SYSTEMS

The study of new materials and their interfaces remains an active area of research. A variety of optical spectroscopies have been applied to study surfaces and interfaces of a wide array of different materials systems. Here, notable applications of such techniques are described for surface and interfacial characterization of low dimensional materials, inorganic semiconductors, and organic semiconductors. Additionally, emerging methods are noted.

Polymers and Buried Interfaces. Interfaces of different materials with polymers continue to be important in multiple technologies and, as such, continue to receive attention with new and novel spectroscopic studies reported frequently. As an example, a key consideration for the widespread commercial production of flexible electronic devices is the interfacial adhesion between metallic coatings and polymer surfaces. Chen and co-workers studied such interfaces for the first time utilizing AFM-IR.[150] They identified characteristic peaks of the modified polymer at the metal−polymer interface. In concert with data from X-ray photoelectron spectroscopy (XPS) and scanning electron microscopy (SEM), these researchers proposed a molecular bonding mechanism of adhesion, providing greater understanding of these important interfaces.

Marcott and co-workers used optical photothermal IR (O-PTIR) spectroscopy to probe the interfacial boundary of a laminate consisting of two bioplastics, poly[(*R*)-3-hydroxybutyrateco-(*R*)-3-hydroxyhexanoate] coated onto poly(lactic acid), at a spatial resolution below that attainable with a conventional IR microscope.[151] In their setup, a pulsed IR QCL is made collinear with a visible laser and then focused onto the sample through a microscopic objective. Upon absorption, the photothermal response is probed through the modulated component of the reflected visible laser, which has a much smaller spatial diffraction limit than the IR source. Moreover, when the scattered visible light is returned to the detector, not only can the IR signal be extracted but the Raman scattered radiation can be diverted to a spectrometer to allow acquisition of simultaneous IR and Raman spectra. O-PTIR has several advantages over traditional FTIR, including wavelength-independent spatial resolution of ∼500 nm and the ability to obtain complementary and confirmatory Raman spectral data at the same time. Obtaining both single frequency spectral images along with individual IR spectra along the bioplastic interface, these researchers captured gradual spatial intensity changes that span several micrometers. Since the two plastics are immiscible, this gradual change across the interface and lack of isosbestic point is unexpected, since in an ideal binary system of noninteracting polymers, the composition would be expected to change abruptly at domain edges. The fact that a gradual change is observed indicates a much more complex compositional change at the interface between the two polymers that must include spatially dependent intermixing of the polymers to a certain extent, despite their purported immiscibility. Additional insight into this intermixing as well as information about microstructure of each polymer component across the interfacial regions was provided from synchronous and asynchronous two-dimensional correlation spectroscopy with both the O-PTIR and Raman spectral responses.

The use of polymer composites is ubiquitous, and their properties are often largely determined by the interfacial adhesion between the polymer matrix and inorganic filler. Understanding the properties of matrix−filler adhesion is especially important for tensile deformation during elongation or stretching of polymer composite materials. To characterize the behavior at this interface, Shinzawa and co-workers developed a rheo-optical FTIR imaging system that allows acquisition of polarized FTIR spectra while a polymer sample is mechanically perturbed through an increasing application of strain.[152] The spectra are then analyzed by disrelation mapping based on two-dimensional correlation spectroscopy (2D-COS) analysis, with disrelation intensity developing when the absorbance at two different frequencies varies mutually out-of-phase. This approach allows identification of sites where molecular deformation is most prominent. To demonstrate the utility of this technique, two polymer composites were studied. Both contained a mixture of hydroxylated polypropylene and either unmodified silica spheres (PPOH/SS) or silica spheres surface modified with ocatadecyldimethyl groups (PPOH/mSS). In PPOH/SS, the unmodified silica spheres interact with the polymer through hydrogen bonding, whereas the octadecyldimethyl layer acts as a spacer between the polymer and the modified silica spheres. Thus, more strain was required to deform the PPOH/SS composite than the PPOH/mSS composite, which was attributed to greater adhesion between the PPOH matrix and the unmodified silica spheres. Two vibrational bands of interest for the disrelation analysis are intramolecular C−H vibrations at 810 cm^{-1} from long helixes of largely crystalline polypropylene and 842 cm^{-1}, more indicative of short helixes associated with amorphous domains. The synchronous spectrum of a mechanically elongated pure PPOH sample exhibits several correlation peaks suggestive of correlated changes of the helical structure throughout the sample. However, the asynchronous spectrum indicates that the intensity changes at 842 cm^{-1} occur prior to changes at 810 cm^{-1}, suggesting that stretching of the polymer causes changes in the amorphous regions before changes in the crystalline regions. Analysis of higher frequency regions indicate changes in hydroxyl group interactions with increased tensile strain as well. For the PPOH/SS composite, the presence of an additional disrelation envelope with two maxima at 842 and 825 cm^{-1} indicates additional changes induced with the addition of the silica spheres. Comparison of the disrelation maps of the (842, 810 cm^{-1}) envelope from PPOH/SS and PPOH/mSS samples shows smaller disrelation intensities for PPOH/mSS, further substantiating the assertion of weaker interfacial adhesion with modified silica spheres. Combining the capabilities of FTIR imaging with tensile deformation and 2D-COS analysis represents a powerful tool for better understanding interfacial interactions in polymer composites.

Beyond being a powerful surface scanning technique, nano-FTIR can also be utilized to probe subsurface, nanoscale features at depths up to ∼100 nm. Hillenbrand and colleagues have also systematically explored the utility of nano-FTIR for multilayered systems by probing thin films of PMMA covered by polystyrene (PS) of thicknesses varying from 0 to 110 nm.[153] PMMA was identified by its characteristic $\nu(\text{C}{=}\text{O})$ band at 1738 cm^{-1}; PS is silent in this spectral region but can be uniquely identified by its $\nu(\text{C}-\text{C})$ bands at 1452, 1493, and 1601 cm^{-1}. With the increase in PS thickness, the PMMA $\nu(\text{C}{=}\text{O})$ band decreases in intensity and shifts to higher frequencies by up to 7 cm^{-1} for a 110 nm-thick PS film. These results were consistent with predictions from finite dipole model (FDM) calculations. These researchers additionally noted that with increasing PMMA thickness, the relative contrast of the signal at the higher harmonic demodulation orders of 3 and 4 decreased due to greater confinement of the near field at the tip apex. This observation suggests that identification of surface or subsurface layers could be deduced from analysis of peak intensity ratio at different demodulation orders for a single vibrational band. For systems such as PMMA/PS in which frequency shifts due to chemical interactions are unlikely, nano-FTIR can be a powerful technique for differentiating layers of an unknown sample. This work is an important contribution to the nano-FTIR field in that it will allow future use of nano-FTIR in distinguishing frequency shifts caused by sample geometry from shifts resulting from chemical effects such as unique surface and interfacial interactions.

In the related but different approach of AFM-IR, Haufmann and co-workers studied buried poly(acrylic acid) (PAA)−Al_2O_3 interfaces.[154] First, they investigated the PAA ν(C═O) region in thin films on Al_2O_3. For a thin (20 nm) PAA film, the ν(C═O) band for the neutral acid form of PAA at 1718 cm^{-1}, similar to that seen for bulk PAA at 1700 cm^{-1}, was observed along with a new $\nu_{as}(COO^-)$ band at 1602 cm^{-1} due deprotonated carboxylate species formed upon interacting with the Al_2O_3. The observation of COO^- species validated the use of AFM-IR for buried interfaces. Further, the $\nu_{as}(COO^-)$ band was not observed for slightly thicker films (50 nm) confirming its origin at the interface with Al_2O_3. Further confirmation came from examination of the interfacial region directly in a cross-section of the PAA−Al_2O_3 assembly. With the high spatial resolution of AFM-IR, these researchers were able to "map" the transition to the interfacial region through the intensity ratio of the $\nu_{as}(COO^-)$ band to the neutral acid ν(C═O) band as a function of position. As expected, this ratio increased as the probe position approached the interface, confirming that the $\nu_{as}(COO^-)$ band results from species at the interface. This work was the first definitive example of the use of AFM-IR for probing a buried interface.

Mol and co-workers studied the buried polymer−metal (oxide) interface of a polyester/zinc oxide/zinc assembly using the complementary techniques of ATR-FTIR and vSFG with the goal of elucidating the presence of metal−carboxylate complexes that stabilize such interfaces.[155] The nature of interfacial bonding is of central importance for understanding and predicting stability in industrially relevant polyester−metal interfaces such as automotive and industrial paints and metal can and coil coatings. Although ATR-FTIR is the most accessible vibrational spectroscopic technique for study of such interfaces, its significant probing depth of at least several hundred nanometer at large angles of incidence (e.g., 80°) result in information being obtained from a combination of interfacial and bulk molecules. In contrast, vSFG is a truly interface sensitive technique, although it has not been routinely used for study of metal−polymer interfaces. Recent advances in mid-IR laser capabilities have now made feasible vSFG studies of carbonyl and carboxylic acid-containing buried polymer−metal interfaces. This work reports one such study in which the information from ATR-FTIR and vSFG is compared for buried polyester/zinc (oxide) interfaces. ATR-FTIR spectra in the ν(C═O) region indicate the presence of both carboxylate moieties, from zinc (oxide)-carboxylate bonding, and ester groups from regions of the polyester at greater depths from the interface. In contrast, the vSFG spectrum shows only the presence of fully protonated carboxylic acid bands that are not converted to carboxylate moieties in the absence of moisture. Moisture exposure over several days eventually leads to conversion of these carboxylic acids to carboxylates in the vSFG spectra. With further optimization, complementary ATR-FTIR and vSFG measurements could represent a powerful combination of tools for studying buried polymer−metal interfaces.

Li and colleagues similarly utilized the powerful capabilities of vSFG to study buried interfaces involving polymers in an investigation of a buried nylon-maleic anhydride (MAH) grafted polyethylene interface.[156] They found that the nylon C═O groups tilted more toward the interface plane at the nylon−polyethylene interface than they did at the nylon−air interface as well as being able to distinguish signals from grafted and ungrafted MAH groups at the prism−MAH grafted polyethylene interface.

Spatially offset Raman spectroscopy (SORS) approaches have been developed to probe molecular interfaces at large penetration depths. Unfortunately, many of these advances require sophisticated data processing which render this powerful technique less user-friendly than other Raman analyses. To combat this, Cooper and co-workers have incorporated a fiber coupled, spatial heterodyne spectrometer (SHS) in their digital micromirror device (DMD)-based SORS microscope setup to create the technique spatial heterodyne offset Raman spectroscopy (SHORS).[157] The implementation of SHS makes this instrument analogous to a Michelson interferometer, wherein beams are split by a beamsplitter which then reflect from diffraction gratings instead of moving mirrors. The tilt of the gratings generates interfering wavefronts which can be captured as an image on a CCD, and Fourier transformation results in the Raman spectrum. In a direct comparison, these researchers measured a S/N of 11 for a dispersive SORS instrument but a S/N of 104 for the SHORS setup. The utility of SHORS was demonstrated on phantom models of tissue and bone, with the tissue phantom comprised of TiO_2 nanoparticles in a PDMS matrix, and the bone phantom, based on $CaCO_3$ and hydroxyapatite (HAP), placed inside the tissue phantom. For offset values from 0.0 to 1.0 mm, Raman spectra could be observed from depths up to 4 mm. The 960 cm^{-1} band characteristic of HAP and the 1070 cm^{-1} band of $CaCO_3$ increased in intensity as the offset value increased. In fact, the bone phantom bands were visible at the highest offset value even when the depth of the bone phantom was increased to 8 mm, highlighting a possible increased working depth. Similar results were obtained for the bone phantom in a bovine serum albumin (BSA)-polyethylene glycol (PEG)-hydrogel scaffold. This second medium produced noisier Raman spectra than the tissue phantom matrix, which was attributed to increased scattering from BSA centers in the matrix, but this system better mimics what might be observed in nonsynthetic biological samples. Overall, the results demonstrate the power of SHORS for probing even relatively deep buried interfaces and paves the way for the better analysis of biological-based samples and materials.

Although to date only even-ordered nonlinear spectroscopies such as vSFG have achieved true surface specificity, Petti and co-workers proposed an extension to 2D third-order tools such as 2DIR or 2D white-light spectroscopy (2DWL) spectroscopy to make them surface specific as well.[158] The singularly cross-polarized detection scheme proposed provides surface specificity through polarization control that results in all on-diagonal signals and those from the bulk system being

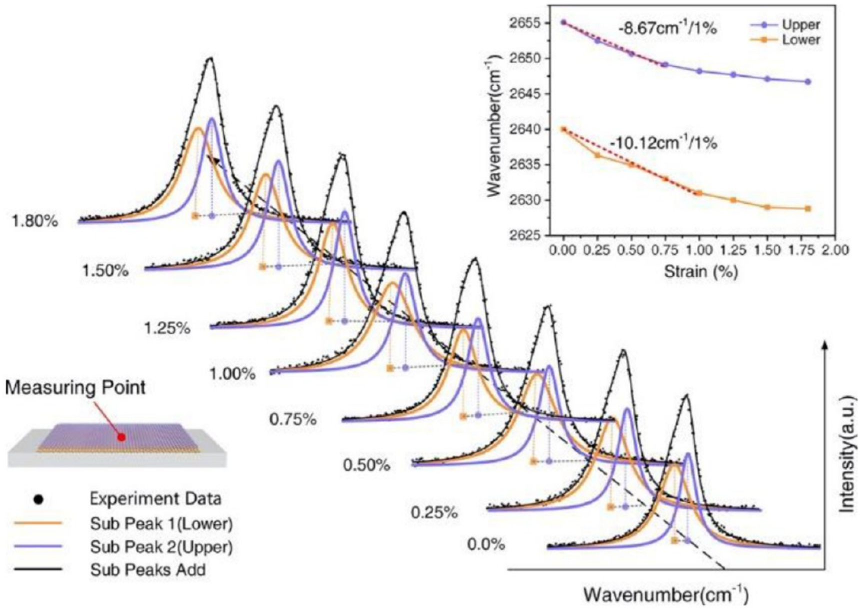

Figure 7. Schematic diagram of the peak splitting result of the midpoint of the double-layer graphene in different substrate strains. The upper right corner shows the peak positions of the upper and lower layers graphene at different substrate strain; the lower left is a representation of the sampling arrangement. Reprinted with permission from Dou, W.; Xu, C.; Guo, J.; Du, H.; Qiu, W.; Xue, T.; Kang, Y.; Zhang, Q. *ACS Appl. Mater. Interfaces* **2018**, *10*, 44941−44949 (ref 159). Copyright 2018 American Chemical Society.

reduced to zero. Thus, the detected spectrum contains only cross-peaks from the ordered interface or surface layer.

2D and Low-D Materials and Films. Low dimensional materials have emerged as promising platforms for numerous applications. Their unique properties, including superconductivity and strong electronic coupling, and fabrication approaches that allow by-design stacked heterostructures offer promising avenues for tuning their physical and chemical characteristics for various chemical analysis uses.

Much of the effort during this past period focused on 2D or low dimensional carbon-based materials such as graphene and carbon nanotubes. Zhang and co-workers used micro-Raman spectroscopy to study the sensitivity to mechanical strain of the graphene 2D Raman band at 2640 cm^{-1} to investigate in real-time double-layer polycrystalline graphene samples on polyethylene terephthalate substrates under microtensile loading of the graphene−graphene interface.[159] For double-layer graphene fabricated by two wet transfer steps, the 2D band splits into two peaks that arise from the independent response of the upper and lower individual graphene layers. The strain information in each layer can be extracted by fitting the envelope to two components, one representing each layer as seen below in Figure 7. A shift to lower frequencies of the 2D band is indicative of tensile strain while a shift to higher frequencies indicates compressive strain. The band intensities also contain useful information. Under small strain applied to the substrate, both layers deform uniformly yielding equal intensities of the two components of the 2D band. However, at larger strains, slip between the graphene layers results in inequivalent intensities of the two components. Plotting the frequency shift of each component as a function of strain allows quantitative assessment of strain information for each layer independently. Finally, double-layer graphene samples with unequal lengths were also investigated, leading to the conclusion that strain in the two layers is concentrated where the shorter of the two layers ends. Understanding the mechanical properties of double-layer graphene will be essential for its use in practical applications. This work clearly documents the utility of micro-Raman spectroscopy as a powerful tool for quantitatively mapping the properties of individual layers in double-layer graphene.

Wang and co-workers developed a super-resolved hyperspectral imaging system in the near IR region to identify single defects in SWCNTs.[160] Their system was based on an InGaAs detector array cooled to −190 °C, instead of the more commonly employed procedure of cooling to −100 °C using liquid N_2, which improved the S/N by over 3 orders of magnitude for weak SWCNT defect photoluminescence signals in the spectral region between 900 and 1300 nm. The additional decrease in cooling temperature suppressed the dark current to only 10 e^- per pixel, a value approximately 500 times lower than comparable InGaAs arrays cooled to −100 °C. By analyzing the temporal dependence and intensity states of the photoluminescence stochastic blinking from synthetically created defects, these researchers were able to identify blinking single defects with very low intensities within the instrument field of view. These synthetic defects were organic color centers incorporated into the SWCNTs by covalent bonding of different functional groups to the sidewalls. Under visible radiation illumination, these defects create exciton traps that emit as single photons in the near IR region of the spectrum. The spatial resolution of a single defect was determined to be 15 nm within a diffraction-limited spot. This approach should facilitate efforts to understand and control chemical defects on SWCNTs in a high-throughput fashion.

Semiconducting SWCNTs, while possessing remarkable properties, are greatly impacted by defects. Zanni and co-workers postulated that since excitons become trapped when encountering defects (limiting lateral diffusion and performance), preparing longer SWCNTs and SWCNTs with fewer defects will result in longer exciton lifetimes and increased energy transfer efficiency.[161] To study this, they utilized TA spectroscopy to measure exciton lifetime dynamics along with photoluminescence excitation (PLE) spectroscopy and 2DWL spectroscopy to create correlation maps to monitor the S_2 and S_1 transitions of SWCNTs prepared by two different methods: shear-force mixing which allows, on average, longer, less defective SWCNTs or a harsher ultrasonication method that yields shorter SWCNTs. The cross-peaks observed in the 2DWL spectra along with quenching in the PLE spectra allowed quantification of the energy transfer. Based on this, they concluded that energy transfer of the shorter SWCNTs prepared by shear-force mixing is ∼20% more efficient. This suggests a link between energy transfer and exciton diffusion and provides guidance in fabricating SWCNT-based devices with improved performance.

Efforts to better understand exciton dynamics of semiconducting SWCNTs using optical spectroscopies were also undertaken in this period. Such studies are difficult because of the inherent heterogeneity of SWCNTs. However, better insight into sample heterogeneity was obtained by Potma and co-workers in a study comparing ensemble TA measurements of (6,5) SWCNTs deposited on glass with similar measurements at the nanoscale on individual nanotubes or nanotube clusters using time-resolved pump−probe PiFM.[162] The time-resolved pump−probe PiFM measurement senses a pump-induced transient polarization on the picosecond time scale in a sub-10 nm region of a sample through the force created on a sharp metal tip. Interestingly, four distinct types of temporal dynamics were observed at the nanoscale that deviate significantly from the dynamics measured in the ensemble measurements; the regions that exhibit these altered dynamics seem to be associated with SWCNT clusters suggesting that they result from unique inter-SWCNT interactions. Despite this heterogeneity observed at the nanoscale in a minority of the sample, the overall dominant behavior at the nanoscale matches that of the ensemble measurements, confirming the relative purity of the (6,5) SWCNT sample. The nanoscale resolution offered by this time-resolved PiFM approach is promising for the future study of dynamics in other low dimensional materials.

Other 2D materials of interest have also received attention during this period. van der Waals heterostructures (vdWHs) are 2D materials with promising applications in many fields. However, conventional fabrication methods for layer stacking often trap unwanted and unidentified contaminants within the layers even when performed in clean environments. Centrone and co-workers used PTIR to identify contaminants found in vdWHs made from WSe_2, WS_2, and hexagonal boron nitride.[163] Using a "nanosqueegee" method, they were first able to concentrate and eventually remove contaminants in "bubbles" near the edges of the samples. The localized concentrated contaminants prior to removal were topographically mapped with AFM and their IR absorbance spectra acquired enabling definitive identification of the poly(dimethylsiloxane) and polycarbonate polymers used in the fabrication stamp materials. Nanosqueegeed regions were proven to be clean by PTIR. The high sensitivity, high spatial resolution, and molecular specificity afforded by PTIR resulted in definitive identification of previously unknown contaminants, allowing mitigation strategies with better fabrication protocols to be devised.

vdWHs from transition metal dichalcogenides are of interest for their ability to contain interlayer excitons (iXs). Recently, Tartakovskii et al. demonstrated using photoluminescence that conventional fabrication of vdWHs through mechanical stacking can lead to transfer-induced anisotropic strain within the two-dimensional layers, thereby significantly changing the optical properties.[164] These researchers found that smoother $MoSe_2/WSe_2$ heterostructures exhibit iX photoluminescence at higher energy whereas vdWHs with more layer corrugation or "wrinkles" exhibit broader, lower energy iX photoluminescence. They further noted that independent of incident light polarization, vdWHs containing more wrinkles produce highly linearly polarized iX photoluminescence, with no circularly polarized light observed which would indicate symmetry breaking. In contrast, smoother vdWHs do exhibit circularly polarized photoluminescence. This difference in optical properties was attributed to iX accumulation at the top of the wrinkles in the rougher sample, where the local strain was greatest. Understanding the origin of anomalous optical properties is crucial for future development and use of vdWHs and other 2D materials. Although this research indicates that random strain defects can negatively affect optical properties of vdWHs, it also demonstrates the potential control of optical properties afforded by engineered wrinkling of such 2D materials.

Ultrafast carrier dynamics in monolayer WS_2 were investigated by Gustafson and co-workers using broadband time-resolved THz spectroscopy.[165] Upon photoexcitation, an increase in conductivity is observed. This is rationalized through exciton creation with subsequent trapping of a subset of electrons in defect sites leaving an additional population of holes in the valence band. These additional holes can be transiently captured by remaining excitons to produce three-body, bound quasiparticles called positive trions which contribute to the photoconductivity. The photoconductivity is frequency dependent and was modeled as a combination of contributions from a Drude component, a broad resonance component, and a dissociation component at the trion binding energy. This work represents the first direct measurement of the trion binding energy in WS_2. The formation of trions are defect-mediated which leads to a saturation of this effect with sufficient photon flux. Overall, this work contributes to an enhanced understanding of nonequilibrium carrier dynamics in two-dimensional systems.

Wu and co-workers reported the first investigation of 2D monolayer boron (borophene) sheets by in situ Raman spectroscopy and TERS at low temperature in ultrahigh vacuum (UHV).[166] Borophene has been shown to exhibit polymorphism indicating that multiple structures exist with similar formation energy. Far-field Raman spectroscopy of borophene is experimentally challenging due to its very low Raman scattering cross-section. Nonetheless, these researchers observed for the first time the far-field Raman spectrum of the β_{12} phase, confirmed by STM, of borophene on Ag(111). Insight into electron−phonon coupling strength can be determined from the spectral line width of the Raman phonon modes. It is known that the anharmonic phonon−phonon coupling in boron is weak; therefore, the Raman line widths observed largely reflect strong electron−phonon coupling. Using the Allen relationship between the line width and the electron−phonon coupling constant λ,[167] λ was experimentally determined to be about 0.53−0.59, comparable to that in graphene. TERS on terraces of the β_{12} phase of borophene exhibited strong enhancement of the B_{3g}^2 phonon mode in which the atomic motions are largely vertical, with an

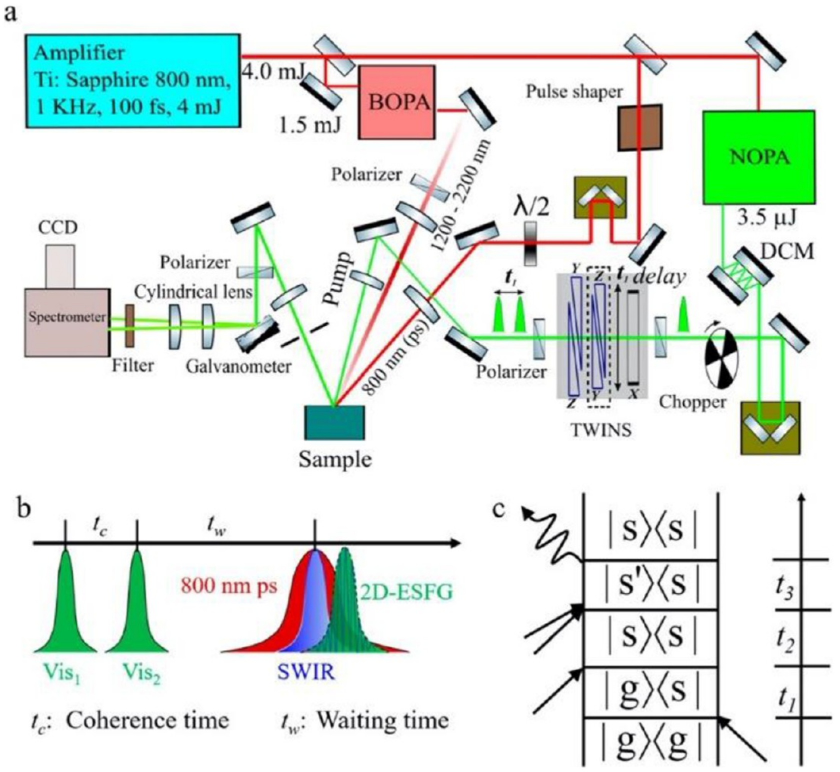

Figure 8. (a) Schematic setup of an interface-specific 2D-ESFG spectrometer. (b) Phase-locked pump pair and two probes (800 nm + SWIR) configured to generate a 2D-ESFG spectrum. A coherence time, t_c, between the two pump beams was controlled by the TWINs system. A waiting time, t_w, between the pump pair and the probes was controlled by a translation stage. (c) One of the double-sided Feynman pathways for 2D-ESFG. g, s, and s′ stand for ground state, surface state, and a higher surface state, respectively. Reprinted with permission from Deng, G. H.; Qian, Y.; Wei, Q.; Zhang, T.; Rao, Y., *J. Phys. Chem. Lett.* **2020**, *11*, 1738−1745 (ref 169). Copyright 2020 American Chemical Society.

enhancement factor of ~3 × 10^9. This enhancement was shown to exhibit an exponential dependence on tip−sample separation with a decay length of ~144 pm. These studies provide a basic understanding of the vibrational behavior of borophene sheets that will underpin further investigation of the mechanical, superconducting, and electronic properties of this interesting material.

Building on their previous efforts to characterize 2D covalent polymer layers by TERS, Zenobi and co-workers used TERS to investigate 2D photopolymerization of a monolayer through [4 + 4] cycloaddition reactions between adjacent anthracene units at the air−water interface and at Au (111) surfaces.[168] TERS provides direct evidence for covalent bond formation between monomeric units and allows quantification of conversion efficiency. For studies at the air−water interface, amphiphilic macrocyclic anthrapene monomers were used to provide the photoreactive anthracene units. This monomer has a rigid cyclophane framework with three anthracene moieties attached along with three hydrophilic diethylene glycol methyl ether units. UV-irradiation of monolayers of this macrocycle at the air−water interface in a Langmuir−Blodgett trough, in which the anthracene units are packed in a face-to-face arrangement, results in polymerization. This photopolymerization process is elegantly followed using TERS by transferring the monolayers to Au(111) substrates at different times after photopolymerization is initiated. Polymerization was indicated by a significant decrease in intensity of the anthracene bands at 1385, 1450, and 1560 cm^{-1} along with an increase in polymer bands at 1168 and 1600 cm^{-1}. This study represents the first reported use of TERS to monitor a 2D polymerization process.

Low-dimensional materials represent a new frontier in nanomaterials research. The expansion of fabrication methods has made these interesting materials more readily available for detail analysis of their unique and potentially transformative properties. Optical spectroscopic methods will continue to represent some of the most important tools with which to study these emerging materials.

Inorganic and Hybrid Organic Semiconductors. Even-order nonlinear optical spectroscopies have been used to provide pivotal information about the structure and dynamics of surfaces and interfaces. While second-order techniques have become more mainstream, and a fourth-order, 2D vibrational technique has been demonstrated (2D-vSFG), to date there have been no examples of fourth-order, 2D electronic sum frequency generation spectroscopic (2D-ESFG) techniques. In recent work, Deng et al. describe implementation of a novel 2D-ESFG experimental method using the instrumental arrangement in Figure 8.[169] In short, their amplifier was split into three different beams. The first portion was used in a broadband optical parametric amplifier (BOPA) to generate a short-wave IR (SWIR) beam, the second portion generated a picosecond laser (800 nm) with a pulse shaper, and the third portion pumped a noncollinear optical parametric amplifier (NOPA) from 500 to 750 nm. This beam generated from the noncollinear optical parametric amplifier was compressed with two chirp mirrors and sent to a translating wedge based identical pulses encoding system (TWINS) which then generated phase-locked double pump pulses. This pump pair along with the 800 nm picosecond beam and the SWIR beam were spatially overlapped, and the 800 nm picosecond beam and the SWIR beam were spatially and temporally overlapped at the sample surface. The resulting 2D-ESFG spectrum was collected between 480 and 590 nm by a spectrometer with a CCD. The researchers applied this novel method to *n*-type and *p*-type GaAS surfaces to obtain information about the coupling of the surface states of the semiconductors. Although their measurements suffered from generally weak signal and distortion from coherent excitation scattering, they were able to observe couplings due to the presence of off diagonal peaks along with observing dark states due to the absence of some diagonal peaks, a result that would be impossible to obtain with one-dimensional ESFG. There is much work to be done to improve this technique, but when optimized, it could become a useful tool for probing the electronic properties of interfacial systems such as thin semiconducting films.

Hybrid organic−inorganic perovskite thin films remain a topic of considerable research interest for photovoltaics despite their well-known chemical instability under atmospheric conditions. Using IR s-SNOM, Nishida and co-workers probed heterogeneity and cation−lattice interactions in thin films of a triple cation formamidinium (FA)-methylammonium (MA)-Cs^+ perovskite.[170] The FA vibrational resonance acts as a reporter of its local environment and from subtle differences in its vibrational line shape, important information about composition, spatial heterogeneity, and cation−lattice interaction dynamics can be extracted. For perovskites that contain FA cations, the ν_{as}(CN) band areas, frequencies, and line widths report on different aspects of the film. The band area reflects the concentration of the FA cation with the nanoexcitation volume, thus reporting on composition. The peak frequency of this band reflects differences in cation−lattice interactions reflecting heterogeneity in perovskite lattice structures. Finally, the line width of this band is a measure of cation−lattice coupled vibrational dynamics. Pristine perovskite films used in this work were intrinsically polycrystalline with grain sizes of ∼100 nm as reflected by integrated area, peak frequency, and line width of the FA ν_{as}(CN) band. Upon water vapor annealing, the average grain size increases to >200 nm and the ν_{as}(CN) band areas, frequencies, and line widths remained relatively the same as those of the pristine films. Nonetheless, despite larger grain sizes, the correlation lengths deduced from the s-SNOM parameters over multiple data sets do not evolve accordingly, suggesting subgrain heterogeneity. This is rationalized as reflecting fusion of the grains at grain boundary edges without homogenization of the bulk supergrains so produced. Interestingly, the absence of significant vibrational area-frequency and area-line width correlations indicates that the FA concentration is not a dominant factor in dictating lattice structure and dynamics. In contrast, the vibrational band frequency and line width is observed to be correlated both in pristine films and in water vapor annealed films, suggesting that the cation−lattice interaction strengths and their associated vibrational dynamics act in concert. This effect is rationalized through a nonuniform distribution of Cs^+, which both contracts the lattice and slows the lattice dynamics. Uneven cation−lattice interactions influence the elasticity of the lattice and can lead to disordered charge-phonon coupling and polaron formation. IR s-SNOM is thus demonstrated to be a powerful nanoscopic probe of local cation−lattice interactions and their vibrational dynamics in these complex triple-cation perovskite semiconductor thin films.

Yu and co-workers used a combination of PTIR and AFM to study the degradation of a organic−inorganic hybrid perovskite thin film under ambient conditions with a spatial resolution of ∼20 nm.[171] Films of $MAPbI_{3-x}Cl_x$ with average grain sizes of 300−600 μm were studied; AFM topographic images and FTIR spectra were acquired at various spots in the grain boundaries and in the grain interior correlated with photoluminescence mapping images. The FTIR spectral evidence confirms more degradation at the grain boundary through a loss in intensity of characteristic outer Helmholtz plane bands and the increase of mixed ν(O−H) bands around 3400−3600 cm^{-1} with a concomitant decrease in the ν(N−H) at ∼3300 cm^{-1} that are indicative of adsorbed H_2O and O_2-initiated reactions. The ability to probe this chemistry with molecular specificity on the nanoscale allows confirmation of the initiation of degradation at grain boundaries. Studies such as these are critical for the emergence of rational design principles for the optimum manufacture of OHP thin films.

To overcome limitations due to small electrolyte volume during *operando* analysis of photoelectrochemical systems, Smith and Venugopal and co-workers developed a novel approach called photoelectrochemical attenuated total reflection Fourier transform infrared (PEC-ATR-FTIR) spectroscopy to investigate metal oxide−electrolyte interfaces.[172] Utilizing this approach, $BiVO_4$ thin films were studied as a model multinary metal oxide photoelectrode. Photocharging led to a loss of IR bands at 682 and 802 cm^{-1} for the ν_{as}(V−O) modes and the 894 cm^{-1} band for the ν_s(V−O) mode while the 640 cm^{-1} band for the ν_s(Bi−O) mode remained unchanged. Loss of the ν(V−O) bands during photocharging with retention of the ν_s(Bi−O) indicates loss of V at the interface. Preferential loss of V results in a Bi-rich surface layer on top of the bulk $BiVO_4$ creating a heterojunction that facilitates band bending with concomitant improvement in PEC performance. The ability to probe PEC performance using a molecularly specific probe such as FTIR spectroscopy under illumination conditions with and without applied potential allows new insight into the dissolution of metal oxide components in PEC devices, thereby paving the way for more robust PEC technologies.

Organic Semiconductors. While advances in organic solar cell technology have resulted in power conversion efficiencies of greater than 15% in numerous systems, their operational and environmental stability remains poorly characterized. Vaynzof and co-workers studied degradation of the model system poly[(5,6-difluoro-2,1,3-benzothiadiazol-4,7-diyl)-*alt*-(3,3‴-di(2-octyldodecyl)-2,2′;5′,2″;5′′,2′′′-quarterthiophen-5,5′′′-diyl)]:$PC_{71}BM$ under combined oxygen and light exposure using femtosecond TA spectroscopy and ultrasensitive photothermal deflection spectroscopy (PDS).[173] TA spectroscopy showed broad excited state absorption in the near-IR and subsequent charge separation occurring almost completely within the initial 15 min of degradation. Furthermore, as degradation progressed, exciton lifetime decreased. Significant charge separation was observed even in degraded films. The PDS data allowed measurement of the sub-bandgap absorption of the system, and as degradation progressed, an absorption increase of almost an order of magnitude below the bandgap was noted. Coupled with a loss in device performance after degradation and XPS and ultraviolet photoelectron spectroscopy experiments that showed no evidence of photodegradation products, their results suggest that loss of efficiency is due to p-doping of the active layer with concomitant formation of trap states. That this doping is reversible was further confirmed by performance recovery after storage of the device in vacuum. These results emphasize the need for effective encapsulation of devices, even if photodegradation does not occur, to prevent incursion of O_2.

Although fullerene systems are still prevalent as acceptors, push−pull molecules with alternating donor and acceptor units represent a new frontier in organic photovoltaics (OPVs). Watts and co-workers studied degradation of three small push−pull donor molecules upon continuous exposure to radiation under ambient conditions. The molecular systems chosen for study in this work were based on benzodithiophene terthiophene cores (BDT-3T) with electron acceptor end-caps of either benzothiazoleacetonitrile, pyrazolone, or barbituric acid.[174] These molecules were designed by theory to possess highly similar optoelectronic and redox properties. Over the course of days of exposure, all three films photobleached to varying degrees based on their UV−vis absorbance, with the least stable film completely photobleaching within 6 days but the most stable film retaining 90% of its chromophore behavior over the same period. XPS confirmed oxidation of the end-caps as well as parts of the BDT-3T core, with the pyrazolone end-cap being most susceptible to degradation and barbituric acid being the least susceptible. This work clearly indicates the need to consider both optoelectronic properties as well as chemical stability in the design of complex push−pull molecules for devices.

The advent of scanning probe techniques has given spectroscopists powerful tools for acquiring highly specific chemical information with nanoscale spatial resolution. Rao and co-workers utilized two of these techniques, AFM-IR and IR s-SNOM, to explore whether either technique is suitable for studying device-relevant π-conjugated organic molecules.[175] Work on single crystals of 6,13-bis(triisopropylsilylethynyl)-pentacene (TIPS-PEN) and thin polycrystalline films of perfluorobutyldicyanoperylene carboxydiimide (PDIF-CN_2) allowed these researchers to demonstrate several pros and cons of AFM-IR and IR s-SNOM for such characterization. In general, the lower thermal expansion coefficient of organic crystals leads to low S/N in AFM-IR measurements for single crystal samples; therefore, AFM-IR is better suited for polycrystalline materials. IR s-SNOM yields high-resolution spectra for vibrational modes with transition dipole moments parallel to the electric field enhancement at the probe tip and along the conjugated backbone. However, since only selective modes can be observed, IR s-SNOM may be suitable only on a case-by-case basis depending on the molecular system. Well-resolved AFM-IR and IR s-SNOM spectra from PDIF-CN_2 led to further testing of the imaging capabilities of each technique. Although images could be obtained at specific wavenumbers with good contrast, these researchers noted the challenges of identifying the origin of signal contrast and subsequent image interpretation, which make these techniques difficult to use for definitive materials study. Further work on model systems should aid in establishing more concrete guidelines for use of these techniques to study organic semiconductors.

Regioregular poly(3-hexyl)thiophene (rr-P3HT) doped with 2,3,5,6-tetrafluoro-7,7,8,8,-tetracyanoquinodimethane (F_4TCNQ) is a common model organic semiconductor system. In this system, two types of electron transfer events can occur simultaneously: the desired integer charge transfer (ICT) resulting in free charge carriers or the undesired partial charge transfer (CPX), which results in localized trapping of charge carriers. In pristine F_4TCNQ-doped rr-P3HT films, ICT is the dominant electron transfer pathway. Watts et al. studied the stability of these charge states after observing a surprising conductivity decrease for samples stored under dark inert conditions.[176] To test the hypothesized conversion of ICT to CPX, FTIR spectroscopy was used to monitor the ν(C≡N) b_{1u} mode of F_4TCNQ which serves as a reporter for charge transfer type due to its sensitivity to local electron density. Using the known shift in this band to higher frequencies for the CPX relative to the ICT state, these researchers studied films with varying F_4TCNQ dopant concentration over the course of several weeks on films stored under dark inert conditions. Films of all dopant concentrations showed an increase of the CPX state with time with an inverse relationship between dopant concentration and CPX growth rate. A greater increase in CPX state was also observed for rr-P3HT films stored under ambient conditions compared to those stored in an inert environment. These results demonstrate functional performance degradation by processes intrinsic to the doped organic semiconductor system without exposure to significant degrading conditions and have high significance for understanding an important contribution to the limited lifetimes of such systems not previously recognized.

Organic semiconducting polymers are also often doped with transition metals to increase electrical conductivity. Abouelsayed and co-workers performed transmission measurements spanning from the THz to the UV frequency regions on a Ag@polyaniline (Ag@PANI) core@shell nanocomposite.[177] Their THz-TDS setup provided information on optical constants in the 0.6−3 THz region and were merged with results from the mid-IR and UV spectral regions. A Kramers−Kronig transformation was applied across on the whole frequency spectrum providing important optical parameters for the film including conductivity in the dc limit and Fermi energy. Using the localization-modified Drude model on the obtained optical conductivity spectrum, they noted that the Drude conductivity increased with incremental loading of $AgNO_3$. In fact, addition of $AgNO_3$ enhances the PANI degree of polymerization, increases the density of states at the Fermi level, and decreases the conduction bandwidth.

Although p-polarized multiple-angle incidence resolution spectrometry (pMAIRS) has been used extensively for molecular orientation determination on surfaces, it has not been useful for quantitative chemical analysis of compositional changes in thin films. Hasagawa and co-workers addressed this limitation by developing an approach that annihilates the optical anisotropy that allows orientation determination, thereby calculating an “orientation-free” spectrum that responds only to molecular amounts in thin films. The basis of their approach is calculating the simple average of the in-plane (IP) and out-of-plane (OP) spectral signals that are obtained simultaneously on a common intensity scale, thereby removing the optical anisotropy.[178] Using solution-processed pentacene (PEN) films by thermal conversion from its soluble spin-cast precursor 13,6-*N*-sulfinylacetamidopentacene (SAP), they monitored the IP and OP PEN vibrational bands with temperature until oriented PEN films were reached. From the calculated orientation-free spectrum, they demonstrated quantification of SAP amounts, thin film-phase PEN, and bulk-phase PEN in the films at the various temperatures until almost complete conversion of SAP to PEN at temperatures >420 K. These results demonstrate that pMAIRS is useful beyond molecular orientation analysis and can be used for compositional analysis as well.

Understanding the chemistry of metal−semiconductor organic interfaces is important for optimizing photonic and electronic devices such as OPVs, organic light emitting diodes, and organic field effect transistors. Sang et al. studied ultrathin (5 ML) films of α-sexithiophene (α-6T) with postdeposited low work function metals as a model system to understand the interfacial chemistry of thiophene-based polymers used in organic electronic devices.[179] With surface Raman spectroscopy in UHV, they found different interfacial reactions depending on the metal. No products resulting from electron transfer were observed at α-6T/Ag interfaces because of its higher work function; however, interfaces from the low work function Ca and Al depositions indicate interfacial chemistry initiated by electron transfer from the metal to α-6T. Surprisingly, the α-6T−Mg interface does not show evidence of reaction chemistry even though its work function is in between that of Ca and Al. This behavior was rationalized by rapid diffusion of Mg through the entire depth of the ultrathin α-6T films whereupon it deposited as a metallic film on the Ag substrate below. As a follow on to this work, Sang and coworkers investigated the penetration depth of Ca and Mg in terthiophene (3T) films of two thicknesses, 5 and 17 ML, with surface Raman spectroscopy in UHV.[180] Upon deposition of Ca, bands from chemical reaction products in the 5 ML film were of greater intensity relative to bands from unreacted 3T than in the 17 ML films for an identical Ca coverage. This observation suggests that a greater fraction of 3T is reduced in the thinner film. Additionally, as Ca coverage increases, the overall Raman intensities were increasingly attenuated for the 17 ML film but not for the 5 ML film indicating that Ca fully penetrates the 5 ML film but not the 17 ML film. Mg was found to be significantly less reactive than Ca and caused little spectral changes in thin 3T films. The absence of signal attenuation in these samples indicates the greater ability of Mg to penetrate the films. Collectively, these results provide important insight into low work function metal−organic interfaces that will remain relevant in the emerging field of organic electronics.

Monitoring ultrafast photochemical reaction pathways is difficult, since the processes cannot be described by the Born−Oppenheimer approximation. To study singlet fission in a complex pentacene dimer, Schnedermann and co-workers created a combined experimental and theoretical methodology based on ultrafast excited-state time-domain Raman spectroscopy with tree-tensor network state simulations.[181] With the time-domain Raman spectroscopy experiments, they observed transfer of vibrational wavepackets from the photoexcited singlet exciton to the pair of triplet excitons in a vibrationally coherent process. Benchmarking these results against their quantum simulations, they assigned the Raman spectrum to the dominant tuning modes and made educated inferences about coupling in the system to create a molecular movie for the singlet fission process. These researchers note the utility of their combined experimental-theoretical technique for investigation of other photochemical processes such as charge transfer reactions.

In related work on ultrafast processes, Schnedermann et al. tracked exciton and charge carrier transport in PEN thin films using a novel time-resolved TA and reflection microscope.[182] In brief, their approach couples an ultrafast pump−probe Raman experiment with a single-objective wide-field optical microscope. The pump pulses are focused tightly on the thin film surface for photoexcitation to generate a localized carrier population whose transient response is then spatially resolved by imaging time-delayed wide-field probe pulses. This approach provided effective temporal resolutions of 12 fs in transmission mode and ∼50 fs in reflection mode while simultaneously achieving sub-10 nm spatial resolution. This spatiotemporal capability allowed them to uncover a new ultrafast linear transport regime in PEN films corresponding to carrier transport lengths of up to 32 nm from the excitation spot. Simultaneous measurement of stimulated Raman scattering while monitoring spatiotemporal dynamics is a significant advance that should allow greater insight into charge transport in heterojunctions of materials in optoelectronic devices.

Spatially offset femtosecond stimulated Raman spectroscopy (SO-FSRS) has also been used to study exciton transport by Kwang et al.[183] They achieve this by holding the position of Raman pump and probe beams constant while raster scanning the photoexcitation beam. At each location, a complete FSRS set is collected and exciton diffusion can be monitored. To test their new technique, they monitored the exciton transport dynamics of TIPS-PEN by following structural evolution of the films due to photoexcitation in space and time. They confirmed that the fast exciton axis matches the free charge carrier transport axis and also observed a triplet fast exciton transport axis. A final observation that certain excitons generated along one part of the fast transport axis diffuse much faster than those generated elsewhere along the axis suggests a preference for unidirectional transport and perhaps preferential movement from thinner regions of the film to thicker regions. Future refinement of this technique could lead to pioneering work that would allow a deeper understanding of exciton and charge transport in energy-related materials.

Broadband 2DWL has been a useful technique for probing ultrafast processes like energy transfer. Kearns and co-workers introduced two geometries of a 2DWL spectrometer that generate for the first time supercontinuum radiation through an all-normal dispersion photonic crystal 70 MHz Yb fiber oscillator without relying on an amplified laser source.[184] Both geometries are almost identical with the only difference being that the simpler version uses only one set of birefringent wedge-pairs to generate the pump pulse pair instead of two. For collection of 2D spectra, two collinear pump pulses separated by a delay interact with the sample, with a probe pulse interacting with the sample after a delay period. After interaction, the pulse is dispersed in a spectrograph onto a linear detector array. Modulation is required to remove the background from the probe spectrum, and then a Fourier transform is completed at each probe pixel to generate the pump frequency axis. This system was demonstrated by collecting high quality 2DWL spectra from thin films of SWCNTs, with compression of their supercontinuum down to sub-20 femtoseconds levels. The ability to produce 2DWL without an amplified laser source is a significant advance, and the use of a 70 MHz oscillator may provide a viable pathway for microscope coupling in future work. In fact, this group has demonstrated 2DWL coupled with microscopy, albeit with a conventional laser-pumped setup. Recently, they reported development of a multimodal 2DWL microscopy system by combining broadband white light generation, AOM-based pulse-shaping, AFM, and confocal optical microscopy.[185] This innovative setup provides multidimensional high-resolution spectroscopic measurements and hyperspectral TA images. This system was demonstrated through simultaneous spectral

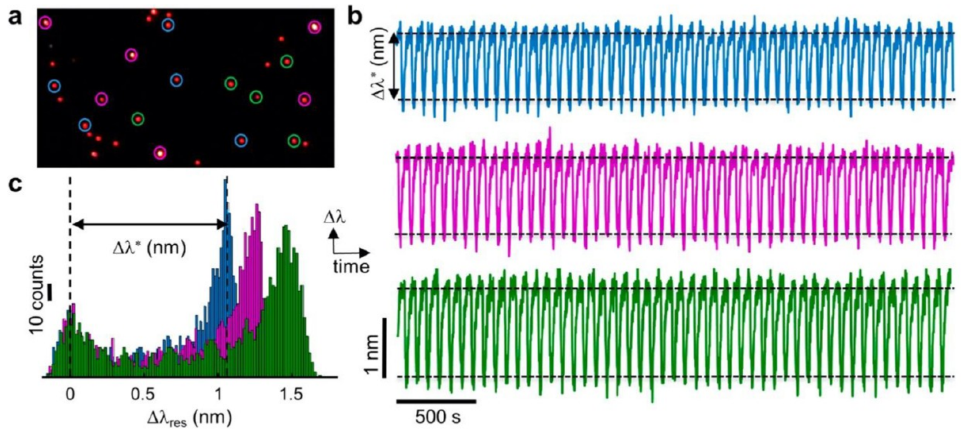

Figure 9. (a) Real-color image of the encoded substrate viewed under dark-field illumination. The red spots are the scattered light of individual nanoparticles. Our software groups particles according to eight batches, indicated here by differently colored circles around the spots. (b) The microscope setup allows tracking the dynamics of the plasmon resonance wavelength for each nanoparticle. Shown here are three representative time traces out of the more than 1000 obtained in a single experiment. (c) Histograms from the time traces to extract the wave amplitude $\Delta\lambda^*$ for each individual particle. Reprinted with permission from Ye, W.; Celiksoy, S.; Jakab, A.; Khmelinskaia, A.; Heermann, T.; Raso, A.; Wegner, S. V.; Rivas, G.; Schwille, P.; Ahijado-Guzman, R.; Sonnichsen, C. *J. Am. Chem. Soc.* **2018**, *140*, 17901−17906 (ref 188). Copyright 2018 American Chemical Society.

and spatial mapping of TIPS-PEN microcrystals. One highlight of their results was the observation of a slight red-shift in vibronic progression of a singlet state absorption peak as they probed across the TIPS-PEN microcrystal. This imaging system is a promising advance for better visualization of correlated morphology and electronic structure of materials.

■ BIOLOGICAL SURFACE AND INTERFACIAL PHENOMENA

The use of optical methods to study surfaces and interfaces of relevance in biological systems has remained an active area of research since the last review. SHG and two-photon fluorescence (TPF) were used by Hou and co-workers to study doxorubicin (DOX) adsorption at and incorporation into lipid membranes important for drug delivery.[186] With SHG, they observed that interactions between high concentrations of DOX and the lipid bilayer consist of a fast process (1−3 s), associated with adsorption-association-reorientation processes on the surface of the membrane and a slow process (5−50 s) involving dissociation-embedding-reorientation processes in the lipid membrane depending on DOX concentration in solution. TPF quenching studies allowed quantification of the DOX adsorption density at the lipid membrane, which was as high as 96% coverage in some cases. Although SHG is a commonly employed interfacial spectroscopy for study of membrane phenomena, TPF has mainly been used as a probe of bulk solution processes due to its lack of selectivity for the interface. However, as the TPF of DOX was shown to vary significantly in different chemical environments, this work clearly demonstrates the potential of TPF for quantitative probing of interfacial dynamics and adsorption density. Overall, these results provide insight into and guidelines for the study of drug−membrane interactions using a combination of these two powerful optical spectroscopic approaches.

Transporting molecules in and out of the plasma membrane is a critical regulatory function of cells, but observing cell binding and transport across a membrane is difficult without labeling. Wilhelm and co-workers used time-resolved SHG imaging to monitor the adsorption and transport of malachite green across a plasma membrane in a living human dermal fibroblast (HDF) cell.[187] In this approach, these researchers took advantage of the fact that, when molecules are adsorbed at the cell surface, the SHG signal increases, but as they diffuse across the bilayer, the signal becomes attenuated. Using this behavior, they calculated adsorption and transport rates of malachite green. Adsorption rates are generally constant across the cell; however, passive diffusion was observed to vary at different locations across the membrane. By mapping the transport rate constants through fitting analysis, it was found that transport rates were slower in portions of the membrane that appeared to have a higher degree of stress or strain. This was hypothesized to be the result of dynamic changes in membrane composition in response to stress that reduces permeability, although more study is needed. Overall, this work clearly demonstrates the potential of SHG imaging for membrane diffusion studies.

The advent of single-particle plasmon spectroscopy (NanoSPR) has allowed the detection and quantification of unlabeled macromolecules. Sönnichsen and colleagues systematically changed plasmonic penetration depth by adjusting the size of the plasmonic nanoparticle to resolve with subnanometer resolution the height of a dynamic bacterial protein assembly, MinDE, above supported lipid membranes of different composition.[188] These researchers utilized small shifts in the peak plasmon resonance of a single nanoparticle ($\Delta\lambda^*$) as the reporter of changes in local refractive index around that particle due to oscillatory dynamical changes in the protein assembly (see Figure 9). By monitoring these changes for thousands of nanoparticles of different sizes simultaneously, this work showed the strong influence of cardiolipin together with local membrane curvature on the Min protein dynamics. Although the effects of membrane composition and local membrane curvature on the MinDE assembly require further study, this work demonstrated the utility of this new method of NanoSPR as a promising probe of protein−membrane systems.

DMSO is a commonly used cryopreservation agent. However, it is known to be somewhat toxic to cells, although a detailed understanding of the mechanism of this toxicity is

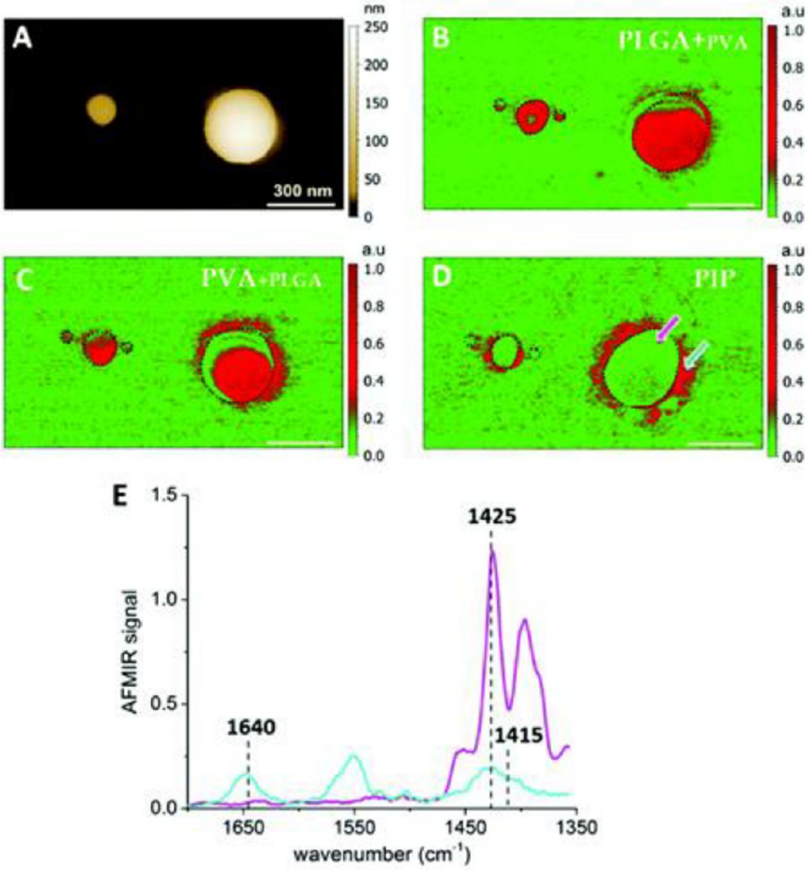

Figure 10. AFM-IR study of PIP-loaded PLGA NPs prepared by nanoemulsion. (A) Topography of PIP-loaded nanoemulsion PLGA NPs. (B) Tapping mode map at 1425 cm^{-1} corresponding to the strong absorption of PLGA. (C) Tapping AFM-IR map at 1415 cm^{-1} corresponding to weak absorption of PLGA and strong absorption of PVA. The NPs component present as the major component in the two IR maps is indicated in the figure with a bigger font size. (D) IR map at 1640 cm^{-1} showing the spatial distribution of the PIP colocalized with PVA in the corona around the PLGA NPs core. In the three IR maps, the black dotted line delimits the NPs topographical borders. (E) Average IR spectra of PIP corona (cyan arrow−cyan spectrum) and PLGA particles (pink arrow−pink spectrum). Republished with permission of The Royal Society of Chemistry from Mathurin, J.; Pancani, E.; Deniset-Besseau, A.; Kjoller, K.; Prater, C.; Gref, R.; Dazzi, A. *Analyst*, **2018**, *143*, 5940−5949 (ref 192). Permission conveyed through Copyright Clearance Center, Inc.

not yet in hand. DMSO is known to alter bulk water structure but how DMSO affects the water−lipid interface is not known. Venkatraman et al. explored this question through the use of ultrafast 2DIR to investigate how DMSO affects lipid headgroup H-bonding with water at such interfaces on the picosecond time scale.[189] By monitoring the ester ν(C═O) band, their 2DIR results demonstrate that the presence of DMSO leads to dehydration of the lipid head groups. Surprisingly, these studies also show that at concentrations <10%, DMSO speeds up H-bond dynamics while at concentrations >10% DMSO slows down H-bond dynamics. They rationalize this by concluding that, at low DMSO concentrations, H-bond networks are weakened and have disordered bulklike characteristics, speeding up interfacial water dynamics, whereas at higher concentrations, headgroup dehydration along with concomitant increased lipid−lipid interactions lead to overall slowing of dynamics. Additional MD simulations show good agreement with experimental results. Their results conclusively show that DMSO alters and even accelerates interfacial dynamics in certain cases, clearly demonstrating significant differences between interfacial and bulk dynamics.

Arguably one of the biggest drawbacks of IR techniques for the study of biological systems is the ubiquitous spectral interference from water. Xia and colleagues argue that, instead of being viewed as the enemy, water should be considered a universal IR probe for monitoring in situ, label-free interfacial biological events at surface-enhanced substrates.[190] These researchers used the loss of the interfacial water signal in ATR-SEIRA spectroscopy experiments as a quantitative indicator of interfacial biological processes that occur. As a first demonstration, they measured the displacement of interfacial water at a Au surface by a monolayer of PS spheres. The ν(O−H) band absorbance decrease was then used to determine the binding rate constants for an immune-recognition reaction in an antigen assembled on a Au nanoparticle film and interfacial DNA hybridization rate constants with a limit of detection for DNA of 0.2 nM. Although not an intuitive choice as an internal standard, the results from this study demonstrate the universality of water as a suitable probe of interfacial processes in biological systems.

The application of metasurface-based SEIRA has been utilized to study biomolecules; however, the analysis of live cell cultures has not been attempted previously. Shvets and colleagues cleverly demonstrate the utility of metasurface-enhanced infrared reflection spectroscopy (MEIRS) as a new technique for monitoring live cells.[191] The use of a metasurface in a reflectance configuration allows avoidance of water absorption, an issue that plagues biological samples in traditional transmission-mode experiments. In this approach, MEIR spectra were acquired using an FTIR-coupled IR microscope with a CaF_2 substrate covering a Fano-resonant plasmonic, nanostructured metasurface. This structure was immersed in cell culture attached to a flow cell through which cell medium circulated to keep the cells viable. The cells under study were A431 human squamous carcinoma cells, and the spectral regions of interest were 1500−1700 cm^{-1} for protein amide bands and 2800−3000 cm^{-1} for lipid $\nu(CH_2)/\nu(CH_3)$ bands. To validate the use of MEIRS for real-time live cell monitoring, trypsin was slowly introduced to the flow cell to cause cell dissociation. The reflectance spectra were acquired continuously over 200 min, and the time-dependent differential absorbance spectra were subjected to principal component analysis (PCA). The early time spectra clearly differentiated the cell states before and after trypsin addition. These researchers additionally used MEIRS to monitor the cellular response to cholesterol depletion induced by addition of methyl-β-cyclodextrin (MβCD) and MβCD-cholesterol, which complexed and extracted cholesterol from the cells. By monitoring both the amide and lipid spectral regions, cells exposed to MβCD were observed to detach from the metasurface, while cells treated with MβCD-cholesterol did not. Finally, using a focal plane array detector, these researchers were able to image live cells with their MEIRS setup. Although the finer subcellular features could not be imaged due to the diffraction limit, the ability to image single cells with MEIRS coupled with chemometric analysis could be useful for identifying subgroup populations in a heterogeneous sample or for drug-screening purposes.

With the spatial resolution of AFM and the chemical information obtained from IR spectroscopy, AFM-IR is now widely viewed as a powerful analytical tool. However, it is used mainly in contact mode, making the analysis of unsecured or soft samples such as those of relevance to biological studies difficult. Polymeric biodegradable nanoparticles used as drug delivery systems are one example of such soft materials. Improvements in the drug release profiles for these systems relies on knowing whether drug molecules are embedded in the nanoparticle core or adsorbed on the nanoparticle surface. Mathurin and colleagues used tapping AFM-IR to analyze nanoparticle morphology, composition, and drug location in such systems.[192] Briefly, tapping AFM-IR utilizes the conventional AFM tapping mode setup with a laser that is pulsed at high repetition rates. To minimize the resulting large far-field background signal, either a heterodyne approach is used or the tapping frequency is set to the second order mode of the cantilever, using the fundamental mode to sense the IR absorption. To test the visualization capabilities of this new tapping AFM-IR approach, these researchers used a core−shell nanoparticle geometry with a poly(lactic acid) core and a poly(vinyl alcohol) (PVA) shell. With tapping AFM-IR, they were able to clearly visualize the inner core and the surrounding PVA corona. With a model drug delivery system based on poly(D,L-lactic-*co*-glycolic acid) (PLGA)/PVA core−shell nanoparticles loaded with the drug pipemidic acid (PIP), they observed no PIP signal in the nanoparticle core, with all PIP colocalized in the corona (Figure 10). This corresponds well to previous experimental evidence for the "burst" fast release of PIP from these systems and demonstrates that PIP has low affinity for the PLGA matrix. With the ability to identify trace incorporation of PIP (1 wt %), this work demonstrates the power of tapping AFM-IR for design and study of drug delivery nanocarriers.

To improve the sensitivity of AFM-IR and single biomolecule detection, Ruggeri, Knowles, and co-workers modified a conventional AFM-IR setup by utilizing low laser power, short 100 ns pulses, and off-resonance monitoring to create off-resonance IR nanospectroscopy (ORS-nanoIR).[193] Using thyroglobulin and apoferritin, two proteins that are morphologically similar but with different secondary structures, they used their new instrumental arrangement for AFM-IR chemical mapping. By monitoring the amide I band, an indicator of protein secondary structure, these researchers mapped individual protein molecules in a mixed layer at the surface by deconvolution of the acquired IR spectra with high signal-to-noise ratio on the second time scale. Improvement in AFM-IR sensitivity to the single molecule level is an important advance for parsing the details of complex biological systems.

Antimicrobial resistance is a growing public health crisis. The need to identify the mechanism behind developed resistance is great and requires a toolkit of analytical methods. Kochan et al. used AFM-IR combined with chemometric analysis to study changes in chemical composition of two drug resistant strains of *Staphylococcus aureus*.[194] These researchers utilized paired clinical bacterial isolates, with the parent (susceptible) strain isolated prior to drug treatment and the daughter (resistant) strain obtained from the same patient after drug administration and resistance development. For the strain that developed resistance to the drug vancomycin, no morphological changes were noted but there was an increase in the band intensity at 1082 cm^{-1} indicating a higher relative content of carbohydrates and/or compounds with phosphodiester groups that lead to thickening of the cell wall carbohydrates. For the strain resistant to the drug daptomycin, no morphological changes were noted, but an in increase in absorbance was noted for several bands related to phospholipid content. These results confirm different modes of action by each drug in stimulating resistance, which is a significant observation. This work demonstrates the potential of AFM-IR for understanding antimicrobial resistance at the single bacterium level.

Contact-free acquisition of chemical information about virons at the single particle level has continued to elude researchers. Recent work by Cheng and co-workers demonstrates how the emerging technique of mid-infrared photothermal (MIP) imaging may offer an approach for label-free spectroscopic virus detection.[195] They used a counter-propagating interferometric MIP microscope to obtain vibrational fingerprint spectra from a single poxvirus and a single vesicular stomatitis virus (VSV) by monitoring their photothermal effect. Their instrument used a pulsed, mid-infrared pump beam from a QCL focused on the sample with the interferometric signal collected in an epi-illumination configuration. PMMA beads of 100 nm diameter were used as model systems to demonstrate the capabilities of the instrument. In subsequent studies of both viruses, the dominant spectral features are the amide I band at 1650 cm^{-1} and the amide II band at 1550 cm^{-1}. At both frequencies, good image contrast was obtained in the form of diffraction-limited spots, as the spatial resolution is insufficient to fully resolve the shape or morphology of the virus. To determine if this approach would allow virus differentiation, VSV samples were tested as well. Using differences in intensity ratio of the amide I and amide II bands between the two viruses, these researchers were able to differentiate the poxvirus from the VSV. The success of these experiments documents the utility of interferometric MIP for label-free detection of viruses or other nanoscale biological materials.

Nonlinear spectroscopies have proven to be powerful techniques for studying complex environments such as biological interfaces. However, since the response depends on the second order susceptibility, it has been difficult to detect molecules with small contributions to this susceptibility, since detection is limited by the precision with which the phase and amplitude can be measured. To address these challenges, Thämer and co-workers developed a new phase-sensitive, time-domain vSFG spectrometer.[196] Their setup utilizes a full colinear beam geometry and simultaneous referencing approach to obtain highly accurate phase and amplitude measurements leading to a signal-to-noise ratio improved by almost an order of magnitude. The reader is directed to the original paper for a thorough examination of the instrument theory. However, a few key highlights of their design include (i) the colinear beam geometry, which allows independence of the measured phase and amplitude from sample position, vibrations, or optics drift; (ii) independence of the SFG signal emission angle due to the wave vector conservation; (iii) concurrent sample and reference spectra collection through use of an oscillating mirror; and (iv) increased S/N from employing balanced detection with the local oscillator and sample SFG responses orthogonally polarized. This design provides low noise, complex SFG data. To demonstrate the capabilities of this system, the authors used the spectrometer setup to investigate the surface response of α-quartz. As a noncentrosymmetric crystal, α-quartz exhibits bulk SFG activity, but the phase-resolved isolation of the SFG contribution from the surface has not been observed, because its contribution to the susceptibility is small relative to the contribution from the bulk. Using linear numerical algebra methods, the spectral response was successfully decomposed into discrete contributions from the bulk and the surface that matched prediction. With further refinement, these researchers hope to extend this approach to study other species that currently cannot be easily measured via conventional vSFG such as protons and hydroxide ions at biological interfaces.

While infrared-visible vSFG is a robust technique, it can be enhanced by having both the IR and visible beams resonant with a surface vibrational mode and an excited electronic state, respectively. This yields the technique of doubly resonant vSFG (DR-vSFG). Velarde and co-workers utilized DR-vSFG to study the vibronic coupling of a novel substituted azobenzene push−pull (donor−acceptor) molecule that may be a useful probe for biological interfaces due to its absorbance in the visible and infrared regimes.[197] For biological applications in which cells and tissue absorb UV radiation and may be damaged, visible or near-infrared (NIR) light is essential for stimulating optical response. Therefore, considerable effort has been expended in the synthesis of azobenzene derivatives that absorb in the visible to near-IR region, especially at wavelengths corresponding to the biological transparency window. The results of these researchers showed for the first time prominent SFG signal enhancement of selective stretching modes that is attributed to the different electronic properties of photochromic cis−trans isomers coexisting at silica surfaces. This work demonstrates conformational-specific vibronic coupling that allows identification of the two distinct photoisomers at the surface. As substantiated by their theoretical modeling, these researchers demonstrated that vibronic coupling of the cis $\nu(\mathrm{C{=}C})$ mode with the cis-allowed (albeit weak) $S_0 \rightarrow S_1$ ($n \rightarrow \pi^*$) transition that is forbidden for the trans-isomer. Their computational analysis further predicts vibronic coupling for the trans $\nu(\mathrm{N{=}N})$ and $\nu(\mathrm{C{\equiv}N})$ modes at higher energy through the $S_0 \rightarrow S_2$ ($\pi \rightarrow \pi^*$) transition. The significance of this development is access to interfacial conformational information that is relevant to processes such as electron transfer and interfacial electric fields, both of which are important in the development of molecular probes for biological interfaces.

Biomaterials engineering of interfaces, including the creation of unnatural proteins, are areas of great interest. One challenge that researchers face is discerning how the chirality of amino acids affects the secondary structure of proteins. Perets et al. used chiral and achiral vSFG to probe the effects of chiral inversion of amino acids on the secondary structure of the antiparallel β-sheet LK$_7\beta$, with either all (L-), all (D-), or alternating (L-Leu/D-Lys) amino acid components, at air−glass and air−water interfaces.[198] These researchers found that all (L-) and all (D-) peptides have identical vSFG spectra, showing three bands in the $\nu(\mathrm{C{-}H})$ region, forming β-sheets. However, an alternating (L-)/(D-) peptide exhibits significant suppression of the $\nu_a(\mathrm{CH_2})$ spectral band and does not form an antiparallel β-sheet. Similarly, chiral vSFG spectra of all (L-) and all (D-) peptides were indistinguishable, while the alternating (L-)/(D-) peptide showed no chiral response. Thus, on the basis of both experimental work and computational modeling, these researchers concluded that a total chirality inversion does not affect LK$_7\beta$ interfacial properties but that mixed chirality does. Additionally, the silence of the $\nu_a(\mathrm{CH_2})$ band in the achiral vSFG spectrum of alternating LK$_7\beta$ suggests that around the interface, the system adopts a disordered, isotropic orientation. Finally, additional computational work indicated that regardless of chirality, the leucine side chains point toward the air while the lysine side chains point toward the water. This strong preference suggests that alternating hydrophobic and hydrophilic chains affects secondary structure. Extensions of these studies can help provide guidelines for establishing links between primary and secondary or tertiary structures and aid in the design of unnatural protein structures.

Chiroptical spectroscopy has garnered much interest lately due in part to the emergence of plasmonic chirality. Protein−protein interactions are governed by stereospecific charge distribution of the amino acid residues on the protein surfaces. However, common circular dichroism techniques are insensitive to these chiral surface charge distributions such that unique spectral fingerprints are not obtained. Rodier et al. demonstrate that the chiroptical properties of Au chiral plasmonic structures can be used to observe these chiral protein surface charge distributions through monitoring asymmetries in the protein-chiral nanostructure response using circular dichroism and optical rotatory dispersion.[199] In these studies, two structurally homologous proteins, two variants of type II dehydroquinase (DHQase), can be distinguished through differences in their reflectance-based optical rotatory dispersion (ORD) responses at these chiral plasmonic surfaces even though conventional CD cannot distinguish them. The chiroptical substrates used were comprised of 100 nm-thick Au plasmonic metafilms templated onto nanostructured polycarbonate substrates with either left-handed (LH) or right-handed (RH) 6-fold, rotationally symmetric Shuriken-shaped indentations; these were identified as “template plasmonic substrates” (TPSs). After immobilization of DHQase on the TPS, they observed that asymmetry parameters of different DHQases vary widely, suggesting that local chiral charge distributions cause these differences. This effect was rationalized as being due to creation of an enantiomeric image charge distribution in the metal which alters the optical activity of the plasmonic response. The ability to detect the changes in surface charge distribution of through enantiomeric plasmonic responses has important and broad implications for the study of structurally homologous biomolecules. These effects are likely to be frequently exploited in the future for such studies.

Kalachyova and co-workers reported a chiral-active hybrid plasmonic substrate consisting of M- or P-[6]helicine coupled with a SPP-supported Au grating for direct enantiomeric detection in a SERS experiment.[200] In a proof-of-concept experiment, they showed enantioselective discrimination of L- and D-cysteine and tartaric acid. Interestingly, the Au-M substrates preferentially enhanced the L-cysteine and L-tartic acid Raman bands while the Au−P substrate enhanced both D-enantiomers, indicating coincidence of substrate optical activity and selective chiral analyte response. Further evidence was provided through enantiospecific SERS measurements of L- and D-dihydroxyphenylalanine (DOPA) in which L-enantiomers were again enhanced on the Au-M substrate while D-enantiomers were enhanced on the Au−P substrate. DOPA detection was demonstrated down to 10^{-14} M for both enantiomers on their preferred substrates, but of perhaps greater significance, these substrates also allowed estimation of enantiomeric amounts even in the presence of the opposite enantiomer. These results represent a major advance in direct enantiomeric SERS detection that will be invaluable for further study of biological systems.

One final advance worth noting in terms of probe-based spectroscopies for biological applications is the work of Voylov and co-workers who developed noncontact mode tip enhanced Raman spectroscopy (TERS) for rough or sticky samples such as biological systems.[201] As a proof-of-concept, these workers first used a side-illumination configuration and oxidized tips for signal enhancement on carbon nanotubes on a Si wafer and graphene oxide on an oxidized Si wafer. In both cases they were successful in chemical imaging and obtained enhancement values on the orders of 10^3 and 10^5, respectively. To demonstrate utility in biological system studies, they used noncontact TERS to resolve the binding site for binding between androgen receptor (AR) activation function-1 domain (AF-1) protein and androgen receptor degrader (SARD). By monitoring the characteristic 1325 cm^{-1} band of SARD, they mapped the SARD location, finding spatial regions with higher or lower SARD concentrations. It was noted that these workers attempted these studies with standard contact-mode TERS, but these experiments failed due to severe tip contamination. Thus, the addition of noncontact mode TERS to the toolbox may facilitate studies of biological systems not amenable to more standard approaches.

SUMMARY AND FUTURE OUTLOOK

Advances in the application of optical spectroscopy in the UV, visible, IR, and THz regions of the electromagnetic spectrum for the study of phenomena at surfaces, interfaces, and thin films have continued unabated since the last review. Methods based on plasmonics continue to play a very prominent role in this area, with the breadth of plasmonic-based techniques and studies expanding rapidly. Improvements in spatial and temporal resolution have been particularly noteworthy as has the wide variety of surface, interfacial, and thin film applications areas in which investigations have been made.

The breadth of literature sources within which the scientific advances reported herein appeared convey the broad and diverse reach of this area. Significantly, techniques that once were only within the realm of specialists are becoming more routinely accessible to a broader range of researchers across multiple disciplines. Such expansion into communities of nonexperts is a hallmark of chemical measurement science tools that are rapidly maturing and truly impactful in answering relevant scientific questions. For this reason, one can reasonably expect that the creative energy that has fueled these advances will persist for the foreseeable future.

AUTHOR INFORMATION

Corresponding Author

Jeanne E. Pemberton − *Department of Chemistry and Biochemistry, University of Arizona, Tucson, Arizona 85721, United States;* orcid.org/0000-0002-1710-2922;
Email: pembertn@email.arizona.edu

Authors

Thomas J. Blackburn − *Department of Chemistry and Biochemistry, University of Arizona, Tucson, Arizona 85721, United States*
Sarah M. Tyler − *Department of Chemistry and Biochemistry, University of Arizona, Tucson, Arizona 85721, United States*

Complete contact information is available at:
https://pubs.acs.org/10.1021/acs.analchem.1c05323

Notes

The authors declare no competing financial interest.

Biographies

Thomas J. Blackburn obtained his B.A. degree in Chemistry from Wesleyan University in 2016. He is working toward his Ph.D. degree at the University of Arizona in the laboratory of Professor Jeanne E. Pemberton studying degradation chemistry of organic semiconductors.

Sarah M. Tyler obtained her B.S. degree in Chemistry from Purdue University in 2017. She is currently pursuing her Ph.D. degree under the direction of Professor Jeanne E. Pemberton at the University of Arizona investigating the photodegradation of organic semiconductors with a focus on 2D-correlation spectroscopy and chemometric analyses.

Jeanne E. Pemberton obtained a B.S. degree with Honors in Chemistry and a B.A. degree in Biology from the University of Delaware in 1977. She obtained her Ph.D. degree in Chemistry from the University of North Carolina at Chapel Hill in 1981 working under the direction of Richard P. Buck. She is a Regents Professor and the John and Helen Schaefer Professor of Chemistry at the University of Arizona, where she has been since starting there as an Assistant Professor in 1981. Her research interests are in surface and interfacial chemistry, with a particular emphasis on optical spectroscopies for surface, interface, and thin film analysis.

ACKNOWLEDGMENTS

This review was prepared with financial support from the National Science Foundation, Division of Materials Research under Grant Award DMR-2003631. We would be remiss if we

did not note with profound sadness the passing in 2019 of a true giant and pioneer in areas related to this review, ***Professor Richard P. Van Duyne***. This review is dedicated to his memory and to the living legacy of plasmonic science that his work inspired.

■ REFERENCES

(1) Watts, K. E.; Blackburn, T. J.; Pemberton, J. E. *Anal. Chem.* **2019**, *91*, 4235−4265.

(2) Kang, H.; Buchman, J. T.; Rodriguez, R. S.; Ring, H. L.; He, J.; Bantz, K. C.; Haynes, C. L. *Chem. Rev.* **2019**, *119*, 664−699.

(3) Ahuja, T.; Ghosh, A.; Mondal, S.; Basuri, P.; Jenifer, S. K.; Srikrishnarka, P.; Mohanty, J. S.; Bose, S.; Pradeep, T. *Analyst* **2019**, *144*, 7412−7420.

(4) Li, A.; Baird, Z.; Bag, S.; Sarkar, D.; Prabhath, A.; Pradeep, T.; Cooks, R. G. *Angew. Chem., Int. Ed.* **2014**, *53* (46), 12528−12531.

(5) Ghosh, A.; Ahuja, T.; Chaudhari, K.; Pradeep, T. *J. Phys. Chem. C* **2020**, *124*, 16644−16651.

(6) Cetin, A. E.; Yilmaz, C.; Galarreta, B. C.; Yilmaz, G.; Altug, H.; Busnaina, A. *Plasmonics* **2020**, *15*, 1165−1171.

(7) Ma, Y.; Sikdar, D.; Fedosyuk, A.; Velleman, L.; Klemme, D. J.; Oh, S.-H.; Kucernak, A. R. J.; Kornyshev, A. A.; Edel, J. B. *ACS Nano* **2020**, *14*, 328−336.

(8) Park, J. E.; Yonet-Tanyeri, N.; Vander Ende, E.; Henry, A.-I.; Perez White, B. E.; Mrksich, M.; Van Duyne, R. P. *Nano Lett.* **2019**, *19*, 6862−6868.

(9) Pan, C.; Li, X.; Sun, J.; Li, Z.; Zhang, L.; Qian, W.; Wang, P.; Dong, J. *ACS Appl. Bio Mater.* **2019**, *2*, 2102−2108.

(10) Huang, Y.-F.; Wang, W.; Guo, H.-Y.; Zhan, C.; Duan, S.; Zhan, D.; Wu, D.-Y.; Ren, B.; Tian, Z.-Q. *J. Am. Chem. Soc.* **2020**, *142*, 8483−8489.

(11) Ha, M.; Kim, J.-H.; You, M.; Li, Q.; Fan, C.; Nam, J.-M. *Chem. Rev.* **2019**, *119*, 12208−12278.

(12) Chang, F.-C.; Li, Y.-C.; Wu, R.-J.; Chen, C.-H. *ACS Appl. Nano Mater.* **2019**, *2*, 2515−2524.

(13) Dey, P.; Tabish, T. A.; Mosca, S.; Palombo, F.; Matousek, P.; Stone, N. *Small* **2020**, *16*, 1906780.

(14) Yang, J.-M.; Pan, Z.-Q.; Qin, F.-F.; Chen, M.; Wang, K.; Xia, X.-H. *Chem. Commun.* **2018**, *54*, 13236−13239.

(15) Grys, D.-B.; de Nijs, B.; Salmon, A. R.; Huang, J.; Wang, W.; Chen, W.-H.; Scherman, O. A.; Baumberg, J. J. *ACS Nano* **2020**, *14*, 8689−8696.

(16) Huang, J.; Grys, D.-B.; Griffiths, J.; de Nijs, B.; Kamp, M.; Lin, Q.; Baumberg, J. J. *Sci. Adv.* **2021**, *7*, eabg17790.

(17) Baumberg, J. J.; Aizpurua, J.; Mikkelsen, M. H.; Smith, D. R. *Nat. Mater.* **2019**, *18*, 668−678.

(18) Xomalis, A.; Chikkaraddy, R.; Oksenberg, E.; Shlesinger, I.; Huang, J.; Garnett, E. C.; Koenderink, A. F.; Baumberg, J. J. *ACS Nano* **2020**, *14*, 10562−10568.

(19) Zong, C.; Premasiri, R.; Lin, H.; Huang, Y.; Zhang, C.; Yang, C.; Ren, B.; Ziegler, L. D.; Cheng, J. X. *Nat. Commun.* **2019**, *10*, 5318.

(20) Hu, S.; Liu, B.-J.; Feng, J.-M.; Zong, C.; Lin, K.-Q.; Wang, X.; Wu, D.-Y.; Ren, B. *J. Am. Chem. Soc.* **2018**, *140*, 13680−13686.

(21) Li, Y.; Hu, H.; Jiang, W.; Shi, J.; Halas, N. J.; Nordlander, P.; Zhang, S.; Xu, H. *Nano Lett.* **2020**, *20*, 3499−3505.

(22) Sacco, A.; Mangino, S.; Portesi, C.; Vittone, E.; Rossi, A. M. *J. Phys. Chem. C* **2019**, *123*, 24723−24730.

(23) Bhattarai, A.; El-Khoury, P. Z. *Chem. Commun.* **2017**, *53*, 7310−7313.

(24) Kato, R.; Umakoshi, T.; Verma, P. *J. Phys. Chem. C* **2021**, *125*, 20397−20404.

(25) Lee, D. Y.; Park, C.; Choi, J.; Koo, Y.; Kang, M.; Jeong, M. S.; Raschke, M. B.; Park, K. *Nat. Commun.* **2021**, *12*, 3465.

(26) Alamri, M.; Sakidja, R.; Goul, R.; Ghopry, S.; Wu, J. Z. *ACS Appl. Nano Mater.* **2019**, *2*, 1412−1420.

(27) Zhu, Y.-P.; El-Demellawi, J. K.; Yin, J.; Lopatin, S.; Lei, Y.; Liu, Z.; Miao, X.; Mohammed, O. F.; Alshareef, H. N. *Adv. Mater.* **2020**, *32*, 1908392.

(28) Cao, Y.; Liang, P.; Dong, Q. M.; Wang, D.; Zhang, D.; Tang, L. S.; Wang, L.; Jin, S. Z.; Ni, D. K.; Yu, Z. *Anal. Chem.* **2019**, *91*, 8683−8690.

(29) Lin, J.; Ren, W. Z.; Li, A. R.; Yao, C. Y.; Chen, T. X.; Ma, X. H.; Wang, X. T.; Wu, A. G. *ACS Appl. Mater. Interfaces* **2020**, *12*, 4204−4211.

(30) Busson, B.; Dalstein, L. *J. Phys. Chem. C* **2019**, *123*, 26597−26607.

(31) Li, J. F.; Huang, Y. F.; Ding, Y.; Yang, Z. L.; Li, S. B.; Zhou, X. S.; Fan, F. R.; Zhang, W.; Zhou, Z. Y.; Wu, D. Y.; Ren, B.; Wang, Z. L.; Tian, Z. Q. *Nature* **2010**, *464*, 392−395.

(32) He, Y.; Ren, H.; You, E.-M.; Radjenovic, P. M.; Sun, S.-G.; Tian, Z.-Q.; Li, J.-F.; Wang, Z. *Phys. Rev. Lett.* **2020**, *125*, 047401.

(33) Osorio-Román, I. O.; Guerrero, A. R.; Albella, P.; Aroca, R. F. *Anal. Chem.* **2014**, *86*, 10246−10251.

(34) Mishra, H.; Mali, B. L.; Karolin, J.; Dragan, A. I.; Geddes, C. D. *Phys. Chem. Chem. Phys.* **2013**, *15*, 19538−19544.

(35) Meng, M.; Zhang, F.-L.; Yi, J.; Lin, L.-H.; Zhang, C.-L.; Bodappa, N.; Li, C.-Y.; Zhang, S.-J.; Aroca, R. F.; Tian, Z.-Q.; Li, J.-F. *Anal. Chem.* **2018**, *90*, 10837−10842.

(36) Li, C.-Y.; Duan, S.; Yi, J.; Wang, C.; Radjenovic, P. M.; Tian, Z.-Q.; Li, J.-F. *Sci. Adv.* **2020**, *6*, eaba6012.

(37) Park, K.-D.; May, M. A.; Leng, H.; Wang, J.; Kropp, J. A.; Gougousi, T.; Pelton, M.; Raschke, M. B. *Sci. Adv.* **2019**, *5*, eaav5931.

(38) Litvin, A. P.; Cherevkov, S. A.; Dubavik, A.; Babaev, A. A.; Parfenov, P. S.; Simões Gamboa, A. L.; Fedorov, A. V.; Baranov, A. V. *J. Phys. Chem. C* **2018**, *122*, 20469−20475.

(39) Tamma, V. A.; Beecher, L. M.; Shumaker-Parry, J. S.; Wickramasinghe, H. K. *Opt. Express* **2018**, *26*, 31439−31453.

(40) Zhou, J.; Smirnov, A.; Dietler, G.; Sekatskii, S. K. *Nano Lett.* **2019**, *19*, 8278−8286.

(41) Esmann, M.; Becker, S. F.; Witt, J.; Zhan, J.; Chimeh, A.; Korte, A.; Zhong, J.; Vogelgesang, R.; Wittstock, G.; Lienau, C. *Nat. Nanotechnol.* **2019**, *14*, 698−704.

(42) Yang, M.; Mattei, M. S.; Cherqui, C. R.; Chen, X.; Van Duyne, R. P.; Schatz, G. C. *Nano Lett.* **2019**, *19*, 7309−7316.

(43) Lee, H.; Kim, I.; Park, C.; Kang, M.; Choi, J.; Jeong, K.; Mun, J.; Kim, Y.; Park, J.; Raschke, M. B.; Park, H.; Jeong, M. S.; Rho, J.; Park, D. P. *Adv. Funct. Mater.* **2021**, *31*, 2102893.

(44) Bhaskar, S.; Das, P.; Srinivasan, V.; B. N., S. B.; Ramamurthy, S. S. *J. Phys. Chem. C* **2020**, *124*, 7341−7352.

(45) Adato, R.; Yanik, A. A.; Amsden, J. J.; Kaplan, D. L.; Omenetto, F. G.; Hong, M. K.; Erramilli, S.; Altug, H. *Proc. Natl. Acad. Sci. U. S. A.* **2009**, *106*, 19227−19232.

(46) Wu, C.; Khanikaev, A. B.; Adato, R.; Arju, N.; Yanik, A. A.; Altug, H.; Shvets, G. *Nat. Mater.* **2012**, *11*, 69−75.

(47) Aksu, S.; Cetin, A. E.; Adato, R.; Altug, H. *Adv. Opt. Mater.* **2013**, *1*, 798−803.

(48) Cetin, A. E.; Etezadi, D.; Altug, H. *Adv. Opt. Mater.* **2014**, *2*, 866−872.

(49) O'Callahan, B. T.; Hentschel, M.; Raschke, M. B.; El-Khoury, P. Z.; Lea, A. S. *J. Phys. Chem. C* **2019**, *123*, 17505−17509.

(50) Armelles, G.; Bergamini, L.; Cebollada, A.; Zabala, N.; Aizpurua, J. *J. Appl. Phys.* **2021**, *129*, 073103.

(51) Petti, M. K.; Ostrander, J. S.; Saraswat, V.; Birdsall, E. R.; Rich, K. L.; Lomont, J. P.; Arnold, M. S.; Zanni, M. T. *J. Chem. Phys.* **2019**, *150*, 024707.

(52) Leitis, A.; Tittl, A.; Liu, M.; Lee, B. H.; Gu, M. B.; Kivshar, Y. S.; Altug, H. *Sci. Adv.* **2019**, *5*, eaaw2871.

(53) Albinsson, D.; Nilsson, S.; Antosiewicz, T. J.; Zhdanov, V. P.; Langhammer, C. *J. Phys. Chem. C* **2019**, *123*, 6284−6293.

(54) Lindquist, N. C.; de Albuquerque, C. D. L.; Sobral-Filho, R. G.; Paci, I.; Brolo, A. G. *Nat. Nanotechnol.* **2019**, *14*, 981−987.

(55) de Albuquerque, C. D. L.; Hokanson, K. M.; Thorud, S. R.; Sobral-Filho, R. G.; Lindquist, N. C.; Brolo, A. G. *ACS Photonics* **2020**, *7*, 434−443.

(56) Khlebtsov, B. N.; Khanadeev, V. A.; Burov, A. M.; Le Ru, E. C.; Khlebtsov, N. G. *J. Phys. Chem. C* **2020**, *124*, 10647−10658.

(57) Gao, Z.; Yin, L.; Fang, W.; Kong, Q.; Fan, C.; Kang, B.; Xu, J.-J.; Chen, H.-Y. *ACS Photonics* **2019**, *6*, 2685−2693.

(58) Shin, D.; Lee, J. W. *Chem. Commun.* **2020**, *56*, 4047−4050.

(59) Ostovar, B.; Cai, Y.-Y.; Tauzin, L. J.; Lee, S. A.; Ahmadivand, A.; Zhang, R.; Nordlander, P.; Link, S. *ACS Nano* **2020**, *14*, 15757.

(60) Li, H.; Cheng, Y.; Tang, H.; Bi, Y.; Chen, Y.; Yang, G.; Guo, S.; Tian, S.; Liao, J.; Lv, X.; Zeng, S.; Zhu, M.; Xu, C.; Cheng, J.-X.; Wang, P. *Adv. Sci.* **2020**, *7*, 1903644.

(61) Phal, Y.; Yeh, K.; Bhargava, R. *Anal. Chem.* **2021**, *93*, 1294−1303.

(62) O'Callahan, B. T.; Crampton, K. T.; Novikova, I. V.; Jian, T.; Chen, C.-L.; Evans, J. E.; Raschke, M. B.; El-Khoury, P. Z.; Lea, A. S. *J. Phys. Chem. C* **2018**, *122*, 24891−24895.

(63) O'Callahan, B. T.; Park, K. D.; Novikova, I. V.; Jian, T.; Chen, C. L.; Muller, E. A.; El-Khoury, P. Z.; Raschke, M. B.; Lea, A. S. *Nano Lett.* **2020**, *20*, 4497−4504.

(64) Yeh, K.; Lee, D.; Bhargava, R. *Anal. Chem.* **2019**, *91*, 2177−2185.

(65) Akhtar, P.; Lindorfer, D.; Lingvay, M.; Pawlak, K.; Zsiros, O.; Siligardi, G.; Javorfi, T.; Dorogi, M.; Ughy, B.; Garab, G.; Renger, T.; Lambrev, P. H. *J. Phys. Chem. B* **2019**, *123*, 1090−1098.

(66) Gong, L.; Zheng, W.; Ma, Y.; Huang, Z. *Nat. Photonics* **2020**, *14*, 115−122.

(67) Ruggeri, F. S.; Marcott, C.; Dinarelli, S.; Longo, G.; Girasole, M.; Dietler, G.; Knowles, T. P. J. *Int. J. Mol. Sci.* **2018**, *19*, 2582.

(68) Liu, X.; Li, Y.; Xu, X.; Zhang, Y.; Li, B. *ACS Appl. Bio Mater.* **2019**, *2*, 2889−2895.

(69) Li, Y.; Xin, H.; Zhang, Y.; Lei, H.; Zhang, T.; Ye, H.; Saenz, J. J.; Qiu, C. W.; Li, B. *ACS Nano* **2018**, *12*, 10703−10711.

(70) Wang, R.; Kurouski, D. *J. Phys. Chem. C* **2018**, *122*, 24334−24340.

(71) Mueller, N. S.; Juergensen, S.; Höflich, K.; Reich, S.; Kusch, P. *J. Phys. Chem. C* **2018**, *122*, 28273−28279.

(72) Bhattarai, A.; Joly, A. G.; Krayev, A.; El-Khoury, P. Z. *J. Phys. Chem. C* **2019**, *123*, 7376−7380.

(73) Bhattarai, A.; El-Khoury, P. Z. *J. Phys. Chem. Lett.* **2019**, *10*, 2817−2822.

(74) Lee, J.; Crampton, K. T.; Tallarida, N.; Apkarian, V. A. *Nature* **2019**, *568*, 78−82.

(75) Braun, K.; Hauler, O.; Zhang, D.; Wang, X.; Chasse, T.; Meixner, A. J. *J. Am. Chem. Soc.* **2021**, *143*, 1816−1821.

(76) Su, H.-S.; Feng, H.-S.; Zhao, Q.-Q.; Zhang, X.-G.; Sun, J.-J.; He, Y.; Huang, S.-C.; Huang, T.-X.; Zhong, J.-H.; Wu, D.-Y.; Ren, B. *J. Am. Chem. Soc.* **2020**, *142*, 1341−1347.

(77) He, Z.; Han, Z.; Kizer, M.; Linhardt, R. J.; Wang, X.; Sinyukov, A. M.; Wang, J.; Deckert, V.; Sokolov, A. V.; Hu, J.; Scully, M. O. *J. Am. Chem. Soc.* **2019**, *141*, 753−757.

(78) Kim, S.; Yu, N.; Ma, X.; Zhu, Y.; Liu, Q.; Liu, M.; Yan, R. *Nat. Photonics* **2019**, *13*, 636−643.

(79) Schnell, M.; Goikoetxea, M.; Amenabar, I.; Carney, P. S.; Hillenbrand, R. *ACS Photonics* **2020**, *7*, 2878−2885.

(80) Wang, L.; Wang, H.; Vezenov, D.; Xu, X. G. *J. Phys. Chem. C* **2018**, *122*, 23808−23813.

(81) Kenkel, S.; Mittal, S.; Bhargava, R. *Nat. Commun.* **2020**, *11*, 3225.

(82) Rubano, A.; Mou, S.; Marrucci, L.; Paparo, D. *ACS Photonics* **2019**, *6*, 1515−1523.

(83) Aghamiri, N. A.; Huth, F.; Huber, A. J.; Fali, A.; Hillenbrand, R.; Abate, Y. *Opt. Express* **2019**, *27*, 24231−24242.

(84) Hunsche, S.; Koch, M.; Brener, I.; Nuss, M. C. *Opt. Commun.* **1998**, *150*, 22−26.

(85) Pizzuto, A.; Mittleman, D. M.; Klarskov, P. *Opt. Express* **2020**, *28*, 18778−18789.

(86) Ilchenko, O.; Pilgun, Y.; Kutsyk, A.; Bachmann, F.; Slipets, R.; Todeschini, M.; Okeyo, P. O.; Poulsen, H. F.; Boisen, A. *Nat. Commun.* **2019**, *10*, 5555.

(87) Stanciu, S. G.; Tranca, D. E.; Pastorino, L.; Boi, S.; Song, Y. M.; Yoo, Y. J.; Ishii, S.; Hristu, R.; Yang, F.; Bussetti, G.; Stanciu, G. A. *ACS Appl. Nano Mater.* **2020**, *3*, 1250−1262.

(88) Wang, H.; Wang, L.; Jakob, D. S.; Xu, X. G. *Nat. Commun.* **2018**, *9*, 2005.

(89) Li, H.; Zhao, Y.; Li, Y.; Liu, W. T. *Opt. Lett.* **2021**, *46*, 54−57.

(90) Jauffred, L.; Samadi, A.; Klingberg, H.; Bendix, P. M.; Oddershede, L. B. *Chem. Rev.* **2019**, *119*, 8087−8130.

(91) Huh, H.; Trinh, H. D.; Lee, D.; Yoon, S. *ACS Appl. Mater. Interfaces* **2019**, *11*, 24715−24724.

(92) Wu, Y.; Yang, M.; Ueltschi, T. W.; Mosquera, M. A.; Chen, Z.; Schatz, G. C.; Van Duyne, R. P. *J. Phys. Chem. C* **2019**, *123*, 29908−29915.

(93) Zhan, C.; Wang, Z.-Y.; Zhang, X.-G.; Chen, X.-J.; Huang, Y.-F.; Hu, S.; Li, J.-F.; Wu, D.-Y.; Moskovits, M.; Tian, Z.-Q. *J. Am. Chem. Soc.* **2019**, *141*, 8053−8057.

(94) Sheng, S.; Ji, Y.; Yan, X.; Wei, H.; Luo, Y.; Xu, H. *J. Phys. Chem. C* **2020**, *124*, 11586−11594.

(95) Sun, J.-J.; Su, H.-S.; Yue, H.-L.; Huang, S.-C.; Huang, T.-X.; Hu, S.; Sartin, M. M.; Cheng, J.; Ren, B. *J. Phys. Chem. Lett.* **2019**, *10*, 2306−2312.

(96) Tesema, T. E.; Kafle, B.; Habteyes, T. G. *J. Phys. Chem. C* **2019**, *123*, 8469−8483.

(97) Wang, R.; Li, J.; Rigor, J.; Large, N.; El-Khoury, P. Z.; Rogachev, A. Y.; Kurouski, D. *J. Phys. Chem. C* **2020**, *124*, 2238−2244.

(98) Dubi, Y.; Un, I. W.; Sivan, Y. *Chem. Sci.* **2020**, *11*, 5017−5027.

(99) Zhou, L.; Swearer, D. F.; Zhang, C.; Robatjazi, H.; Zhao, H.; Henderson, L.; Dong, L.; Christopher, P.; Carter, E. A.; Nordlander, P.; Halas, N. J. *Science* **2018**, *362*, 69−72.

(100) Keller, E. L.; Frontiera, R. R. *ACS Nano* **2018**, *12*, 5848−5855.

(101) Sarhan, R. M.; Koopman, W.; Pudell, J.; Stete, F.; Rössle, M.; Herzog, M.; Schmitt, C. N. Z.; Liebig, F.; Koetz, J.; Bargheer, M. *J. Phys. Chem. C* **2019**, *123*, 9352−9357.

(102) Szczerbiński, J.; Gyr, L.; Kaeslin, J.; Zenobi, R. *Nano Lett.* **2018**, *18*, 6740−6749.

(103) Ryu, H.-J.; Shin, H.; Oh, S.; Joo, J. H.; Choi, Y.; Lee, J.-S. *ACS Appl. Mater. Interfaces* **2020**, *12*, 2842−2853.

(104) Wei, D.; Yue, M.; Qin, S.; Zhang, S.; Wu, Y.; Xu, G.; Zhang, H.; Tian, Z.; Li, J. *J. Am. Chem. Soc.* **2021**, *143*, 15635−15643.

(105) Wang, C.; Chen, X.; Chen, T.-M.; Wei, J.; Qin, S. N.; Zheng, J.-F.; Zhang, H.; Tian, Z.-Q.; Li, J.-F. *ChemCatChem.* **2020**, *12*, 75−79.

(106) Wang, Y.-H.; Wei, J.; Radjenovic, P.; Tian, Z.-Q.; Li, J.-F. *Anal. Chem.* **2019**, *91*, 1675−1685.

(107) Nuguid, R. J. G.; Ferri, D.; Marberger, A.; Nachtegaal, M.; Kröcher, O. *ACS Catal.* **2019**, *9*, 6814−6820.

(108) Moncada, J.; Adams, W. R.; Thakur, R.; Julin, M.; Carrero, C. A. *ACS Catal.* **2018**, *8*, 8976−8986.

(109) Minova, I. B.; Matam, S. K.; Greenaway, A.; Catlow, C. R. A.; Frogley, M. D.; Cinque, G.; Wright, P. A.; Howe, R. F. *ACS Catal.* **2019**, *9*, 6564−6570.

(110) Schuschke, C.; Hohner, C.; Stumm, C.; Kettner, M.; Fromm, L.; Görling, A.; Libuda, J. *J. Phys. Chem. C* **2019**, *123*, 31057−31072.

(111) Liu, J.; He, N.; Zhou, W.; Shu, M.; Lin, L.; Wang, J.; Si, R.; Xiong, G.; Xin, Q.; Guo, H. *Catal. Sci. Technol.* **2019**, *9*, 1609−1620.

(112) Bhattacherjee, A.; Sneha, M.; Lewis-Borrell, L.; Tau, O.; Clark, I. P.; Orr-Ewing, A. J. *Nat. Commun.* **2019**, *10*, 5152.

(113) Greetham, G. M.; Donaldson, P. M.; Nation, C.; Sazanovich, I. V.; Clark, I. P.; Shaw, D. J.; Parker, A. W.; Towrie, M. *Appl. Spectrosc.* **2016**, *70*, 645−653.

(114) Ternero-Hidalgo, J. J.; Guerrero-Pérez, M. O.; Rodríguez-Mirasol, J.; Cordero, T.; Bañares, M. A.; Portela, R.; Bazin, P.; Clet, G.; Daturi, M. *Anal. Chem.* **2020**, *92*, 5100−5106.

(115) Liu, Y.; Wu, Z.; Naschitzki, M.; Gewinner, S.; Schöllkopf, W.; Li, X.; Paier, J.; Sauer, J.; Kuhlenbeck, H.; Freund, H.-J. *J. Am. Chem. Soc.* **2020**, *142*, 2665−2671.

(116) Chen, X.-J.; Yu, S.; Chen, J.-L.; Pérez-Jiménez, A. I.; Wu, D.-Y.; Tian, Z.-Q. *J. Phys. Chem. C* **2019**, *123*, 21478−21486.

(117) Klein, J. M.; Squire, H.; Gurkan, B. *J. Phys. Chem. C* **2020**, *124*, 5613−5623.

(118) Kang, G.; Yang, M.; Mattei, M. S.; Schatz, G. C.; Van Duyne, R. P. *Nano Lett.* **2019**, *19*, 2106−2113.

(119) Chen, X.; Brasiliense, V.; Van Duyne, R. P. *J. Phys. Chem. C* **2018**, *122*, 24329−24333.

(120) Huang, S.-C.; Ye, J.-Z.; Shen, X.-R.; Zhao, Q.-Q.; Zeng, Z.-C.; Li, M.-H.; Wu, D.-Y.; Wang, X.; Ren, B. *Anal. Chem.* **2019**, *91*, 11092−11097.

(121) Bao, Y.-F.; Cao, M.-F.; Wu, S.-S.; Huang, T.-X.; Zeng, Z.-C.; Li, M.-H.; Wang, X.; Ren, B. *Anal. Chem.* **2020**, *92*, 12548−12555.

(122) Zhang, Y.-J.; Su, Z.-F.; Li, J.-F.; Lipkowski, J. *J. Phys. Chem. C* **2020**, *124*, 13240−13248.

(123) Lu, Y.-H.; Larson, J. M.; Baskin, A.; Zhao, X.; Ashby, P. D.; Prendergast, D.; Bechtel, H. A.; Kostecki, R.; Salmeron, M. *Nano Lett.* **2019**, *19*, 5388−5393.

(124) Liu, Z.; Li, Y.; Xu, Q.; Wang, H.; Liu, W.-T. *J. Phys. Chem. Lett.* **2020**, *11*, 243−248.

(125) Liu, W.-T.; Shen, Y. R. *Proc. Natl. Acad. Sci. U. S. A.* **2014**, *111*, 1293−1297.

(126) Oquendo, L. E.; Ehamparam, R.; Armstrong, N. R.; Saavedra, S. S.; McGrath, D. V. *J. Phys. Chem. C* **2019**, *123*, 6970−6980.

(127) Zheng, Y.; Giordano, A. J.; Marder, S. R.; Saavedra, S. S. *Langmuir* **2020**, *36*, 6728−6735.

(128) Zhou, L.; Arugula, M. A.; Chin, B. A.; Simonian, A. L. *ACS Appl. Mater. Interfaces* **2018**, *10*, 41763−41772.

(129) Wang, Y.; Guo, W.; Yang, Q.; Su, B. *J. Am. Chem. Soc.* **2020**, *142*, 1222−1226.

(130) Lin, L.; Husek, J.; Biswas, S.; Baumler, S. M.; Adel, T.; Ng, K. C.; Baker, L. R.; Allen, H. C. *J. Am. Chem. Soc.* **2019**, *141*, 13525−13535.

(131) Piontek, S. M.; DelloStritto, M.; Mandal, B.; Marshall, T.; Klein, M. L.; Borguet, E. *J. Am. Chem. Soc.* **2020**, *142*, 12096−12105.

(132) Xiong, H.; Shi, L.; Wei, L.; Shen, Y.; Long, R.; Zhao, Z.; Min, W. *Nat. Photonics* **2019**, *13*, 412−417.

(133) Xiong, H.; Lee, J. K.; Zare, R. N.; Min, W. *J. Phys. Chem. Lett.* **2020**, *11*, 7423−7428.

(134) Ohno, P. E.; Chang, H.; Spencer, A. P.; Liu, Y.; Boamah, M. D.; Wang, H.-f.; Geiger, F. M. *J. Phys. Chem. Lett.* **2019**, *10*, 2328−2334.

(135) Li, C.-Y.; Yu, Y.; Wang, C.; Zhang, Y.; Zheng, S.-Y.; Li, J.-F.; Maglia, F.; Jung, R.; Tian, Z.-Q.; Shao-Horn, Y. *J. Phys. Chem. C* **2020**, *124*, 4024−4031.

(136) Flores, E.; Novák, P.; Aschauer, U.; Berg, E. J. *Chem. Mater.* **2020**, *32*, 186−194.

(137) Lee, T. S.; Patil, S. B.; Kao, Y. T.; An, J. Y.; Lee, Y. C.; Lai, Y. H.; Chang, C. K.; Cheng, Y. S.; Chuang, Y. C.; Sheu, H. S.; Wu, C. H.; Yang, C. C.; Cheng, R. H.; Lee, C. Y.; Peng, P. Y.; Lai, L. H.; Lee, H. H.; Wang, D. Y. *ACS Appl. Mater. Interfaces* **2020**, *12*, 2572−2580.

(138) Singh, A. K.; Yasri, N.; Karan, K.; Roberts, E. P. L. *ACS Appl. Energy Mater.* **2019**, *2*, 2324−2336.

(139) Lin, X.-M.; Wu, D.-Y.; Gao, P.; Chen, Z.; Ruben, M.; Fichtner, M. *Chem. Mater.* **2019**, *31*, 3239−3247.

(140) Yang, G.; Ivanov, I. N.; Ruther, R. E.; Sacci, R. L.; Subjakova, V.; Hallinan, D. T.; Nanda, J. *ACS Nano* **2018**, *12*, 10159−10170.

(141) Kim, J. H.; Chern, Z.-Y.; Yoo, S.; deGlee, B.; Wang, J.; Liu, M. *ACS Appl. Mater. Interfaces* **2020**, *12*, 2370−2379.

(142) Katayama, Y.; Nattino, F.; Giordano, L.; Hwang, J.; Rao, R. R.; Andreussi, O.; Marzari, N.; Shao-Horn, Y. *J. Phys. Chem. C* **2019**, *123*, 5951−5963.

(143) Chen, X.; Henckel, D. A.; Nwabara, U. O.; Li, Y.; Frenkel, A. I.; Fister, T. T.; Kenis, P. J. A.; Gewirth, A. A. *ACS Catal.* **2020**, *10*, 672−682.

(144) Kemna, A.; García Rey, N.; Braunschweig, B. *ACS Catal.* **2019**, *9*, 6284−6292.

(145) Heidary, N.; Morency, M.; Chartrand, D.; Ly, K. H.; Iftimie, R.; Kornienko, N. *J. Am. Chem. Soc.* **2020**, *142*, 12382−12393.

(146) Kukunuri, S.; Noguchi, H. *J. Phys. Chem. C* **2020**, *124*, 7267−7273.

(147) Chen, Z.; Jiang, S.; Kang, G.; Nguyen, D.; Schatz, G. C.; Van Duyne, R. P. *J. Am. Chem. Soc.* **2019**, *141*, 15684−15692.

(148) Saeed, K. H.; Forster, M.; Li, J.-F.; Hardwick, L. J.; Cowan, A. J. *Chem. Commun.* **2020**, *56*, 1129−1132.

(149) Yang, S.; Su, Y.; Xu, Y.; Wu, Q.; Zhang, Y.; Raschke, M. B.; Ren, M.; Chen, Y.; Wang, J.; Guo, W.; Ron Shen, Y.; Tian, C. *J. Am. Chem. Soc.* **2018**, *140*, 13746−13752.

(150) Chen, D.; Kang, Z.; Hirahara, H.; Li, W. *Nanoscale Adv.* **2020**, *2*, 2106−2113.

(151) Marcott, C.; Kansiz, M.; Dillon, E.; Cook, D.; Mang, M. N.; Noda, I. *J. Mol. Struct.* **2020**, *1210*, 128045.

(152) Watanabe, R.; Sugahara, A.; Hagihara, H.; Mizukado, J.; Shinzawa, H. *Anal. Chem.* **2020**, *92*, 12160−12167.

(153) Mester, L.; Govyadinov, A. A.; Chen, S.; Goikoetxea, M.; Hillenbrand, R. *Nat. Commun.* **2020**, *11*, 3359.

(154) Cavezza, F.; Pletincx, S.; Revilla, R. I.; Weaytens, J.; Boehm, M.; Terryn, H.; Hauffman, T. *J. Phys. Chem. C* **2019**, *123*, 26178−26184.

(155) Fockaert, L.-L. I.; Ganzinga-Jurg, D.; Versluis, J.; Boelen, B.; Bakker, H. J.; Terryn, H.; Mol, J. M. C. *J. Phys. Chem. C* **2020**, *124*, 7127−7138.

(156) Li, B.; Andre, J. S.; Chen, X.; Walther, B.; Paradkar, R.; Feng, C.; Tucker, C. J.; Mohler, C.; Chen, Z. *Langmuir* **2020**, *36*, 11349−11357.

(157) Cui, H.; Glidle, A.; Cooper, J. M. *Small* **2021**, *17*, 2101114.

(158) Petti, M. K.; Ostrander, J. S.; Birdsall, E. R.; Kunz, M. B.; Armstrong, Z. T.; Alperstein, A. M.; Zanni, M. T. *J. Phys. Chem. A* **2020**, *124*, 3471−3483.

(159) Dou, W.; Xu, C.; Guo, J.; Du, H.; Qiu, W.; Xue, T.; Kang, Y.; Zhang, Q. *ACS Appl. Mater. Interfaces* **2018**, *10*, 44941−44949.

(160) Wu, X.; Kim, M.; Qu, H.; Wang, Y. *Nat. Commun.* **2019**, *10*, 2672.

(161) Flach, J. T.; Wang, J.; Arnold, M. S.; Zanni, M. T. *J. Phys. Chem. Lett.* **2020**, *11*, 6016−6024.

(162) Kim, B.; Khan, R. M.; Fast, A.; Fishman, D. A.; Potma, E. O. *J. Phys. Chem. C* **2020**, *124*, 11694−11700.

(163) Schwartz, J. J.; Chuang, H. J.; Rosenberger, M. R.; Sivaram, S. V.; McCreary, K. M.; Jonker, B. T.; Centrone, A. *ACS Appl. Mater. Interfaces* **2019**, *11*, 25578−25585.

(164) Alexeev, E. M.; Mullin, N.; Ares, P.; Nevison-Andrews, H.; Skrypka, O.; Godde, T.; Kozikov, A.; Hague, L.; Wang, Y.; Novoselov, K. S.; Fumagalli, L.; Hobbs, J. K.; Tartakovskii, A. I. *ACS Nano* **2020**, *14*, 11110−11119.

(165) Gustafson, J. K.; Cunningham, P. D.; McCreary, K. M.; Jonker, B. T.; Hayden, L. M. *J. Phys. Chem. C* **2019**, *123*, 30676−30683.

(166) Sheng, S.; Wu, J.-B.; Cong, X.; Zhong, Q.; Li, W.; Hu, W.; Gou, J.; Cheng, P.; Tan, P.-H.; Chen, L.; Wu, K. *ACS Nano* **2019**, *13*, 4133−4139.

(167) Wu, S. F.; Richard, P.; Wang, X. B.; Lian, C. S.; Nie, S. M.; Wang, J. T.; Wang, N. L.; Ding, H. *Phys. Rev. B: Condens. Matter Mater. Phys.* **2014**, *90*, 054519.

(168) Zheng, L.-Q.; Servalli, M.; Schlüter, A. D.; Zenobi, R. *Chem. Sci.* **2019**, *10*, 9673−9678.

(169) Deng, G. H.; Qian, Y.; Wei, Q.; Zhang, T.; Rao, Y. *J. Phys. Chem. Lett.* **2020**, *11*, 1738−1745.

(170) Nishida, J.; Alfaifi, A. H.; Gray, T. P.; Shaheen, S. E.; Raschke, M. B. *ACS Energy Lett.* **2020**, *5*, 1636−1643.

(171) Yu, H. M.; Oh, H. M.; Park, D. Y.; Jeong, M. S. *J. Phys. Chem. C* **2020**, *124*, 3915−3922.

(172) Venugopal, A.; Kas, R.; Hau, K.; Smith, W. A. *J. Am. Chem. Soc.* **2021**, *143*, 18581−18591.

(173) Weu, A.; Kress, J. A.; Paulus, F.; Becker-Koch, D.; Lami, V.; Bakulin, A. A.; Vaynzof, Y. *ACS Appl. Energy Mater.* **2019**, *2*, 1943−1950.

(174) Watts, K. E.; Nguyen, T.; Tremolet de Villers, B. J.; Neelamraju, B.; Anderson, M. A.; Braunecker, W. A.; Ferguson, A. J.; Larsen, R. E.; Larson, B. W.; Owczarczyk, Z. R.; Pfeilsticker, J. R.; Pemberton, J. E.; Ratcliff, E. L. *J. Mater. Chem. A* **2019**, *7*, 19984−19995.

(175) Rao, V. J.; Matthiesen, M.; Goetz, K. P.; Huck, C.; Yim, C.; Siris, R.; Han, J.; Hahn, S.; Bunz, U. H. F.; Dreuw, A.; Duesberg, G. S.; Pucci, A.; Zaumseil, J. *J. Phys. Chem. C* **2020**, *124*, 5331−5344.
(176) Watts, K. E.; Neelamraju, B.; Ratcliff, E. L.; Pemberton, J. E. *Chem. Mater.* **2019**, *31*, 6986−6994.
(177) Abouelsayed, A.; Anis, B.; Eisa, W. H. *J. Phys. Chem. C* **2020**, *124*, 18243−18256.
(178) Shioya, N.; Fujiwara, R.; Tomita, K.; Shimoaka, T.; Hasegawa, T. *J. Phys. Chem. A* **2020**, *124*, 2714−2720.
(179) Sang, L.; Pemberton, J. E. *J. Phys. Chem. C* **2019**, *123*, 18877−18888.
(180) Sang, L.; Pemberton, J. E. *Chem. Mater.* **2019**, *31*, 6908−6917.
(181) Schnedermann, C.; Alvertis, A. M.; Wende, T.; Lukman, S.; Feng, J.; Schroder, F.; Turban, D. H. P.; Wu, J.; Hine, N. D. M.; Greenham, N. C.; Chin, A. W.; Rao, A.; Kukura, P.; Musser, A. J. *Nat. Commun.* **2019**, *10*, 4207.
(182) Schnedermann, C.; Sung, J.; Pandya, R.; Verma, S. D.; Chen, R. Y. S.; Gauriot, N.; Bretscher, H. M.; Kukura, P.; Rao, A. *J. Phys. Chem. Lett.* **2019**, *10*, 6727−6733.
(183) Kwang, S. Y.; Frontiera, R. R. *J. Phys. Chem. Lett.* **2020**, *11*, 4337−4344.
(184) Kearns, N. M.; Jones, A. C.; Kunz, M. B.; Allen, R. T.; Flach, J. T.; Zanni, M. T. *J. Phys. Chem. A* **2019**, *123*, 3046−3055.
(185) Jones, A. C.; Kearns, N. M.; Bohlmann Kunz, M.; Flach, J. T.; Zanni, M. T. *J. Phys. Chem. A* **2019**, *123*, 10824−10836.
(186) Hou, Y.; Chen, S. L.; Gan, W.; Ma, X.; Yuan, Q. *J. Phys. Chem. B* **2019**, *123*, 3756−3762.
(187) Sharifian Gh., M.; Wilhelm, M. J.; Moore, M.; Dai, H.-L. *Biochemistry* **2019**, *58*, 1841−1844.
(188) Ye, W.; Celiksoy, S.; Jakab, A.; Khmelinskaia, A.; Heermann, T.; Raso, A.; Wegner, S. V.; Rivas, G.; Schwille, P.; Ahijado-Guzman, R.; Sonnichsen, C. *J. Am. Chem. Soc.* **2018**, *140*, 17901−17906.
(189) Venkatraman, R. K.; Baiz, C. R. *Langmuir* **2020**, *36*, 6502−6511.
(190) Liu, Y.; Bao, W. J.; Zhang, Q. W.; Li, J.; Li, J.; Xu, J. J.; Xia, X. H.; Chen, H. Y. *Anal. Chem.* **2018**, *90*, 12979−12985.
(191) Huang, S. H.; Li, J.; Fan, Z.; Delgado, R.; Shvets, G. *Lab Chip* **2021**, *21*, 3991−4004.
(192) Mathurin, J.; Pancani, E.; Deniset-Besseau, A.; Kjoller, K.; Prater, C. B.; Gref, R.; Dazzi, A. *Analyst* **2018**, *143*, 5940−5949.
(193) Ruggeri, F. S.; Mannini, B.; Schmid, R.; Vendruscolo, M.; Knowles, T. P. J. *Nat. Commun.* **2020**, *11*, 2945.
(194) Kochan, K.; Nethercott, C.; Perez Guaita, D.; Jiang, J. H.; Peleg, A. Y.; Wood, B. R.; Heraud, P. *Anal. Chem.* **2019**, *91*, 15397−15403.
(195) Zhang, Y.; Yurdakul, C.; Devaux, A. J.; Wang, L.; Xu, X. G.; Connor, J. H.; Unlu, M. S.; Cheng, J. X. *Anal. Chem.* **2021**, *93*, 4100−4107.
(196) Thamer, M.; Campen, R. K.; Wolf, M. *Phys. Chem. Chem. Phys.* **2018**, *20*, 25875−25882.
(197) Raab, M.; Becca, J. C.; Heo, J.; Lim, C. K.; Baev, A.; Jensen, L.; Prasad, P. N.; Velarde, L. *J. Chem. Phys.* **2019**, *150*, 114704.
(198) Perets, E. A.; Videla, P. E.; Yan, E. C. Y.; Batista, V. S. *J. Phys. Chem. B* **2019**, *123*, 5769−5781.
(199) Rodier, M.; Keijzer, C.; Milner, J.; Karimullah, A. S.; Roszak, A. W.; Barron, L. D.; Gadegaard, N.; Lapthorn, A. J.; Kadodwala, M. *Nanoscale Horiz.* **2020**, *5*, 336−344.
(200) Kalachyova, Y.; Guselnikova, O.; Elashnikov, R.; Panov, I.; Zadny, J.; Cirkva, V.; Storch, J.; Sykora, J.; Zaruba, K.; Svorcik, V.; Lyutakov, O. *ACS Appl. Mater. Interfaces* **2019**, *11*, 1555−1562.
(201) Voylov, D. N.; Bocharova, V.; Lavrik, N. V.; Vlassiouk, I.; Polizos, G.; Volodin, A.; Shulga, Y. M.; Kisliuk, A.; Thiyagarajan, T.; Miller, D. D.; Narayanan, R.; Sumpter, B. G.; Sokolov, A. P. *Nanoscale Adv.* **2019**, *1*, 3392−3399.